Simulation Study on an Electron-Tracking Compton Camera for Deep Gamma-ray Burst Search

Tatsuya Sawano

Department of Physics, Graduate School of Science, Kyoto University
Kitashirakawa Oiwake-cho, Sakyo-ku, Kyoto, 606-8502, Japan
sawano@cr.scphys.kyoto-u.ac.jp

This thesis was submitted to the Department of Physics,
Graduate School of Science, Kyoto University
on January 5 2017
in partial fulfillment of the requirements
for the degree of Doctor of Philosophy in physics.

Abstract

Although the MeV gamma-ray sky in the universe is filled with astronomical explosive phenomena such as supernovae and gamma-ray bursts, no MeV gamma-ray all-sky survey mission is in progress. This is because that the estimate of the MeV gamma-ray detector sensitivity in space is difficult due to the huge background events and the incompleteness of imaging method of MeV gamma rays. To solve those problems, we have been developing an Electron-Tracking Compton Camera (ETCC) for balloon-/satellite- borne experiment, named as Sub-MeV gamma-ray Imaging Loaded-on- balloon/satellite Experiment (SMILE). The final goal of the SMILE project is to observe the MeV gamma-ray sky with 100 times better sensitivity than that of COMPTEL. The ETCC realizes MeV gamma-ray geometrical optics with the introduction of the point spread function (PSF) and background event rejection by particle identification. As the step to the future observation with a satellite platform, we plan to demonstrate the imaging capability of steady celestial objects with a balloon experiment (SMILE-II). For the precise prediction on the performance of the future ETCC, it is essential to develop a simulator that precisely reproduces the electron tracking. Therefore we developed the ETCC simulator with which both the physics process and the response of the electronics are considered. We also developed a balloon-borne ETCC (SMILE-II/ETCC), and tested the performance of the ETCC comparing to that obtained by the simulator. The effective area calculated by the simulator and that obtained by the experiment are consistent within $\sim 30\%$. We studied the background intensity at the SMILE-II balloon experiment with a Monte Carlo simulation. We found that the intensity of the intrinsic gamma rays accounts for about one third of the total background, while the background from neutron elastic scattering events is not predominant. The improvement of the PSF of 10 degrees will greatly work to magnify the statistical significance for the Crab detection to be 7.4σ. Furthermore, we investigated an impact to the high-energy time domain astronomy using the ETCC with a well-defined PSF. To explore ultra-long or high-redshift GRBs and SGRBs associated with gravitational sources, an extended ETCC with an effective area more than 100 cm^2 and a PSF of 2 degrees should be developed. Though the sensitivity of the ETCC to GRBs by the 1-sec burst trigger is comparable to that of BATSE, the ETCC will detect high-redshift GRBs by the image trigger with a duration of 10 - 1000 seconds. Expected detection rates of the high-redshift GRBs are 5 - 7 events $\mathrm{year}^{-1}\,\mathrm{sr}^{-1}$ for $z > 5$, and 0.3 - 0.5 events $\mathrm{year}^{-1}\,\mathrm{sr}^{-1}$ for $z > 10$, respectively. Therefore the ETCC will provide the insights to the massive star evolution in the early universe. For short duration GRBs, the ETCC has a sensitivity with a photon flux limit of 0.5 ph $\mathrm{cm}^{-2}\,\mathrm{s}^{-1}$, if we require a detection photon limit of 25 photons. The estimated detection rate of SGRBs with a luminosity higher than $10^{49}\,\mathrm{erg\,s}^{-1}$ which occur within a distance of 200 Mpc is about ~ 0.2 events per year in the all sky. The wide field ETCC will provide a promising chance to observe the electromagnetic counterparts of the gravitational wave sources.

Contents

Chapter 1

Introduction

The MeV gamma-ray sky in the universe is filled with astronomical explosive phenomena such as supernovae and gamma-ray bursts. The line gamma-ray photons produced by decay of radioisotopes are the unique probe to the existence of fresh nuclei. They are generated, for example, at the supernovae, which are the nucleosynthesis sites, and provide the insights to the 'driver' of the early period of the supernova explosion. Gamma-ray bursts (GRBs) are the brightest transients in the universe with a duration of about 0.1 to 1000 seconds and longer. GRBs occur at a cosmological distance, and therefore they can be used to the probe to the early universe, such as the star formation rate and the degree of ionization of atomic hydrogen. On the other hand, GRBs with a short duration of less than 2 seconds are thought to have common ancestors with a gravitational wave source, because the progenitors of the short duration GRBs are believed to be compact object mergers such as the coalescence of double neutron stars or blackhole and neutron star binary system. Therefore the simultaneous observation of the electromagnetic and gravitational waves is a key to the insights to the explosion mechanism of the compact system. Moreover, since the time when Hess discovered the cosmic rays coming from the universe in 1912, it has been investigated for a hundred year that how and where the cosmic rays are accelerated. For example, whether the high-energy electrons produce observed cosmic gamma rays or protons do is still an open question. This problem is thought to be solved by deep MeV gamma-ray observation, because the energy spectra in MeV region play a decisive role to distinguish the particles accelerated due to the detection of gamma rays from the decay of π^0. Thus, the MeV gamma-ray universe is the frontier in the high energy universe.

The observation of the universe in the MeV gamma-ray region is, however, immature. The all sky survey was performed by *CGRO*/COMPTEL, and found only $\sim$30 stable sources in the MeV band, while the *Fermi*/LAT recently detected more than 3000 sources at GeV region. We can point out two difficulties of the MeV gamma-ray observation in space. One

is the presence of huge background events in this energy band. The other is that there has been no proper imaging method based on optics for MeV gamma rays. Conventional MeV gamma-ray imaging detectors such as a coded mask imager, a collimating detector, and a Compton camera, are pseudo imaging detectors. Their point spread functions and background rejection capabilities are vague because they cannot determine the incident direction of gamma rays properly, which deteriorates the imaging performance in high background environment. To overcome these difficulties, we propose an electron-tracking Compton camera (ETCC) as a promising candidate to the new generation MeV gamma-ray telescope. The ETCC has a new concept to measure the two angles determining incident gamma-ray momenta completely photon by photon. Moreover, the ETCC has a strong background rejection ability using a particle identification. This ability was demonstrated by a balloon-borne experiment, SMILE-I, where the ETCC successfully obtained the fluxes of the diffuse cosmic and atmospheric gamma rays. Thus, the ETCC has the property of the background rejection capability with the true imaging method. On the other hand, the imaging capability of the ETCC for celestial sources has not been well investigated because the effective area of the SMILE-I/ETCC was too small to observe celestial sources with balloon experiments. The goal of the SMILE projects is to observe MeV gamma-ray universe with 100 times higher sensitivity than that of COMPTEL. In order to realize this, we must confirm the imaging ability of the ETCC for celestial sources with a middle-sized ETCC. Then, both the simulation for design of a large effective area, and the development of the middle-sized ETCC for the test of the imaging property are required. Thus, we plan to perform a one-day balloon-borne experiment to demonstrate the imaging property of the ETCC (SMILE-II) as the step for the future satellite-borne extended ETCC.

In this paper, we report on the development of the flight model ETCC for SMILE-II, and an ETCC simulator based on a Monte Carlo method. We tested both the detection efficiency of the gamma rays and the detection inefficiency of the gamma rays that interact with inactive volume of the detector. We also investigated the rejection capability of the neutron scattering events, which are the major background events for classical Compton cameras. Based on the detector simulation, the numerical calculation for the prospect of the future GRB observations to be performed with a satellite-borne ETCC is discussed.

Chapter 2

MeV gamma-ray astronomy

2.1 MeV gamma-ray sky in the universe

The all-sky survey in MeV gamma-ray region was achieved by *Compton Gamma-Ray Observatory (CGRO)* satellite launched in 1991 and revealed that the universe is full of energetic phenomena. COMPTEL, one of four instrument aboard *CGRO*, detected 32 stable source and 31 transient sources in MeV gamma-ray region, although EGRET, which is another instrument loaded on *CGRO*, detected 273 sources in GeV energy region [1, 2]. The list and map of the observed sources are shown in Table 2.1 and Figure 2.1. You note that the objects classified to gamma-ray bursts and active galactic nuclei are major sources in MeV band. As well as such extragalactic sources, there are also Galactic sources such as stellar mass blackhole candidates, gamma-ray pulsars, and supernova remnants. That is also supported from the all-sky survey in hard X-ray band (14-195 keV) performed by *Swift* satellite as shown in Figure 2.2 [3], which detected 1171 sources containing over 700 active galactic nuclei and over 400 gamma-ray bursts [3, 4]. Moreover, the *Fermi*/LAT (2008-) has performed the all-sky survey in sub-GeV and detected more than 3000 sources [5] as shown in Figure 2.3 [6]. The fact there is only one MeV all-sky survey yet and a quite small number of detected sub-MeV/MeV gamma-ray sources compared with hard X-ray and GeV regions are explained by poor sensitivity for this region as shown in Figure 2.4. If the all-sky survey in sub-MeV band with better sensitivity were realized, it must shed light on the good understanding of the sites and the mechanism of the MeV gamma-ray emission. In this chapter, we focus on the topics specific to the MeV gamma-ray region, line emissions from supernovae and massive stars, gamma-ray bursts, and cosmic MeV gamma-ray background.

Table 2.1— The detected sources with COMPTEL and EGRET [1, 2]

Type of source	COMPTEL		EGRET	
Spin-Down Pulsars	3	Crab, Vela, PSR 1509-58	6	Crab, Vela Geminga, PSR 1786-44, PSR 1055-52, PSR 1951+32
Other Galactic sources $\|b\| < 10^\circ$	7	Cyg X-1, Nova Persei 1992, GRO J1823-12, GRO J2228+61, GRO J0241+6119, Crab Nebula, Carina/Vela region	2	Cen X-3, Crab Nebula
Normal Galaxies			1	LMC
Active Galactic Nuclei	10	Cen A, etc.	77	Cen A, etc.
Gamma-Ray Line Source	7	SN1991T (^{56}Co), SNR RX J0852-4642 (^{44}Ti), Cas A (^{44}Ti), Vela (^{26}Al), Carina (^{26}Al), Cyg region (^{26}Al), RE J0317-853 (2.223 MeV)		
Unidentified Sources	5		186	
Total Number	32		273	
Gamma-Ray Burst	31		4	

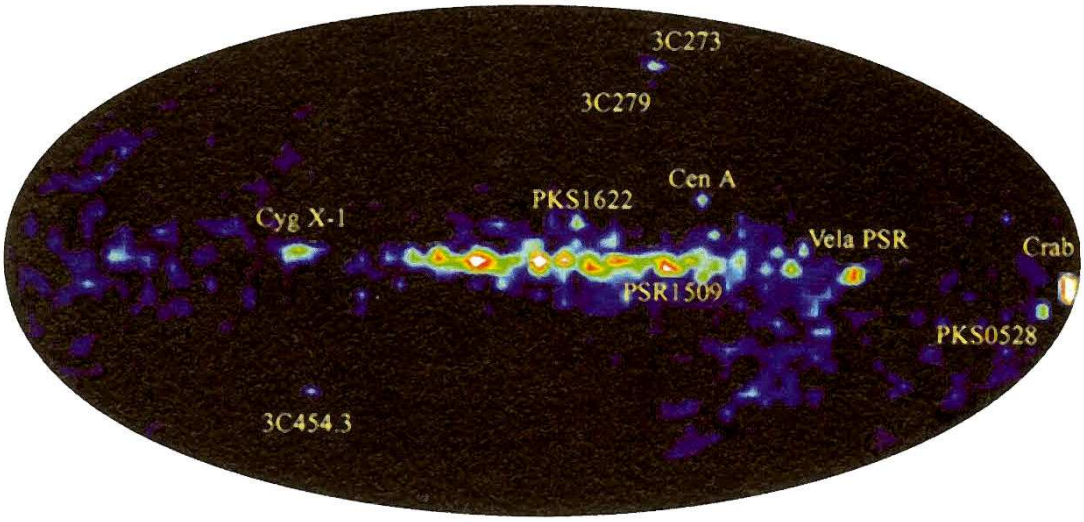

Fig. 2.1.— All sky map between 1MeV and 30 MeV derived by *CGRO*/COMPTEL [1].

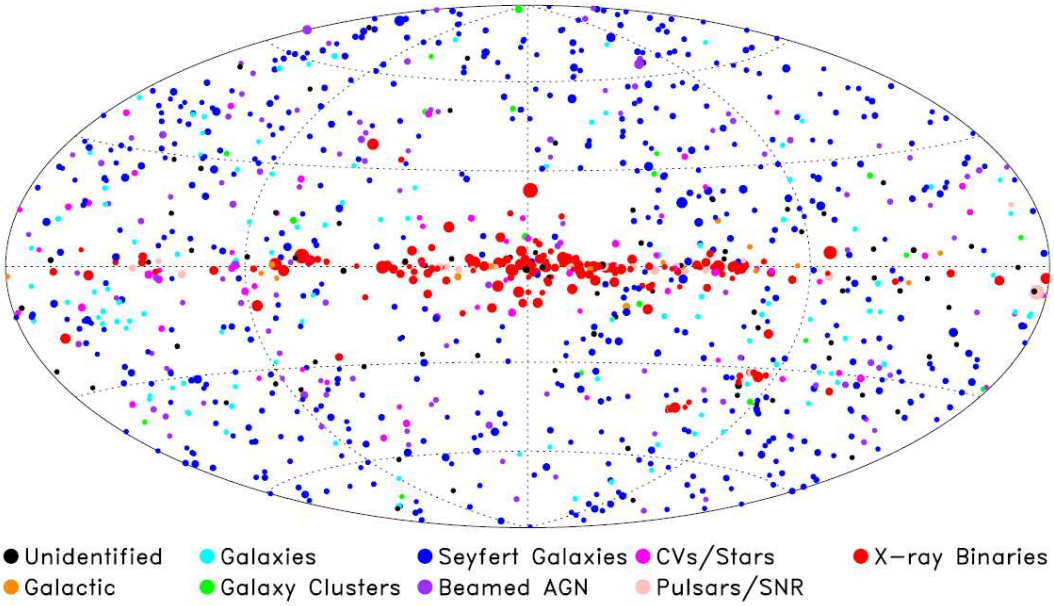

Fig. 2.2.— *Swift*-BAT 70-month-survey stable sources in 14 - 195 keV band [3].

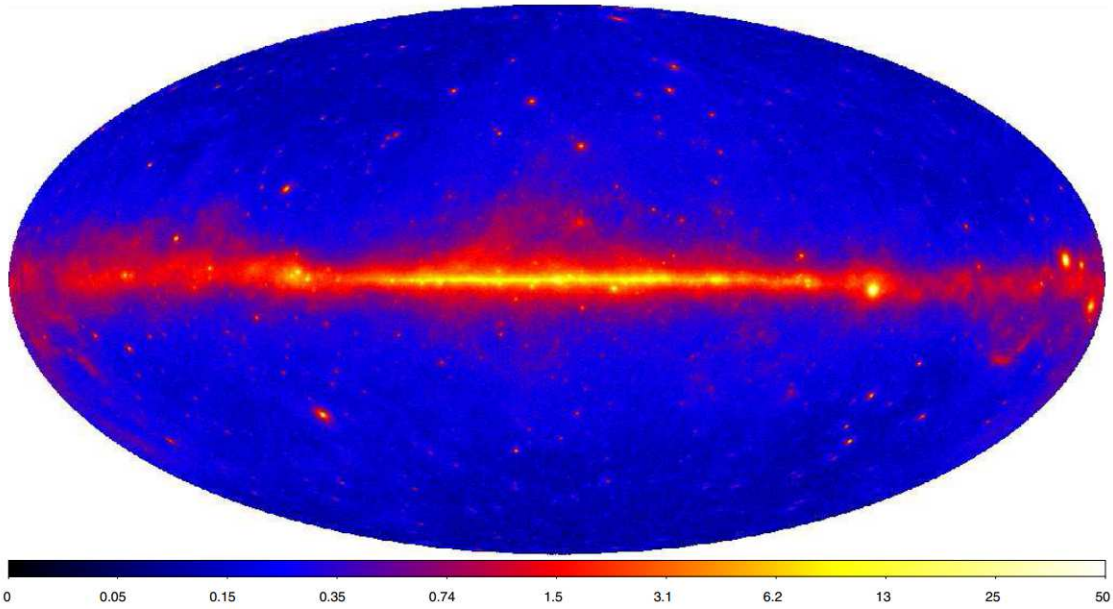

Fig. 2.3.— All sky map of the energy flux between 100 MeV and 10 GeV in units of 10^{-7} erg cm^{-2} s^{-1} sr^{-1}, derived by *Fermi*/LAT [6].

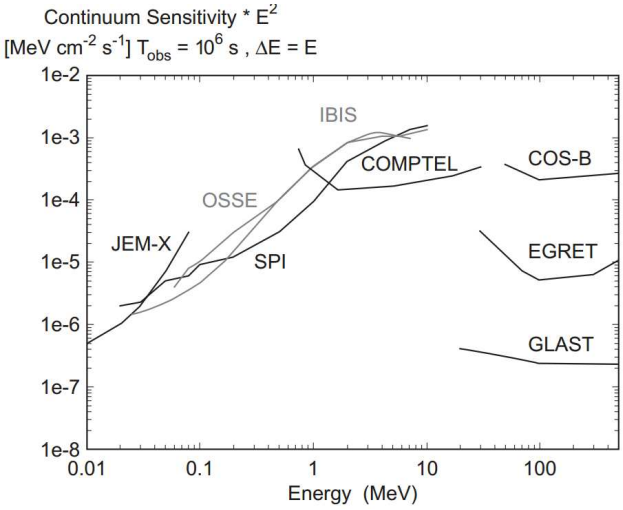

Fig. 2.4.— sensitivity for continuum in X-/gamma- ray region [7].

2.2 Line emissions from Supernovae and Massive Stars

Type Ic and II supernovae are explosive phenomena that occur during the last stage of the evolution of massive stars, and have been considered important sites of nucleosynthesis of heavier nuclides than helium. A detection of line gamma photons from supernovae is a promising probe to study the explosion mechanism. The first detection of such line gamma rays was realized by the observation of SN 1987A, which is a Type II supernova, by the gamma-ray spectrometer on the Solar Maximum Mission (SMM) satellite [8]. The spectrum that was derived by summation of the 36-day data showed the possible presence of the four line gamma-ray emissions from ^{56}Co decay, namely, 0.847, 1.238, 2.599, and 3.250 MeV (the last is a composite of three lines) with 3σ level, as shown in Fig. 2.5 left.

Recently, line gamma-ray emissions from a Type Ia supernova, SN 2014J, were detected [9]. A Type Ia supernova, which is considered to occur in binary system of a white dwarf and a star, produces constant peak luminosity due to the unique mass (Chandrasekhar mass limit) of white dwarfs that explode by accretion mechanism. Thus, the Type Ia supernovae are called as standard candles, and played a role of a distance indicator in cosmology. However, the physical process of the evolution and explosion mechanism is controversial. In the evolution process, it is thought that the companion star plays an important role. In the general hypothesis, when the dwarf star accretes mass from the binary companion star and the mass reaches the Chandrasekhar mass, the core of the dwarf is thought to reach the ignition temperature for nuclear runaway. Radioisotope ^{56}Ni, which is the last fusion product in this nuclear reaction, is produced with a mass of about one solar mass. ^{56}Ni decays to ^{56}Co with a time constant of a week, and then it decays to ^{56}Fe with a time constant with about 100 days. In the decay of ^{56}Co, line emissions of 847 keV and 1238 keV occur. The detection of line gamma-rays from SN 2014J showed that type Ia supernovae really are thermonuclear events.

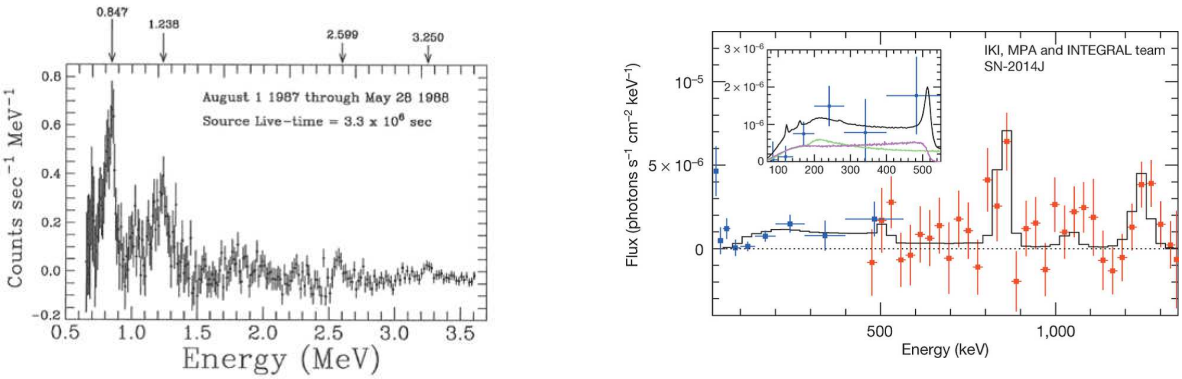

Fig. 2.5.— (Left) Gamma-ray spectrum of SN 1987A [8]. (Right) Gamma-ray spectrum of SN 2014J [10].

While line gamma-ray emissions from short-lived radionuclides give an insight to the explosion mechanism of supernovae, radioisotopes that have long decay constants of about a million years (See Table 3.1) such as ^{26}Al and ^{60}Fe are the tracer for the sites of the evolution of massive stars. They also provide constraint on nucleosynthesis in massive stars and supernovae. The main production sites of ^{26}Al and ^{60}Fe isotopes are believed to be the H layer that has a plenty of protons or the Ne-O layer where ^{25}Mg is produced. Generated ^{26}Al is released to interstellar medium by stellar winds and supernovae. For the massive stars such as Wolf-Rayet stars, with a mass above 30 solar mass, ^{26}Al produced at the H layer is emitted by the stellar wind. On the other hand, ^{60}Fe is believed to be generated by the neutron capture process of ^{58}Fe and ^{59}Fe, in the Ne-O layer through nuclear fusion or explosion. At the supernova explosion, it is also generated by the r-process at the He layer. In both cases, ^{60}Fe is generated at the deeper layer of the stars, and therefore the supply process of ^{60}Fe to the interstellar medium is only though to be the supernovae [11]. Because of their long decay time, they survive to be detected after the supernovae ejected them into interstellar medium.

CGRO/COMPTEL obtained the all sky map in the gamma-ray line of 1.809 MeV emitted from ^{26}Al [12]. One can see a diffuse component along to the galactic plane and some bright local regions. Based on the result of the COMPTEL observation of the ^{26}Al gamma-ray line, *INTEGRAL*/SPI obtained the spectra of the line gamma-ray of ^{26}Al in the galactic plane. The line emission on the galactic plane with an inner latitude of $|l| < 30$ degrees is brighter than that of the outer region, and this result is consistent with that obtained by COMPTEL [13]. Recently, the all sky map of ^{26}Al obtained by SPI was published, as shown in Fig. 2.6, and the ^{26}Al flux on the galactic plane was reported to be $3.3 \times 10^{-4}\,\mathrm{ph\,cm^{-2}\,s^{-1}\,rad^{-1}}$ [14]. Although the total mass of ^{26}Al in our galaxy had been estimated to be $2-3$ solar mass by the COMPTEL observation [15], there is uncertainty resulting from the uncertainty of the distance to the source. According to the observation by COMPTEL, the spatial distribution of massive stars in our galaxy is thought to have a dense structure, compared with the model that was used conventionally. By the observation performed by SPI, they reported the total mass of ^{26}Al to be $1.5-3.6$ solar mass, considering the effect of the uncertainty of the spatial distribution of the massive stars [16]. Calculating the ratio of the fluxes of ^{26}Al and ^{60}Fe, one can obtain the abundance ratio of these isotopes, which is useful to test the theoretical models of the nucleosynthesis in the star. RHESSI, which was a satellite for the observation of the Sun, obtained spectra from our galaxy to observe the line gamma-ray emissions from ^{60}Fe. They reported that there are excesses of 1.173 MeV and 1.332 MeV at 1.4σ and 2.4σ, respectively, and combining these two bands of the spectra the excess is at 2.6σ level [17]. Compared with the flux of ^{26}Al obtained by RHESSI, the flux of ^{60}Fe was estimated to be $9.7 \pm 3.9\%$ [17]. *INTEGRAL*/SPI observed the line gamma-ray emissions of 1.173 MeV and 1.332 MeV, and reported that the significance of these emissions is 4.9σ, and the corresponding flux ratio of ^{60}Fe to ^{26}Al is $14.8 \pm 6.0\%$ [18].

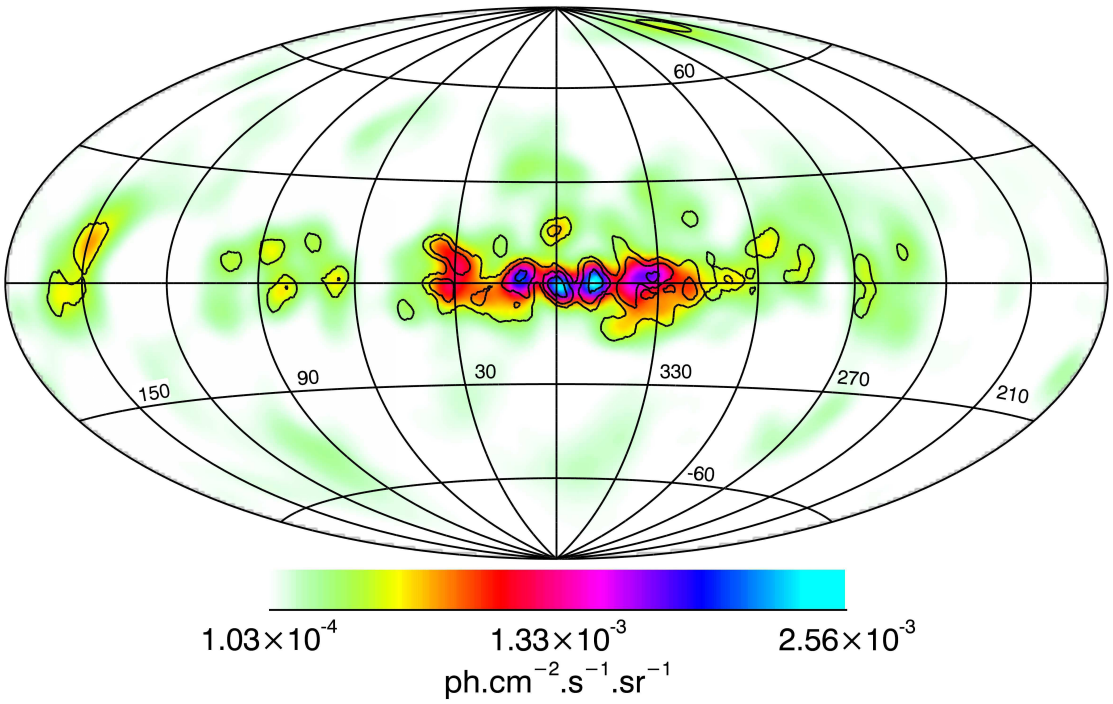

Fig. 2.6.— ^{26}Al sky map obtained by *INTEGRAL*/SPI [14].

The measurement of the flux ratio of ^{60}Fe to ^{26}Al was also performed by other detectors, and uncertainties still exist in the measurement, while the theories that explain the flux ratio also have uncertainty from complicated stellar evolution in late stages, nuclear reactions of neutron capture on unstable Fe isotopes, and explosive nucleosynthesis. For example, the prediction of the flux ratio by Timmes et al. (1995) is $(16 \pm 12)\%$, the one by Prantztos (2004) based on, e.g. Rauscher et al. (2002), Limongi & Chieffi (2003) is $(80 \pm 40)\%$, which is inconsistent with the measurement by SPI, and the one by Limongi & Chieffi (2006) is $(18.5 \pm 6.25)\%$, which is again consistent with the observational constraints [18]. We note that for the aspect of the observational side, there are large systematic errors due to the limit of the imaging resolution and signal-to-noise ratio, and thus observations with better quality data are strongly required.

2.3 Gamma-ray bursts (GRBs)

Gamma-ray bursts (GRBs) are the brightest phenomena in the universe. The first detection of a GRB was performed by a military satellite in the late 1960s [19], but for 30 years after that little progress was made in understanding them due to the very short transient. Thus even the distance to GRBs was not clear. The breakthrough came in the *CGRO* era by the Burst and Transient Source Experiment (BATSE) on *CGRO* [20], which observed directions of several thousand GRBs and revealed the isotropic distribution of the GRB on the sky as shown in Figure 2.7, This indicates the GRBs are not in Galactic. However, it remained unresolved whether GRBs are bright at other wavelengths or not, because the modest position resolution of BATSE of about 10 - 15 degrees [21] could not contribute follow-up observations. In 1996, BeppoSAX on the Italian-Dutch satellite was launched and enabled us to follow-up observations of GRBs with better position resolution within several arcminutes by the combination of wide field X-ray imager and four narrow field X-ray telescopes. The 'afterglow' after the prompt gamma-ray emission of the GRB was first discovered by the detection of GRB 970228 [22]. After the detection of the prompt X-ray emission lasting about 80 seconds, the narrow field X-ray telescope on board BeppoSAX observed the direction of GRB 970228 within 8 hours, and detected a X-ray transient fading with a power-law slope. That was the first detection of the X-ray afterglow. Optical images of GRB 970228 were taken by the William Herschel Telescope and the Isaac Newton Telescope, and the afterglow in optical and infrared band was detected for the first time [23]. Soon after that, the spectral analyses of afterglows of GRB 970508 whose prompt emission was detected by BeppoSAX, showed absorption lines associated with magnesium and iron corresponding with a redshift of $z = 0.835$ [24]. Thus GRBs were found to occur at cosmological distance. A redshift distribution of GRBs observed by *Swift* is shown in Fig. 2.8 [25]. Due to the association with massive stars as pointed out later, the GRB rate can be related to the star formation rate. The emission mechanisms of GRBs, however, have not been explained due to their unique temporal and spectral features as mentioned as follows.

Kouveliotou et al. pointed out that the durations of GRBs, t_{90}, defined as the time in which 5% to 95% of the burst fluence, has two populations using BASTE light curve data: Short GRBs (SGRBs) with $t_{90} < 2$ sec and Long GRBs (LGRBs) with $t_{90} > 2$ sec [27], as shown in Fig. 2.9. This bimodal distribution of the GRB duration has played a key role in GRB classification to investigate progenitors of GRBs. GRB 980425, a kind of LGRBs, occurred nearly simultaneously as SN 1998bw, providing the first evidence that some of LGRBs are associated with the death of massive stars [28]. On the other hand, SGRBs, such as GRB 050509b and GRB 050724, were detected in or near elliptical galaxies, which have ceased star formation long time before, suggesting that SGRBs are associated with old stellar populations and likely due to the merger of two compact stars such as two neutron

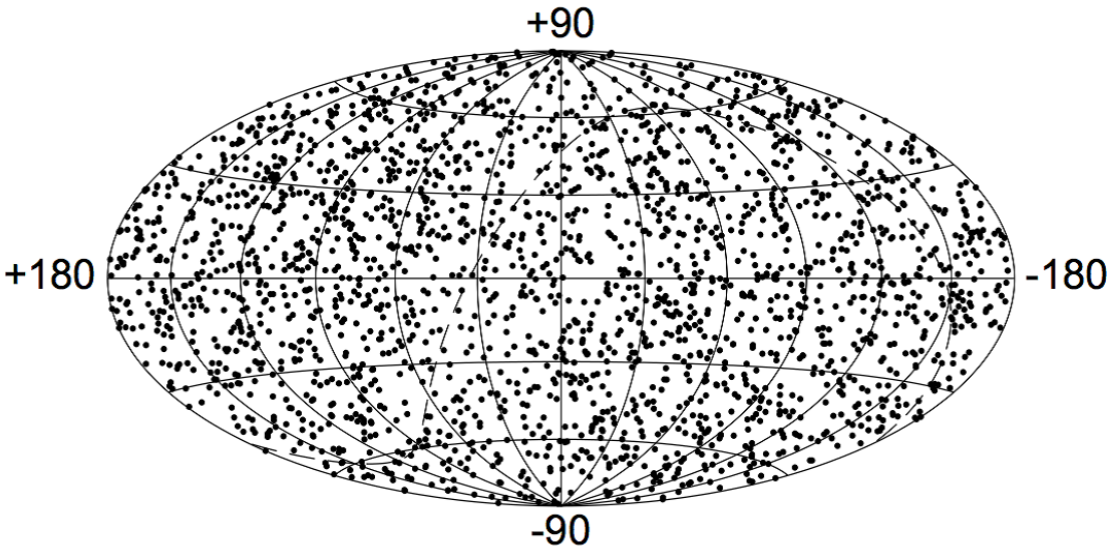

Fig. 2.7.— GRB position distribution obtained by BATSE [26].

stars or a neutron star and stellar black hole in a binary system [29, 30].

The *CGRO*/BATSE observtion also revealed the spectral feature of GRBs. Time-averaged GRB spectra are well described by empirical two power-laws joined smoothly at a given break energy, the Band function [33] as shown in Figure 2.10:

$$\frac{dN(E)}{dE} = \begin{cases} A\left(\frac{E}{100\,\mathrm{keV}}\right)^{\alpha} \exp\left(-\frac{E(2+\alpha)}{E_{\mathrm{peak}}}\right) & \text{if} \quad E < \frac{(\alpha-\beta)E_{\mathrm{peak}}}{(2+\alpha)} \equiv E_{\mathrm{break}} \\ A\left[\frac{(\alpha-\beta)E_{\mathrm{peak}}}{(100\,\mathrm{keV})(2+\alpha)}\right]^{(\alpha-\beta)} \exp(\beta-\alpha)\left(\frac{E}{100\,\mathrm{keV}}\right)^{\beta} & \text{if} \quad E \geq \frac{(\alpha-\beta)E_{\mathrm{peak}}}{(2+\alpha)} \end{cases}, \quad (2.1)$$

where α and β are low and high energy indices of the two power laws, respectively, E_{break} is the break energy of the power law, and E_{peak} is the peak energy at the νF_{ν} spectrum. The parameter α, β, and the break energy vary from GRBs as shown in Figure 2.11, and typical values are -1, < -2, and 200 keV, respectively [34].

To explain the emission regions of the prompt emission and the afterglow of GRBs, the internal-external shocks scenario has been proposed as shown in Figure 2.12 [35]. First, in terms of the very short timescales of GRBs, the size of the emitting region must be very small or be moving at relativistic velocities. If the total energy of typical GRBs are crammed in such a small space, the system will be opaque to promote the photon-photon pair creation process efficiently, which makes the bursts less luminous than that observed in MeV region. To resolve this problem, the emitting matter has been thought to travel at relativistic velocities instead. The related problem is evoked to the variability timescale of the light curves of GRBs. It is much shorter than the total duration of the bursts. The

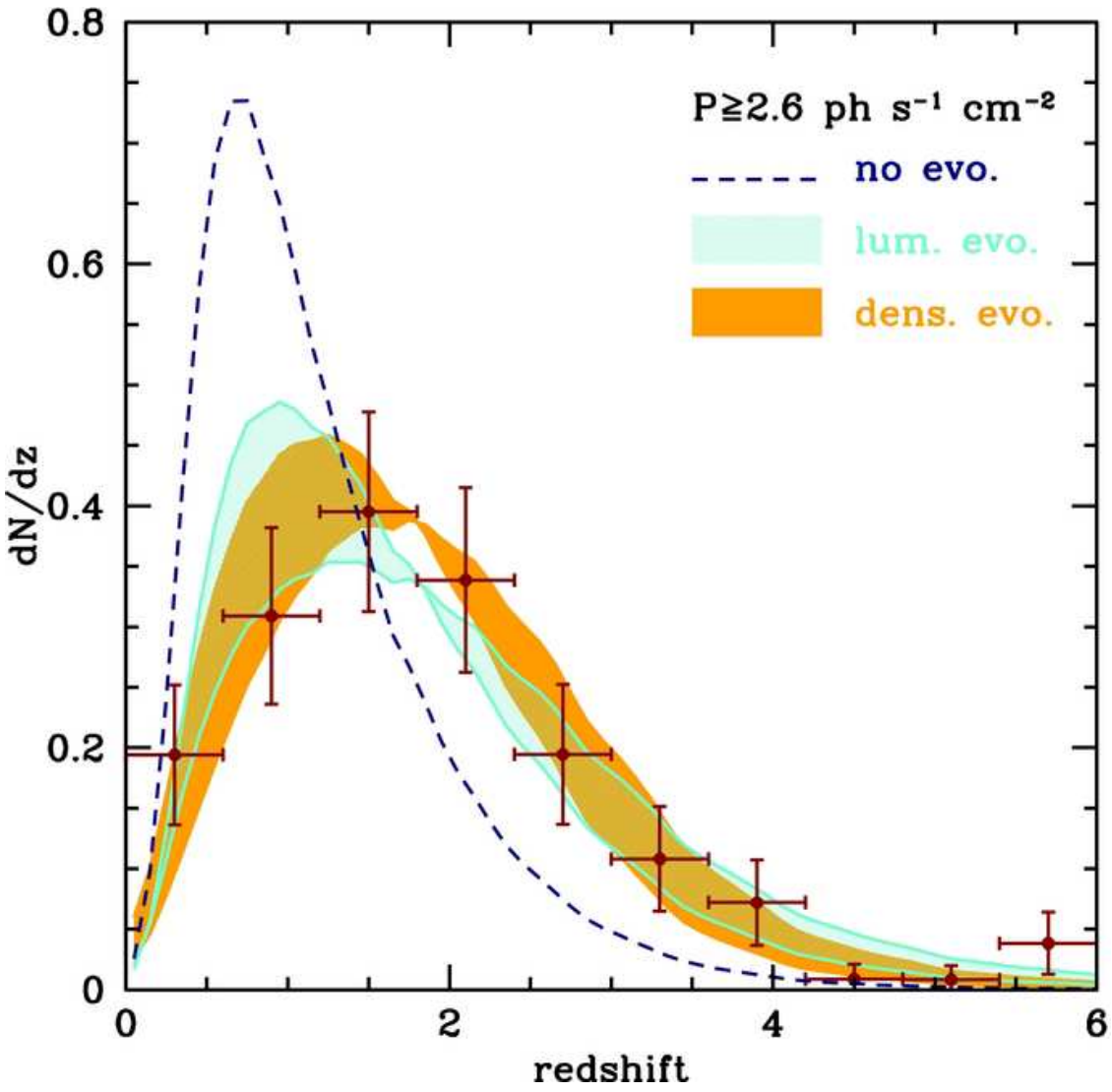

Fig. 2.8.— Normalized redshift distribution of GRBs with a photon flux greater than 2.6 photons $s^{-1}cm^{-2}$. Red points represents the observed redshift distribution. The dashed blue line shows the expected distribution for the no evolution case, and for luminosity and density evolution case, the light blue and dark orange regions show the model, respectively [25].

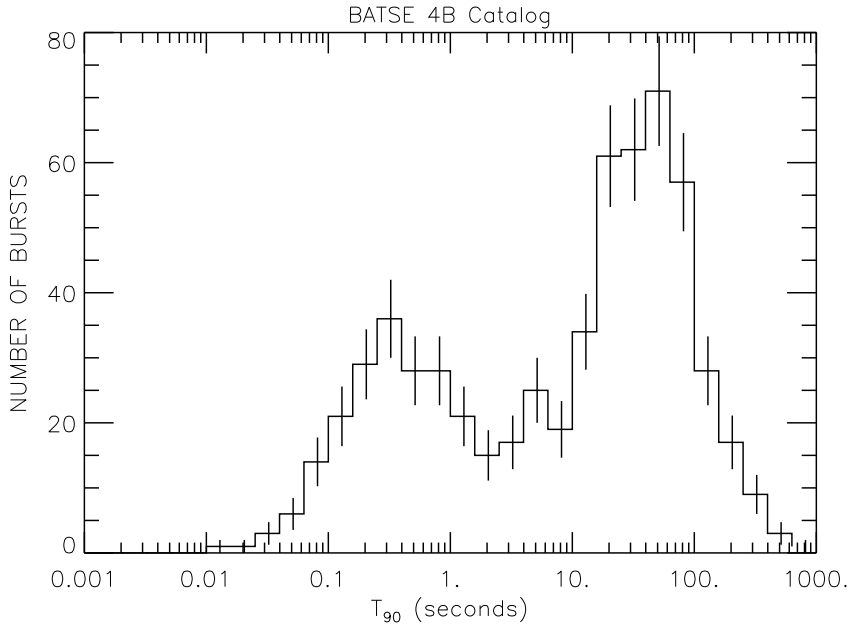

Fig. 2.9.— Duration distribution of 2704 BATSE bursts [31].

generally accepted explanation for such short variability in the system of relativistic matter, is that the collision of multiple shells moving at different velocities produces the prompt bursts, and it is so-called 'internal shocks'. The afterglow is thought to be emitted in a different region from the internal shocks: the 'external shocks', where the front of the shell collides the interstellar medium or the stellar wind of the central star.

An X-/gamma- ray polarization is another key to the understanding of the magnetic and geometrical structure at the site of the GRB jet. It was reported that there was a strong linear polarization with $80 \pm 20\%$ in the prompt gamma-ray emission from GRB 021206 [37], but in the opposition paper, the linear polarization was reported to be $41^{+57}_{-44}\%$ and they claimed that the data quality is insufficient to constrain the degree of the polarization [38]. The recent X-ray polarimetric observation performed by Gamma-Ray Burst Polarimeter (GAP) approached to solve the physical process involved in prompt emission. It successfully observed the polarization of the prompt emission of the GRB (GRB 100826A) with a polarization fraction of $27 \pm 11\%$, and the polarization angle changing with a 3.3σ confidence level during the burst as shown in Figure 2.13 [36]. The possible detection of the X-ray or gamma-ray polarization suggests that the prompt emissions of the GRBs are more likely to originate in synchrotron radiation, and the variability of the polarization angle suggests the direction of the magnetic field varies temporally or spatially, which would be explained by the presence of the patchy structure of the shells.

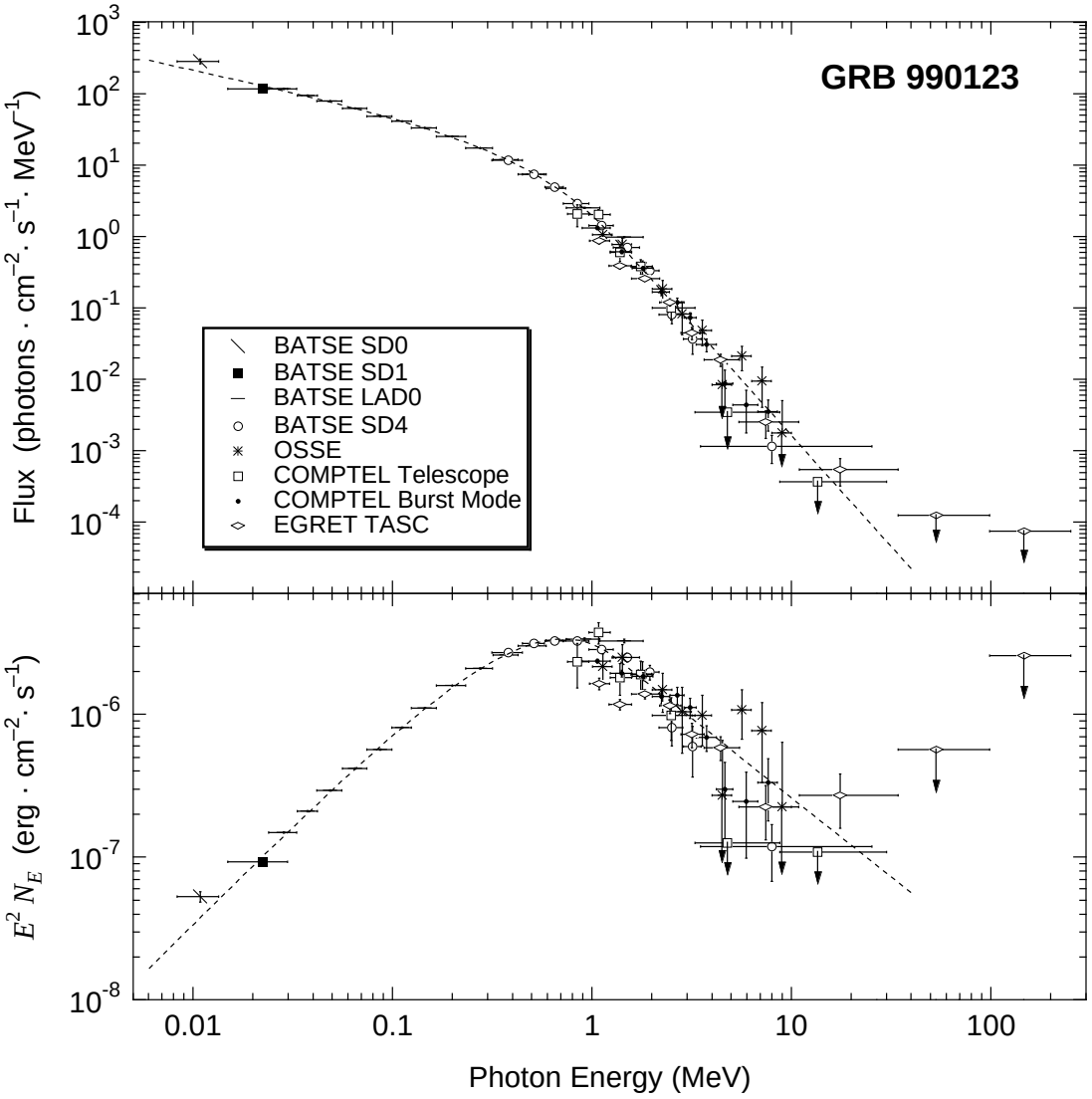

Fig. 2.10.— Spectrum of GRB 990123 [32].

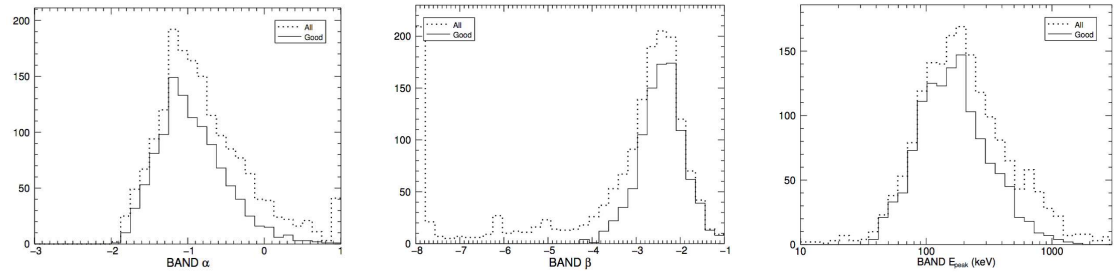

Fig. 2.11.— Distributions of α (left), β (center), and $E_{\rm peak}$ (right) from time-integrated GRB fluence spectra [34].

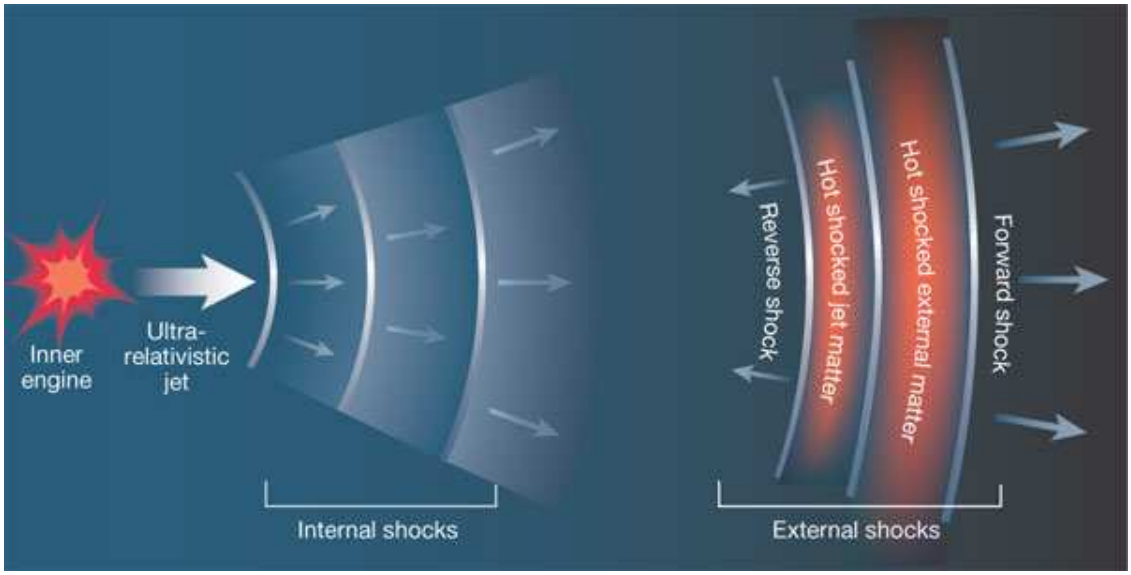

Fig. 2.12.— Schematic view of internal-external shocks scenario of GRBs [35].

Though the bimodal distribution of the burst duration suggested there are at least two types of the progenitors for GRBs, recent observations raised a question about this classical paradigm. LGRBs have the duration up to several hundred seconds, while a small number of events lasting over 1000 seconds have been detected and they are called Ultra Long GRBs (ULGRBs) [39, 40] as shown in Figure 2.14. Some of ULGRB, GRB 060218A and GRB 100316D, have emission of long lasting thermal components in X-ray band and very low $E_{\rm peak}$ value, which is very different from typical one. Virgili et al. performed a χ^2 test with the expected log-normal duration distribution determined by 591 samples of LGRBs detected by *Swift* to 11 samples of ULGRBs, yielding a probability of the accepting the null hypothesis of normality to 3.4%, suggesting that there is no current justification of the necessity of the new ULGRB population but they are just at the tail of LGRBs. On the other hand, the long durations may naturally be explained by the massive stars of much

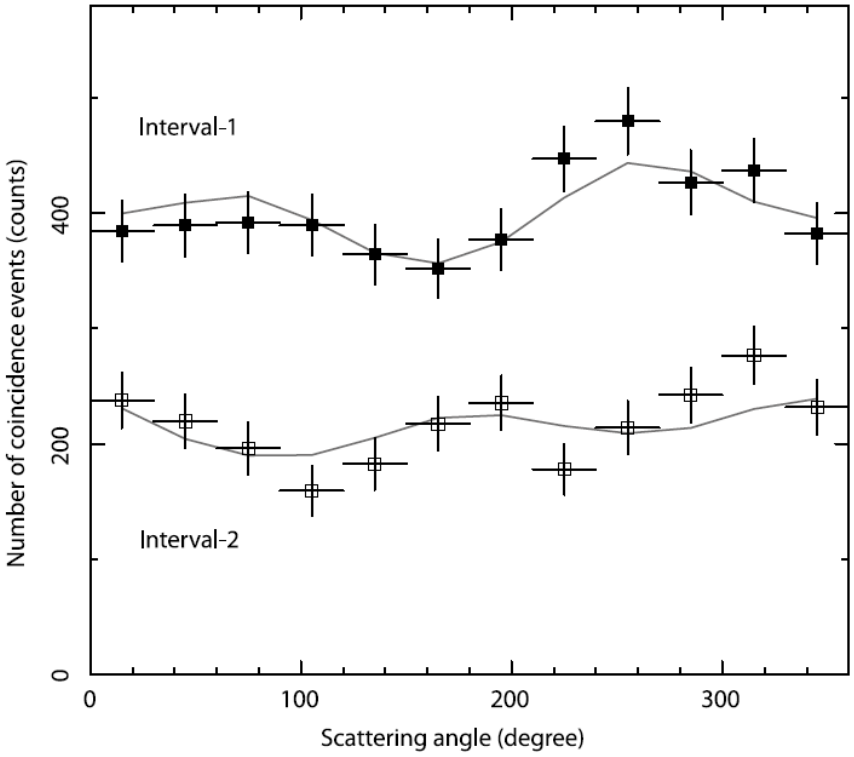

Fig. 2.13.— Polarization of GRB 100826A detected by GAP [36].

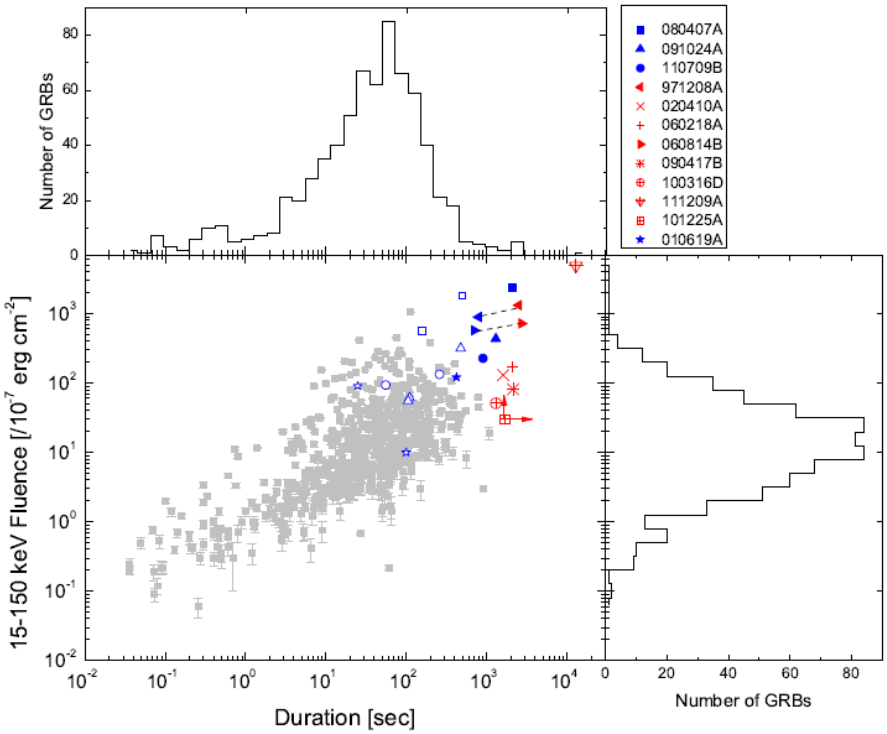

Fig. 2.14.— fluence and t_{90} distribution of GRBs [39].

larger radii than the progenitor of the 'normal' LGRBs which are thought to have compact Wolf-Rayet stars, requiring plenty of good observational samples to clarify if there is such a hitherto unrecognized population of the progenitors of the different type.

GRBs are also interesting subjects for the study of the early universe. In the early universe, where a high redshift of $z \gtrsim 7$, the first stars are thought to play crucial roles for reionization of the universe and production of metals. There are, however, a few observational ways to probe this dark age. The observation of quasars and galaxies performed by the Sloan Digital Sky Survey has been the major probe to cosmologically distant sources. For example, a CO emission was detected with radio observation by VLA from SDSS J114816.64+525150.3, at $z = 6.42$, at which cosmic reionization is just ending [41, 42]. However, the redshift distribution of quasars peaks at z of $2-4$, and the galaxies themselves are much dimmer than quasars. Alternately, GRBs are tremendously bright and occur in normal galaxies, and thus they play a role of the probe to the early universe with $z > 5$. GRBs detected by *Swift* show not a few percentage of GRBs are deteced at high redshift, and the highest being $z = 8.2$ [43]. Recently, Ghirlanda *et al.* provided the detection rates of high-z GRBs based on the model that reproduces the observed properties of GRBs detected by *Swift*, *Fermi* and *CGRO* in the hard X-ray and gamma-ray bands. According to that report, the detection rate of GRBs with a redshift higher than 5 is $\sim 10\,\mathrm{events\,year^{-1}\,sr^{-1}}$ for the fluence sensitivity of $1\,\mathrm{ph\,cm^{-2}}$ as shown in Fig. 2.15 [44]. The tens of the detections of high-z GRBs provide the information on the star formation rate in the early universe. Moreover, the first stars, so-called Population III (Pop III) stars, have not yet been directly observed, but it has been proposed theoretically that Pop III stars may produce GRBs [45, 46, 47]. One of the observational characteristics of Pop III GRBs is to have a very long duration of 10^4-10^5 seconds, typically [47, 48], and its total energy of the explosion is quite large of 10^{54} erg, but very long duration decreases its luminosity under the present detection limits.

Binary neutron star mergers are expected to emit gravitational waves (GWs) [49]. If the coincident observations of the GW and the prompt emission of the SGRB are realized, the mystery of the SGRB progenitor is solved. According to the observation performed by *Fermi*/GBM, SGRBs have a harder typical peak energy E_{peak} of ~ 490 keV than LGRBs [50]. Therefore, an observation in an energy band above such energy can catch the prompt emission from the SGRBs efficiently.

Recently, the first detection of GW was performed by the Laser Interferometer Gravitational-Wave Observatory (LIGO) on Sep. 14, 2015 [51]. The GW data was fitted by templates of black-hole binary mergers based on general relativity, and they concluded that the signal was emitted during the inspiral and merger of a binary black-hole. The obtained parameters are: $m_{\mathrm{BH},1} = 36^{+5}_{-4}\,M_{\mathrm{sun}}$, $m_{\mathrm{BH},2} = 29^{+4}_{-4}\,M_{\mathrm{sun}}$, and the luminosity distance to the source $d_L = 410^{+160}_{-180}\,\mathrm{Mpc}$. By an off-line analysis, it was reported that the *Fermi*/GBM detector measured a week transient event above 50 keV, which occurred 0.4 second after the

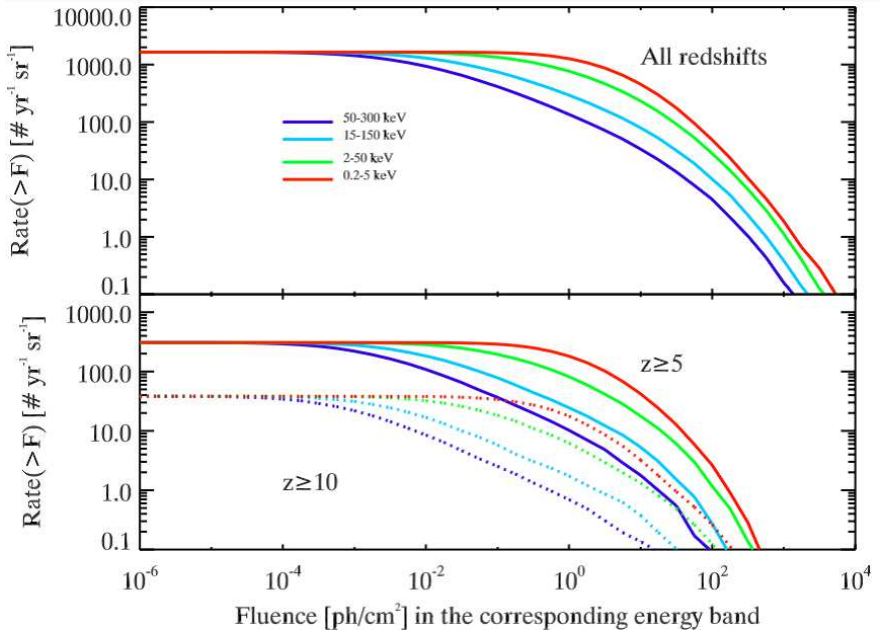

Fig. 2.15.— Cumulative distributions of the GRB fluence [44].

GW was detected as shown in Fig. 2.16, with a false alarm probability of 0.0022 [52]. On the other hand, the *INTEGRAL* observation as shown in Fig. 2.17 put upper limits on the gamma-ray and hard X-ray fluence of $F_\gamma = 2 \times 10^{-8}\,\mathrm{erg\,cm^{-2}}$ to $F_\gamma = 10^{-6}\,\mathrm{erg\,cm^{-2}}$ in the 75 keV - 2 MeV energy range for typical spectral models, which is 10 times dimmer than that by reported by the *Fermi*/GBM observation [53]. Though the identification and localization of the host galaxy of the GW events were not performed, they would provide insights to the formation mechanism of the progenitor.

The number of the SGRBs of which the redshift is measured by the optical spectroscopy is, however, as small as ~ 20 [54], and therefore it is not easy to determine the estimate of the formation rate of SGRBs. Tsutsui et al. (2013) pointed out that there is a correlation between the peak energy and the peak luminosity of SGRBs, as well as LGRBs, which is known as the $E_\mathrm{p} - L_\mathrm{p}$ correlation, or Yonetoku relation, but the luminosity is dimmer if the peak energy is the same:

$$L_\mathrm{p} = 10^{52.29\pm0.066}\mathrm{erg\,s^{-1}} \left(\frac{E_\mathrm{peak}}{774.5\,\mathrm{keV}} \right)^{1.59\pm0.11}, \tag{2.2}$$

where L_p is the isotropic equivalent peak luminosity. Using the peak luminosity L_p obtained by Eq. 2.2 and measured peak flux F_p, we can calculate the luminosity distance to the source d_L by $L_\mathrm{p} = 4\pi d_L^2 F_\mathrm{p}$, and also obtain the redshift. Hereafter we call that calculated redshift as 'pseudo-redshift'. The left side in Fig. 2.18 shows the cumulative redshift distributions up

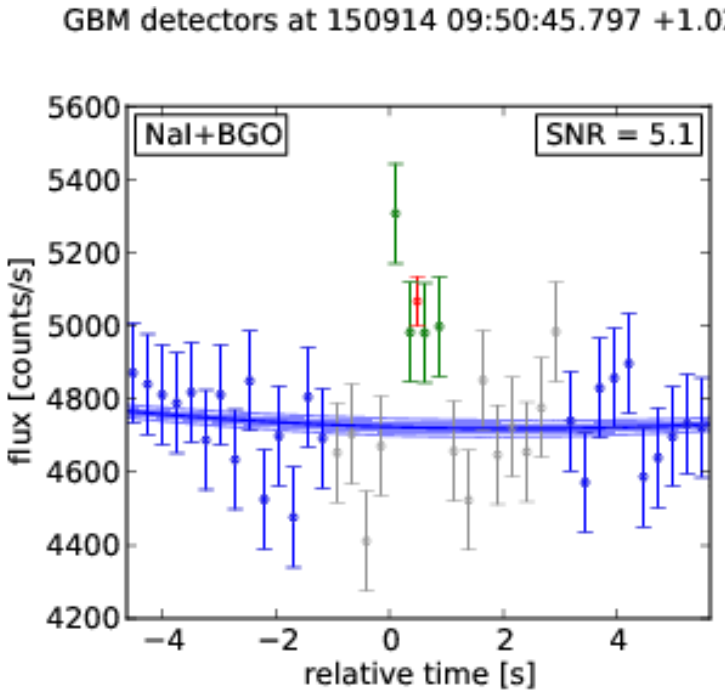

Fig. 2.16.— Count rates detected by *Fermi*/GBM as a function of time relative to the start of GW 150914 [52].

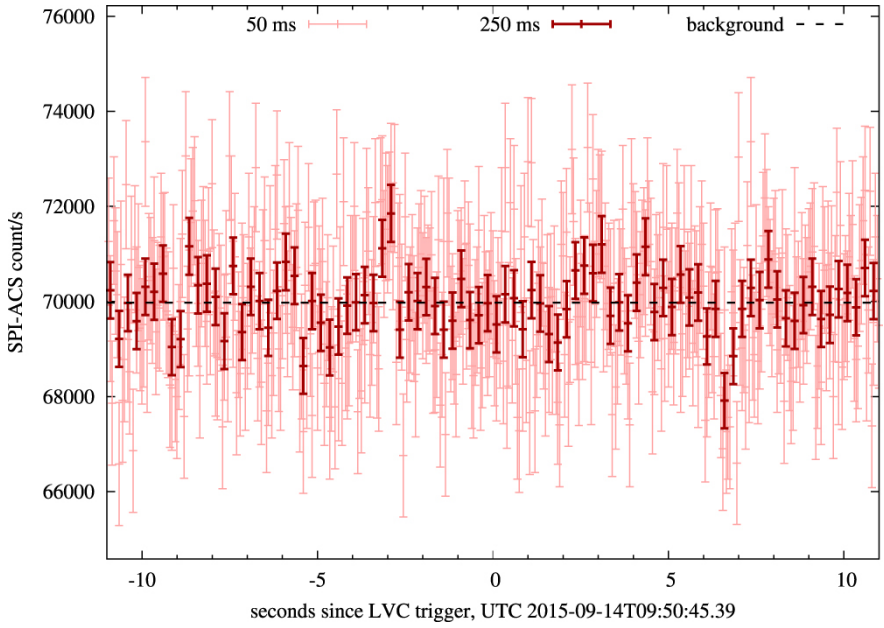

Fig. 2.17.— *INTEGRAL*/SPI-ACS lightcurve in ±10 seconds around GW 150914 trigger time [53].

to $z = 1.14$, with a flux limit of $\sim 4 \times 10^{-6}\,\mathrm{erg\,cm^{-2}s^{-1}}$. The black and the red lines are for 45 BATSE data with pseudo-redshifts and 22 known redshift samples observed by HETE-2 and *Swift*/BAT, respectively. The gray solid lines behind them show possible error regions estimated by 100 Monte Carlo simulations. We can see a good agreement among the red, black, and gray lines in the entire region, A Kolmogorv-Smirnov test between the red and black lines shows that the probability that the two curves arise from different distributions is 79.4%, and the error region in gray lines covers the red line. This suggests that the $E_\mathrm{p} - L_\mathrm{p}$ correlation for SGRBs is a good distance indicator. The formation rate of SGRBs is shown on the right side in Fig. 2.18. The red line is best estimation and 100 gray lines are the one from the Monte Carlo simulation. The local event rate of SGRBs with a luminosity above $10^{50}\,\mathrm{erg\,s^{-1}}$ in observer's frame at $z = 0$ is $6.3^{+3.1}_{-3.9} \times 10^{-10}\,\mathrm{events\,Mpc^{-3}yr^{-1}}$. If we assume the beaming angle of SGRBs is 6 degrees, which is suggested from four estimations of the jet opening angles from GRB 130603B, GRB 051221, GRB 111020A, and GRB 090426, the corresponding gravitational wave event rate is ~ 3.9 events per year for < 200 Mpc, within which the Advanced LIGO-Virgo network can observe the binary neutron star merger.

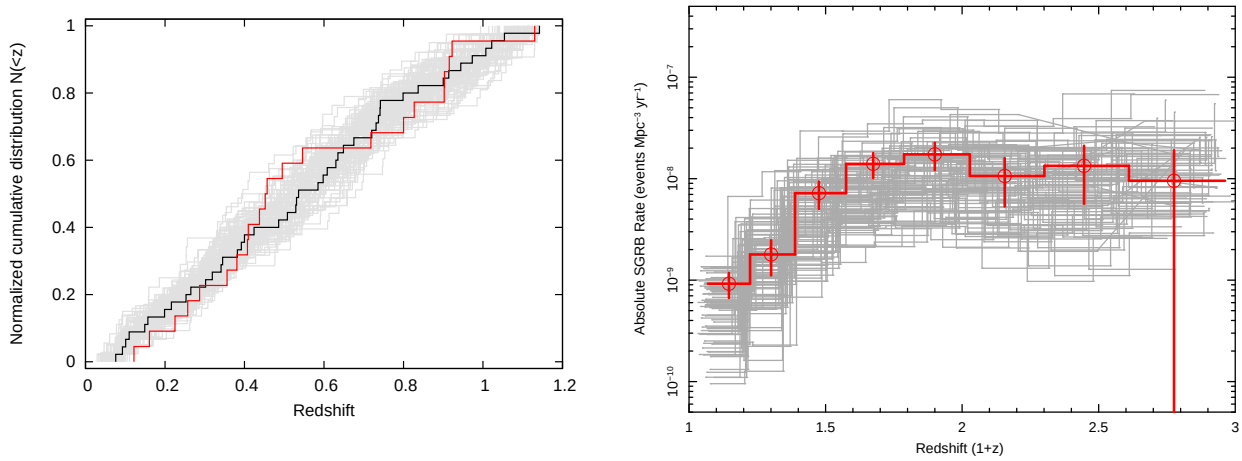

Fig. 2.18.— (Right) Cumulative redshift distribution of SGRBs up to $z = 1.14$, with a flux limit of $\sim 4 \times 10^{-6}\,\mathrm{erg\,cm^{-2}s^{-1}}$. The black and the red lines are for 45 BATSE data with pseudo-redshifts and 22 known redshift samples observed by HETE-2 and *Swift*/BAT, respectively. (Left) Formation rate of SGRBs with a luminosity above $10^{50}\,\mathrm{erg\,s^{-1}}$ [55]. The red line is best estimation and 100 gray lines are the one from the Monte Carlo simulation.

2.4 Cosmic MeV gamma-ray background

The diffuse cosmic X-ray background (CXB) from extragalactic region was first discovered about 50 years ago [56], and believed to be the superposition of the photons from the accretion process of active galactic nuclei. After the discovery of the CXB, Compton Gamma-Ray Observatory revealed that the gamma-ray sky is also bright for any direction. Above 100 MeV, the diffuse gamma-ray background is thought to be the superposition of the photons produced in the jets of AGNs [57, 58]. At near 1 MeV, on the other hand, the origin is in the mystery. In that band, the photons of a few hundreds of keV scattered up from UV photons in the accretion disks of the AGNs by hot corona near the accretion, are thought to be observed. However, the corona is basically thermal and therefore the cutoff energy should be present below 1 MeV, while observed flux is smoothly connected to the power law spectrum at higher energy region, as shown in Fig. 2.19. Therefore there are two scenarios that explain the origin of the cosmic MeV gamma-ray background. One is the non-thermal electrons in coronae above the accretion disks of Seyfert galaxies, and the other is the blazars that are bright at MeV gamma-ray region. One of the keys to deciphering the origin of that background is a measurement of the angular power spectra of anisotropy of the cosmic gamma-ray background [59] as shown Fig. 2.20. Obviously, the all-sky observation with low background is required to approach to this.

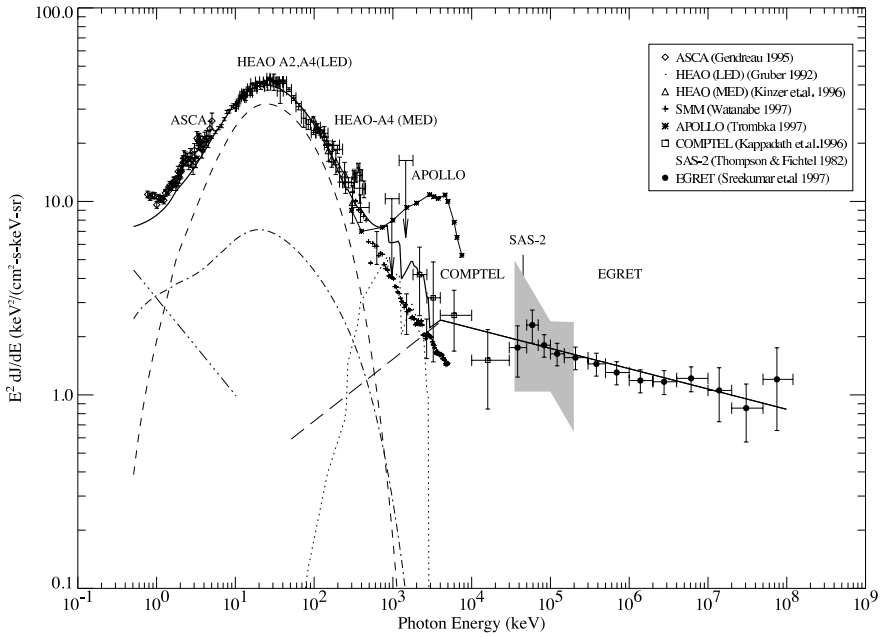

Fig. 2.19.— Multiwavelength spectrum of extragalactic diffuse gamma-ray emission [60].

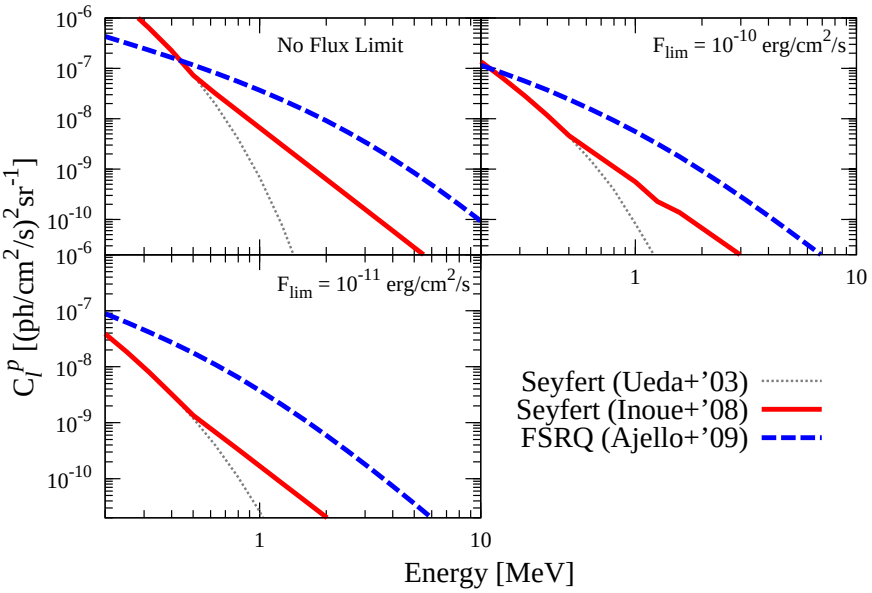

Fig. 2.20.— Predicted poisson term of the angular power spectrum of the cosmic MeV gamma-ray background at 200 keV - 20 MeV [59].

Chapter 3

Sub-MeV/MeV gamma-ray observation

3.1 Radiative process of gamma rays

Thermal radiation is the emission from electromagnetic waves resulting from the kinetic interaction among atoms and molecules as charged particles in the matter. If the radiation-emitting body and its surface are thermodynamic equilibrium and the all radiations are perfectly absorbed on its surface, the matter is called 'black body' and the radiating spectrum is described as follows:

$$I_\nu = \frac{8\pi h\nu^3}{c^3}\frac{1}{e^{h\nu/k_{\rm B}T}-1}, \tag{3.1}$$

where h and $k_{\rm B}$ are the Planck's and Boltzmann's constants, respectively, and T is the temperature of the matter. The typical frequency or energy of photon on the black body distribution is $h\nu \sim k_{\rm B}T$. In case of $h\nu = 1$ MeV, the corresponding temperature is $\sim 10^9$ K, with equilibrium between electron-positron pair creation and annihilation. Though there has been no observation of black body radiation with such a high temperature so far, it is thought to be realized in the inside of supernovae and the neighborhood of black holes.

Non-thermal process is another process of radiation for MeV gamma-ray region. One of the non-thermal emission processes is taken place in the presence of a magnetic field, known as synchrotron radiation. When a relativistic particle travels through the magnetic field B, the particle is accelerated by B, and radiates. The total emitted radiation is written as

$$P_{\rm synch} = \frac{4}{3}\sigma_T c\beta^2\gamma^2 U_B, \tag{3.2}$$

where $\sigma_T = 8\pi r_0^2/3$ is the Thomson cross section, and $U_B = B^2/8\pi$ is the magnetic energy density.

If a photon is scattered by an electron with sufficient kinetic energy compared to the photon, net energy may be transferred from the electron to the photon. This process is known as inverse Compton scattering. The radiation in a given photon energy density $U_{\rm ph}$ is

$$P_{\rm compt} = \frac{4}{3}\sigma_T c\beta^2\gamma^2 U_{ph}. \tag{3.3}$$

Radiation owing to the decceleration of an electron in the electric field of the nucleus is known as bremsstrahlung. For the single-speed electron, the total spectrum for a medium with ion density n_i, electron density n_e, and a fixed electron speed v, is

$$\frac{dW}{d\omega dV dt} = \frac{16\pi e^6}{3\sqrt{3}c^3 m^2 v} n_e n_i Z^2 g_{ff}(v,\omega), \tag{3.4}$$

where m and Z are the mass and atomic number of the ion, respectively, and $g_{ff}(v,\omega)$ is the correction factor or Gaunt factor. For the 'thermal bremsstrahlung', which is referred as the average of the single bremsstrahlung over a thermal distribution of speeds, the emission per unit volume per unit time per unit frequency is described as

$$\frac{dW}{dV dt d\nu} = \frac{2^5\pi e^6}{3mc^3}\left(\frac{2\pi}{3km}\right)^{1/2} T^{-1/2} Z^2 n_e n_i e^{h\nu/k_{\rm B}T}\bar{g}_{ff}, \tag{3.5}$$

where $\bar{g}_{ff}(T,\nu)$ is a velocity averaged Gaunt factor. $\bar{g}_{ff}$ is of order unity for $u \equiv h\nu/k_{\rm B}T \sim 1$ and is in the range 1 to 5 for $10^{-4} < u < 1$.

Radioactive nuclei commonly emit gamma rays at specific energies due to the radioactive decay or de-excitation processes. These nuclear reaction can be formally described as

$$X^* \longrightarrow X + \gamma \tag{3.6}$$

for de-excitation, and

$$X^* \longrightarrow Y^* + e^+ \longrightarrow Y + \gamma \tag{3.7}$$

for radioactive decay. Table 3.1 shows examples of these processes listing the nuclei and the energies of line emissions. Radioactive isotopes are thought to be produced in cosmic sites of nucleosynthesis, such as stellar interiors, supernovae, and interstellar space, while excited nuclei are thought to be produced by the collision of cosmic rays with interstellar gas or dust. Therefore the observation of these line spectra are undoubted evidence of the pion or ion acceleration.

Cosmic rays are also considered to produce gamma rays with the interstellar medium by hadronic process via neutral pion production:

$$\begin{array}{rcl} p + p & \longrightarrow & p + p + \pi^0 \\ \pi^0 & \longrightarrow & \gamma + \gamma. \end{array} \tag{3.8}$$

Table 3.1— The gamma-rays by nuclear transitions [1, 61, 62]

process		Energy [MeV]
De-Excitation	$^{12}C^*$	4.438
	$^{14}N^*$	$2.313, 5.105$
	$^{16}O^*$	$2.741, 6.129, 6.917, 7.117$
	$^{26}Mg^*$	1.809
	$^{56}Fe^*$	$0.847, 1.238, 1.811$
radioactive decay	^{56}Ni (6.10 d)	$0.158, 0.270, 0.480, 0.759, 0.812$
	^{56}Co (77.2 d)	$0.847, 1.238, 2.598$
	^{57}Co (271.7 d)	$0.122, 0.136$
	^{44}Ti (63 y)	1.157
	^{26}Al (7.4×10^5 y)	1.809
	^{60}Fe (1.5×10^6 y)	$1.173, 1.333$
capture	$n + {}^1\mathrm{H} \rightarrow {}^2\mathrm{D} + \gamma$	2.223

When a proton with an energy of E_p is hit to a static proton, the energy threshold for the neutral pion production yields:

$$E_p - m_p c^2 > 2m_{\pi 0}c^2 + \left(\frac{m_{\pi 0}}{2m_p}\right) m_{\pi 0}c^2 \approx 280\,\mathrm{MeV}. \tag{3.9}$$

Here m_p and $m_{\pi 0}$ are the rest mass of the proton and the neutral pion, respectively. The photon spectrum originating in neutral pion decay exhibits a feature of the rest energy of the neutral pion. The photon spectrum of a single-energy neutral pion is flat between $\frac{m_{\pi 0}c^2}{2}\sqrt{(\frac{1-\beta}{1+\beta})}$ and $\frac{m_{\pi 0}c^2}{2}\sqrt{(\frac{1+\beta}{1-\beta})}$ in the laboratory frame, at which the center of the energy is the half of rest energy of the neutral pion of $\approx$70 MeV in log-scale. When the pion spectrum is described by a power law spectrum, the photon spectrum have a bump structure at 70 MeV. Thus, the detection of the 70 MeV bump structure is a strong evidence of the proton acceleration. Therefore the observation in the MeV gamma rays are expected to present the most reliable evidence for the determination of the cosmic ray origin.

An electron-positron annihilation is an important gamma-ray source in MeV region. If a positron is produced in some way, it may form a two body bound state with an electron in the matter. That bound state is known as a positronium. The ground state of the positronium has two possible configurations of the different relative orientations of the spins of the electron and the positron: the singlet and triplet states. The singlet state with parallel spins has a lifetime of 125 picoseconds and decays preferentially into two gamma rays of the energy of 511 keV for each. On the other hand, the triplet state with antiparallel spins

has a lifetime of 142 ns and decays into three gamma rays with a continuum spectrum. The positron production processes are assumed to be β^+-decay, decay of π^+, the positron-electron pair creation from high energy gamma rays with an energy of above 1 MeV in a strong magnetic field such as the both of type Ia and II supernovae and the neighborhood of the black hole, and the collision of hadronic antiparticles with normal matter. Examples of the β^+-decay isotopes are ^{26}Al, ^{44}Ti, ^{60}Co, ^{13}N and ^{18}F. The line emission of 511 keV is therefore a key to probing the site of nucleosynthesis and cosmic-ray origins. It, however, may be strongly emitted by the decay of the radioactive isotopes produced by cosmic rays hitting the instrument of the satellite, which make it difficult to estimate the amount of cosmic origins quantitatively.

3.2 Interaction between gamma rays and matter

For the observation of celestial MeV gamma rays, an instrument must be in space in order to escape the absorption of the air. To observe celestial MeV gamma rays in the high altitudes, moreover, gamma rays cannot be captured and reflected by mirrors in the same ways as visible light and X-rays because the wavelength of the gamma rays is too short. Instead, one have to resolve the kinematics of the particle reaction to obtain the incident direction and energy of the gamma ray.

High-energy photons lose their energy while passing through matter with the electromagnetic interaction, to give kinetic energy to the electron in the matter or create the charged particles. All the things we can know about the incident photon is the ionization loss by these charged particles. There are three processes in the interaction between X/gamma rays and matter: photoelectric absorption, Compton scattering, and pair creation. These cross sections depend on the both energy of the X/gamma rays and the atomic number of the matter Z, which indicates that it is necessary to select appropriate material for the detector depending on the gamma ray energy range. The cross sections with the fixed Z number, argon ($Z = 18$), is shown in Fig. 3.1 and Fig. 3.2 shows the dependence of the dominant interaction on the photon energy and Z.

The photoelectric absorption is a dominant interaction of photons with the energy less than 100 keV. In this process, a photon provides all energy to a electron in the atom, which is called photoelectron, is ejected from the atom. When a photon with an energy of E_0 makes a photoelectron with a kinetic energy of K_e, it yields

$$K_e = E_0 - E_{\rm bind}, \tag{3.10}$$

where $E_{\rm bind}$ is the binding energy of the photoelectron in the atom. If E_0 is higher than the binding energy of the K shell, the probability of the interaction with an electron in K shell

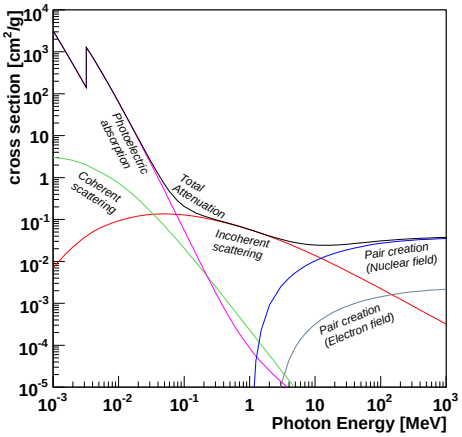

Fig. 3.1.— The cross sections between gamma rays and argon ($Z = 18$) [63]

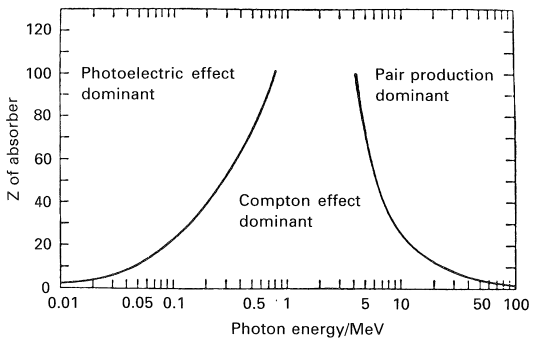

Fig. 3.2.— The dependence of the dominant interaction on the photon energy and Z [64].

is highest, of which the cross section of a K shell electron is:

$$\sigma_K = 4\sqrt{2}Z^5 \left(\frac{8\pi}{3}r_e^2\right)\left(\frac{e^2}{4\pi\varepsilon_0\hbar c}\right)^4\left(\frac{m_e c^2}{E_0}\right)^{7/2}, \tag{3.11}$$

where σ_K is proportional to Z^5 and $E_0^{-7/2}$, and r_e is the classical electron radius: $r_e = \frac{e^2}{4\pi\epsilon_0 m_e c^2}$. If E_0 is less than the binding energy of K shell, the photon interacts with an L shell electron. Therefore, near the K shell binding energy, the energy dependence of the cross section has a large discontinuity in the spectrum in an edge (Figure 3.1). Simultaneously a binding electron in the higher energy level trends to transit to the empty level by emitting an X-ray. The energy of the emitted X-ray is equal to the energy difference of those two levels. Also sometimes an electron of the nearly same energy is ejected instead of the X-ray emission, which is called Auger electron.

In the energy band from a few hundred keV to 10 MeV, the dominant interaction is the Compton scattering, which is an elastic scattering of a gamma-ray and an electron. In the Compton scattering, the incident gamma-ray provides a part of the initial energy to an electron, which runs away as a recoil electron, and the scattered gamma ray brings the remaining energy. When the gamma-ray in the energy of E_0 makes Compton scattering with a free electron, the energy of the scattered gamma-ray is

$$E' = \frac{E_0}{1 + \frac{E_0}{m_e c^2}(1 - \cos\phi)}, \tag{3.12}$$

and the energy of the recoil electron is

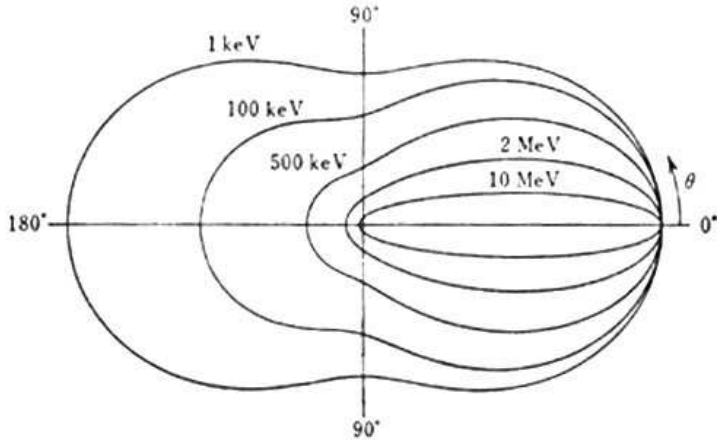

Fig. 3.3.— The angular distribution of Compton scattering [64]

$$K_e = E_0 - E' = \frac{\frac{E_0}{m_e c^2}(1-\cos\phi)}{1+\frac{E_0}{m_e c^2}(1-\cos\phi)} E_0, \tag{3.13}$$

where ϕ is a scattering angle. The angular distribution of the scattered gamma-rays is represented by the differential scattering cross section as follows,

$$\frac{d\sigma}{d\Omega} = Z r_e^2 \left(\frac{1}{1+k(1-\cos\phi)}\right)^2 \left(\frac{1+\cos^2\phi}{2}\right) \left(1+\frac{k^2(1-\cos\phi)^2}{(1+\cos^2\phi)\,[1+k(1-\cos\phi)]}\right), \tag{3.14}$$

where σ is the cross section, Ω is the solid angle and $k = \frac{E_0}{m_e c^2}$. Then the cross section is proportional to Z. The angular distribution is shown in Figure 3.3, where you note that the forward scattering is dominant when E_0 is higher.

In a real material, electrons have the finite momentum of the orbit in the atom, and then, the gamma-ray scattered at the fixed angle from a monoenergetic source have some fluctuation in their energy (the "Doppler broadening", see section 4.3.3).

If the gamma-ray energy exceeds twice of the rest mass of the electron, a pair of an electron and a positron are created with the interaction between the photon and an electric field around the nucleus. This process is called a pair creation, which is a dominant interaction of the photons above 10 MeV. The energies of an electron and a positron emitted from the photon of the energy E_0 must be satisfied with the following equation in the high energy region,

$$E_0 = E_- + E_+ + 2m_e c^2. \tag{3.15}$$

The cross section is proportional to Z^2.

3.3 Basics of MeV gamma-ray Imaging

In the wavelength region of X-ray and gamma-ray, the refractive indices are lower than but very close to 1 except for soft X-rays, and therefore simple lenses or mirrors cannot be used for focusing X-/gamma- rays. Though reflection and diffraction are used to focusing of the X-rays, they are not suitable for gamma-rays due to too shallow incident angle and therefore too long focal length in space. Instead, other techniques have been managed to develop to ensure the incident direction of gamma rays. To identify incident photons from a particular source or region of the sky, a couple of methods are very common, collimators, coded aperture masks, and Compton cameras for the MeV gamma-ray band.

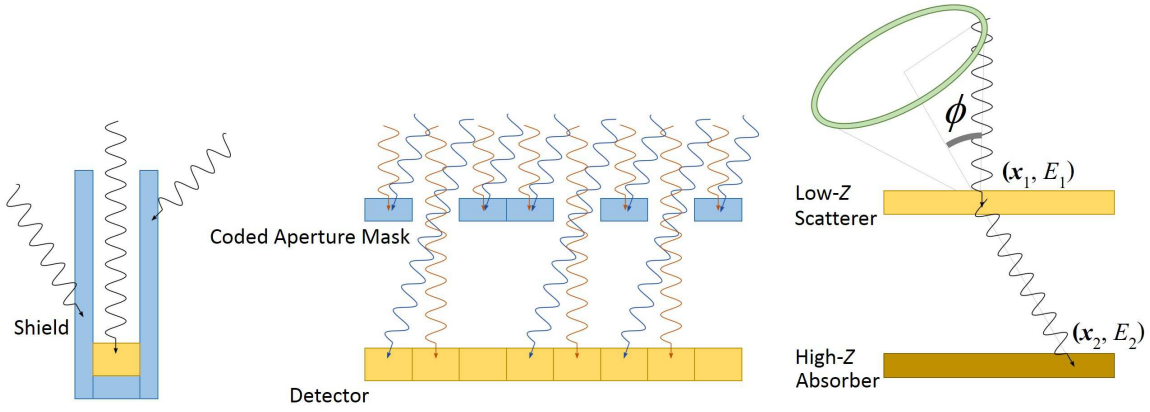

Fig. 3.4.— Schematics of three imaging methods, collimators (left), coded aperture masks (center), and Compton cameras (right).

Collimators, where the shield made of optically thick material partially covers a detector, only allow photons from certain angles to reach the detector, as shown on the left in Figure 3.4. To make a narrow field-of-view, a tube-type shape is adopted for the shield. The collimator can only measure an intensity of a narrow field-of-view by one shot, and therefore screening of the sky is necessary to obtain the intensity map.

Coded aperture mask imaging detectors consist of a mask placed in front of the X-/gamma- ray detector. The mask is made of optically thick material that stops the gamma-rays but only about half of the mask is covered. When a gamma-ray source irradiates gamma rays to the detector, about half of them are stopped by the coded aperture mask. The detector then measures the 'shadow' pattern of the coded aperture mask. Since the projected pattern on the detector varies depending on the position of the gamma-ray source as shown on the middle in Figure 3.4, one can reconstruct the source position using a mathematical calculation. When the gamma rays come with the incident direction of j and

the intensity of s_j, the intensity of the detector d_i on the position index i, is described with the known response matrix of the coded mask M_{ij} as

$$d_i = \sum_j M_{ij} s_j + b_i, \tag{3.16}$$

where b_i is the background intensity. If one can estimate b_i properly, s_j is derived from the deconvolution of the equation (3.16). In stead of deriving the deconvolution matrix directly, one can also reconstruct the source image by the pattern matching between the mask pattern and the derived shadow, which should have the same pattern with an appropriate translation. Formally, one can reconstruct the image s'_j by calculating the cross correlation between the mask pattern and measured image:

$$s'_i = \sum_j M_{i+j} d_j. \tag{3.17}$$

As indicated in Fig. 3.2, Compton scattering is the major interaction in the material for gamma rays of several hundreds of keV. Therefore events with scattering in the mask and detector become background to reduce the signal to noise ratio (SNR) for for energy band above about 100 keV. It is obvious that we need many events in order to gain an appropriate statistics for d_i to determine the incident photon direction, not by a single or a few events. These defects are less important in the case of observing a bright transient source with a high SNR. The nature of the wide field-of-view of coded aperture imaging system is also suitable for detecting transient events. On the other hand, those defects may be critical for observing steady and faint MeV gamma-ray sources due to the background contamination from the off-source region.

A Compton camera measures the physical process of Compton scattering to detect gamma rays event by event. It consists of two position-sensitive detectors, a scatterer and an absorber. If an incident gamma ray is scattered by the scatterer and absorbed in the absorber, the scatterer of the classical Compton camera measures the kinetic energy E_1 and vertex point $\boldsymbol{x}_1$ of the Compton-recoil electron and the absorber measures the energy E_2 and absorption point $\boldsymbol{x}_2$ of the scattering gamma ray. The energy and scattering angle of the incident gamma ray, E_0 and ϕ yield,

$$E_0 = E_1 + E_2, \tag{3.18}$$

$$\cos\phi = 1 - m_e c^2 \left(\frac{1}{E_2} - \frac{1}{E_1 + E_2} \right). \tag{3.19}$$

The direction of the scattering gamma-ray is determined to be $\boldsymbol{x}_2 - \boldsymbol{x}_1$. Since the atomic number dependences on the cross sections for Compton scattering and photoelectric absorption are $\propto Z$ and $\propto Z^5$, respectively, the minimization and maximization of the atomic number of the matters for the scatterer and absorber, respectively, is important for any

Compton cameras. Otherwise, for example, if one choose the high-Z matter as the scatterer, the events of which the incident gamma-rays scatter in the 'absorber' and are absorbed in the 'scatterer', become background because of the misapplication to the Compton scattering kinematics. Therefore, the liquid-organic scintillator, which is a molecule made of light materials, is one of most suitable materials for the scatterer of Compton cameras. Since the two parameters of the direction of the recoil electron is not measured, the reconstructed direction of the incident gamma-ray is limited in a circle (called an event circle as shown on the right in Figure 3.4). Also, there remain no redundant physical parameters for the check of the validity of the event reconstruction. Therefore, it is difficult for classical Compton cameras to separate the correct and incorrect reconstructions.

Chapter 4

Challenges to sub-MeV/MeV region

4.1 Compton Gamma-Ray Observatory (CGRO)

Compton Gamma-Ray Observatory (CGRO) was the satellite mission for the gamma-ray observation launched in 1991 by NASA. It had a weight of 17,000 kg and was in orbit with an altitude of 450 km from 1991 to 2000. CGRO loaded four different types of gamma-ray detectors: the Burst and Transient Source Experiment (BATSE), the Oriented Scintillation Spectrometer Experiment (OSSE), the Imaging Compton Telescope (COMPTEL), and the Energetic Gamma Ray Experiment Telescope (EGRET). Here we introduce the descriptions of the OSSE, COMPTEL, and BATSE as ~ 1 MeV band detector except for the EGRET, whose energy range is higher than 20 MeV.

COMPTEL is a kind of Compton cameras that consists of forward liquid-organic and backward NaI(Tl) scintillators with geometrical areas of 4188 cm^2 and 8744 cm^2, respectively, as shown in Fig. 4.1. The energy range of COMPTEL is $0.8 - 30$ MeV, and the effective is $20 - 50$ cm^2 if no event selections are applied to the data. Although the effective area is as small as tens 20 cm^2, the sensitivity of COMPTEL has ever been best in the MeV gamma-ray band, suggesting that restricting the source region by the Compton camera imaging is important for better sensitivity. As explained later, the background event rejection was carried out by restricting the time of flight of the scattered gamma ray from the upper to the lower detector.

OSSE consists of the 4 units of identical detectors using the combination of collimator and scintillator methods. Figure 4.2 shows the schematic view of the one detector of OSSE [66]. The main detector consists of the NaI(Tl) crystal, with a diameter of 33 cm and a thickness of 10.2 cm) and the CsI(Na) crystal with a thickness of 7.6 cm. Utilizing the differing scintillation time decay constants, it can distinguish the gamma-ray events occurring

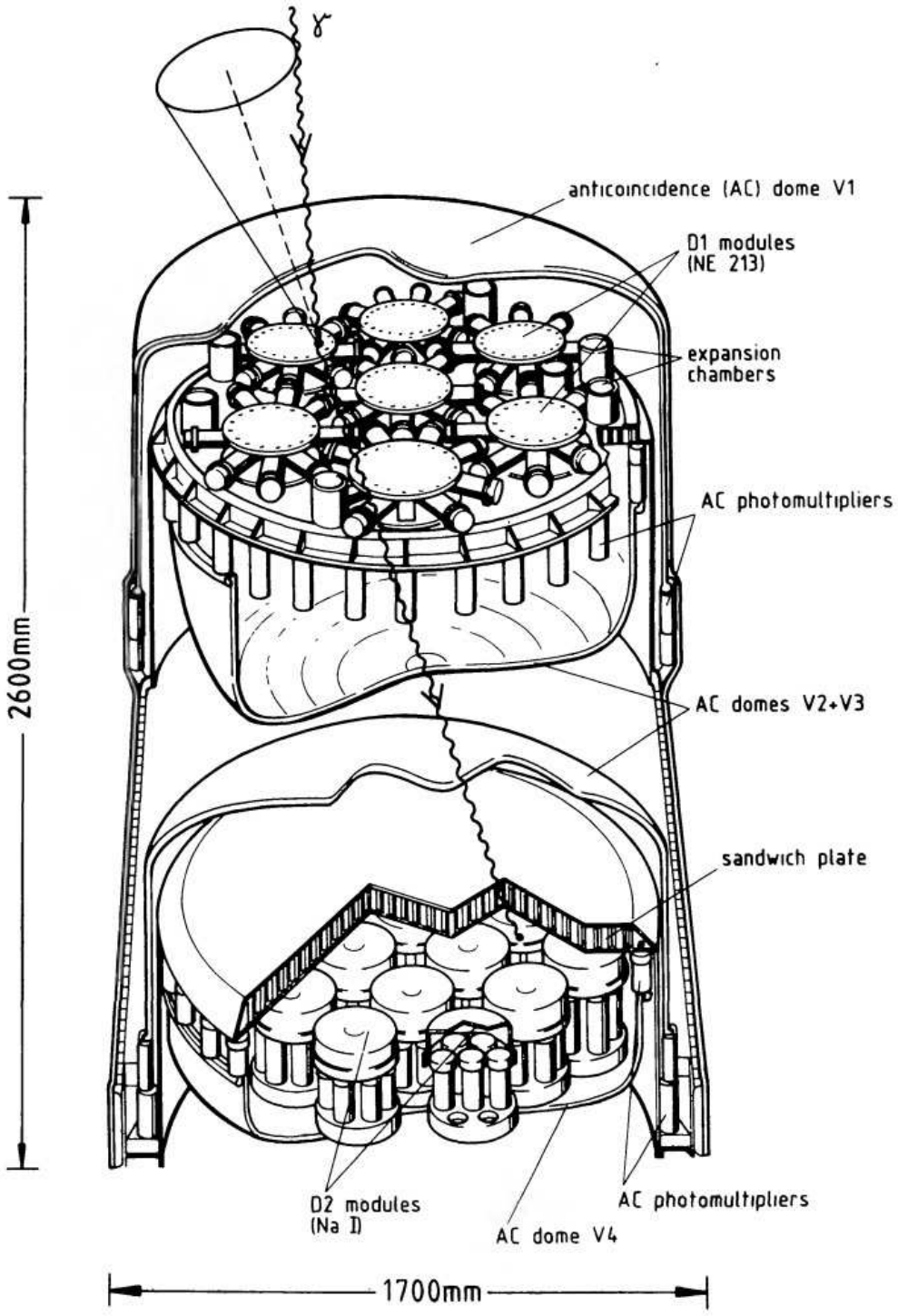

Fig. 4.1.— Schematic view of the COMPTEL instrument [65].

in the NaI portion and background events in the CsI portion by applying pulse shape analysis. In front of the Nal(Tl) crystal, a passive tungsten collimator was mounted. there was the annular shield of 8.5 cm thick NaI(Tl) crystal mounted around the main detector and the tungsten collimator, which rejects the gamma-ray background from the inner detector by the coincidence between inner and veto counter. For the rejection of charged particles, a thin plastic scintillator with a 0.6 cm thickness was also placed on the collimator. OSSE had an energy range from 0.1 MeV to 10 MeV and had a FOV of $3.8° \times 11.4°$ (FWHM). Since each unit of the OSSE did not have an imaging ability, it was unsuitable for the observation of diffuse sources and the objects near the Galactic plane compared with point-like sources. Moreover, such collimation method has a disadvantage of heavy mass due to the large veto counter and heavy passive collimator. The weight of OSSE is 1820 kg.

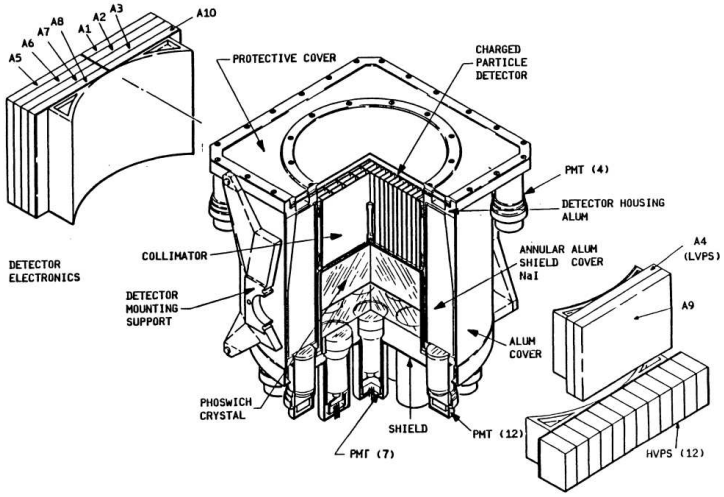

Fig. 4.2.— Schematic view of the OSSE instrument [67].

BATSE consists of eight identical modules. Each module has two NaI(Tl) scintillation detectors: a Large Area Detector (LAD) that is optimized for sensitivity and direction response, and a Spectroscopy Detector (SD) for energy resolution and coverage, as shown in Fig. 4.3 [68]. The LAD comprises a disk of NaI(Tl) scintillation crystal with a diameter of 20 inches and a thickness of one-half inch, mounted on a three-quarters inch layer of quartz. On the front of the crystal, plastic scintillator with a thickness of three-quarters inch is mounted as a anticoincidence shield to reduce the background events due to charged particles. On the back side of the crystal, a light collimator is installed that leads photons to three 5-inch diameter photomultiplier tubes. A lead and tin shield is inside of the light collimator to reduce the background gamma rays entering the back side. The SD consists of 5-inch diameter NaI(Tl) crystal mounted on a 5-inch diameter photomultiplier tube directly, and on the top of the crystal, a beryllium window with a diameter of 3 inches and a thickness of

50 mils is installed for high efficiency down to 10 keV. Scintillator pulses from the LADs are input to readout circuit with a lower-level discriminator of near 20 keV, and used to construct 128-channel spectra. In the case of SDs, the 256-channel spectra are constructed. BATSE detects gamma-ray bursts when the count rate of the eight LADs increases significantly above background on each of three time scales: 64 ms, 256 ms, and 1024 ms. A nominal time scale for the calculation of the background counting rate is 17.4 seconds, and a nominal statistical significance level required to determine the burst detection is 5.5 sigma [69].

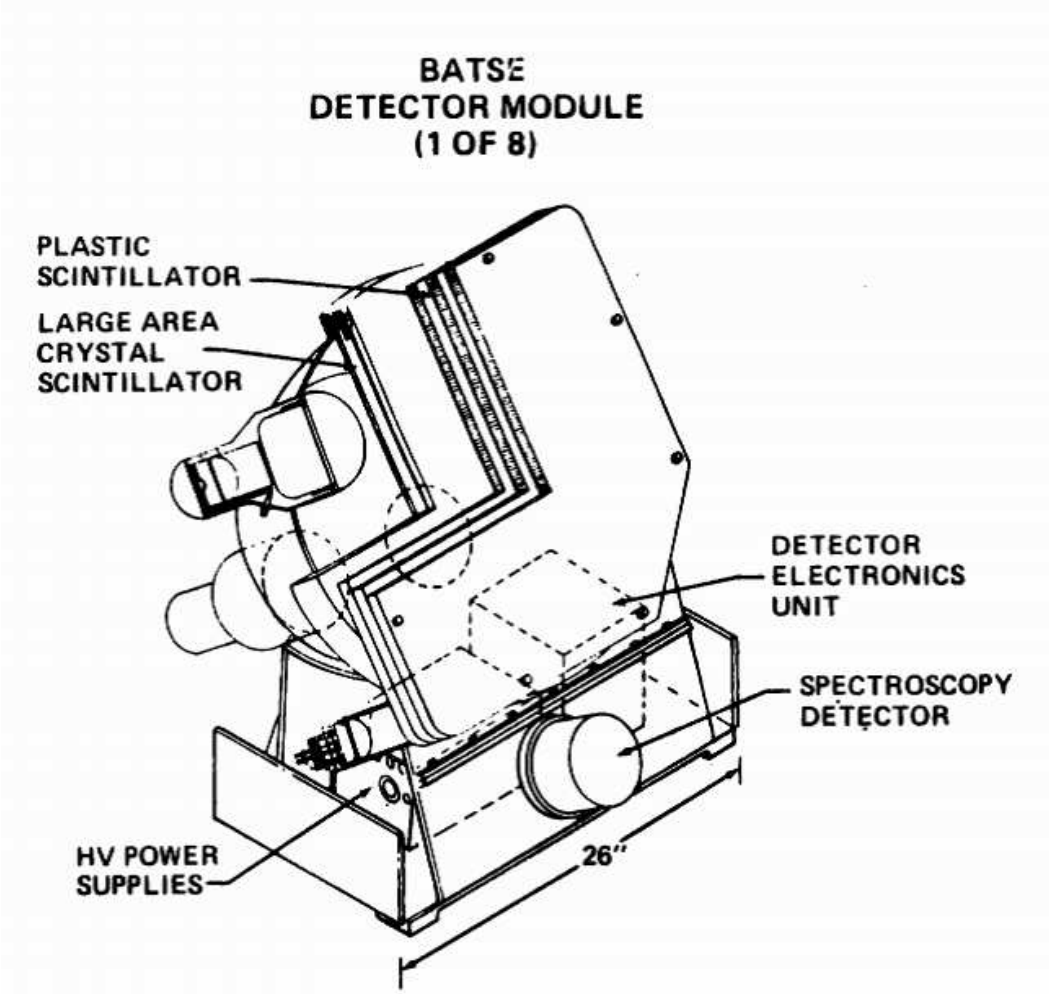

Fig. 4.3.— Schematic view of the BATSE instrument [68].

4.2 Difficulties on MeV gamma-ray observation in space

4.2.1 Huge background

In space, cosmic rays interact with the instruments and satellites to produce radioactive isotopes, electrons, and positrons. Then, they produce large amount of gamma rays by the nuclear reaction and Bremsstrahlung. In this way, cosmic rays are converted to MeV gamma-rays by the satellite itself. To make matter worse, high transmittance of MeV gamma rays causes the difficulty of shielding of them. Moreover, since Compton cameras require in principle the coincidence events between the forward and backward detectors as the candidates of Compton scattering, there are various kinds of background events irrelevant to the gamma-ray Compton scattering.

Actually, Weidenspointer *et al.* studied the detail of the origins of background in COMPTEL by simulation, and reported there are 6 types of major backgrounds [70] as shown in Fig. 4.4. The following shows each process:

A Internal Single Photon: Gamma-rays, which are produced at the inside of the detector by neutron capture or by radioactive isotopes (like ^{40}K), may make Compton scattering in the forward detector, and its scattered gamma-rays are absorbed in the backward detector.

B External Single Photon: Gamma-rays are produced at another detectors or the satellite platform by neutron capture, decay of radioactive isotopes and scattering, and then they may make Compton scattering in the forward detector and its scattered gamma-rays are absorbed in the backward detector.

C Internal Multi-photon: Multi-photons are produced by the interactions, like $^{27}\mathrm{Al}(n,\alpha)^{24}\mathrm{Na}$ or $^{27}\mathrm{Al}(n;n',\cdots)^{27}\mathrm{Al}$. Then some photons may hit the forward detector and also the backward detector simultaneously.

D External Multi Photon: In another detectors or the satellite platform, some gamma-rays may be created by the same processes of C, and some photons may hit the forward detector and also the backward detector simultaneously.

E Random Coincidence: Sometimes, the different photons produced by the independent interactions hit the forward detector and also the backward detector accidentally.

F Cosmic-Ray Interaction: When cosmic-ray comes into the satellite, it interacts with material at the different positions, generates some photons simultaneously. Then those

photons hit both the forward and backward detectors.

- Other Process: As the other backgrounds, neutron, electron and atmospheric gamma-rays were measured.

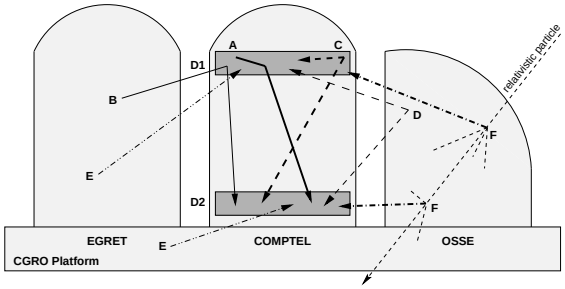

Fig. 4.4.— An illustration of the main channels for the triggering of valid events due to background for COMPTEL [70].

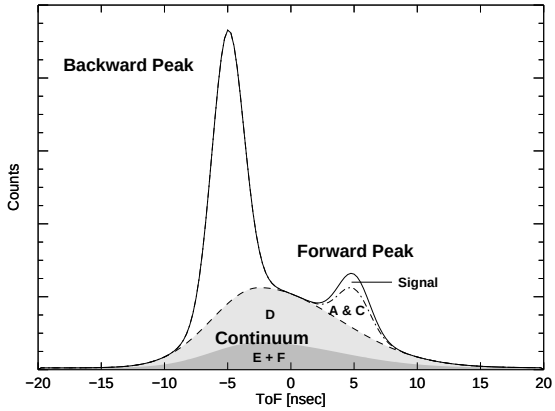

Fig. 4.5.— A schematic representation of the TOF distribution of Compton-like events for COMPTEL [70].

COMPTEL rejected some backgrounds such as neutrons and up-going gamma rays from the part of the satellite using the time of flight (TOF) between the both detectors, although COMPTEL reduced the field of view to obtain the timing information. Figure 4.5 shows the simulated distribution of the TOF [70]. One can see two peaks of 'backward' and 'forward' events in the TOF distribution, in which gamma-ray interacts in the backward detector and then in the forward detector and vice versa. The backward events can be easily rejected applying the TOF window around the forward peak. The D, E and F events, however, make continuum component, and the forward peak includes nearly one third of them. Since the interaction of A and B events are the real Compton interaction, they are the intrinsic background and cannot be rejected. Moreover, if there is a radiative decay in the forward detector, C events have no difference in TOF distribution. Therefore, even if we pick up the forward peak, the most of the selected events still contain background events.

4.2.2 Incomplete imaging of Compton events

Since conventional Compton cameras do not measure the recoil direction of Compton-recoil electrons, one can only reconstruct the incident gamma-ray direction as the event circle. If it can measure that recoil direction and restrict the incident direction event by event, two aspects contribute to the reduction of the background. One is to reject the gamma-ray events

from the outside of the region of interest in the sky. For example, Figure 4.6 shows a sky map describing the position of a GRB with the superposition of the event circles obtained by COMPTEL [71]. One can see the events from not small solid angle, with almost one eighths of the all sky, would become the background confusion source. The other is that using the kinematics one can test if the measured events are likely to be Compton scattering events or improper events such as chance coincidences, neutron scattering events, and the events where Compton scattering occur in the absorber and the scattered gamma ray is absorbed in the scatterer. Those tertiary improper events much increase if one chose heavy material as the scatterer giving priority to the scattering efficiency. One should be careful of these defects from the incomplete imaging ability of classical Compton cameras.

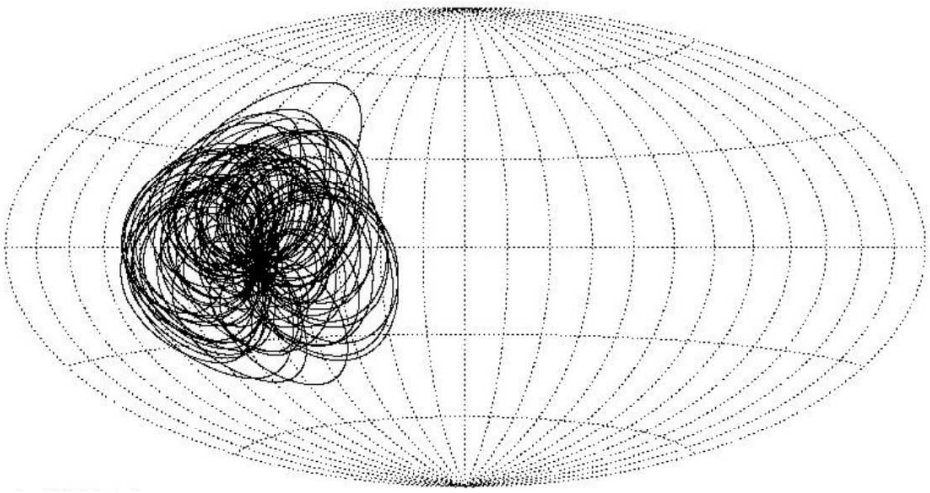

Fig. 4.6.— Event circles image of GRB 910505 obtained by COMPTEL [71]

4.2.3 Suggestion derived from *CGRO*/COMPTEL

For the increase of the sensitivity on the MeV band, Schönfelder pointed out that it is the most sensitive to reduce this instrumental background rate, and showed 7 of different possibilities [7]:

(1) Angular resolution: It is most effective for the detection of point sources to minimize the angular resolution elements and have the best angular resolution.

(2) Sequence determination tools: It is essential to make use of parameters such as the TOF or the motion of Compton-recoil electron, to determine the sequence of interactions and reject the background events.

(3) Localizing arrival direction: Electron tracking constrains the incident direction of the gamma rays.

(4) Low mass equipment: To minimize the production of secondary gamma rays, the mass of passive material around the detector should be as low as possible.

(5) Low background orbit: That is also effective to reduce the secondary gamma rays.

(6) Selection of scattering angle and direction: The events with large scattering angles outside of the field of view become background, and therefore it is essential to constrain the scattering angle to reject such events.

(7) Minimum coincidence window: It is crucial to reduce random coincidence events.

It is remarkable that the greater part of this point out is mentioned about the background reduction (2, 4, 5, 6, 7) rather than the simple improvement of the angular resolutions. This angular resolution is only one angular resolution for the scattering angle of the gamma-ray. In fact, as we point out at Section 4.3.3, it is not effective for the improvement of the sensitivity to have a better angular resolution of the only scattering angle. Also, the applying of (6) narrows the field of view to reduce the efficiency of the observation. For promising observations, a next-generation Compton telescope must have background reduction capability. It is not until the two incident angles are determined photon by photon that the detector can define the point spread function properly and realize a better sensitivity based on optics.

4.3 MeV imaging in astrophysics in post COMPTEL era

4.3.1 Advanced Compton camera

After *CGRO*/COMPTEL era, there are no Compton telescope in orbit. Still, there have been carried out several balloon-borne experiments with an advanced Compton camera planned to open up a new window in the MeV band. Each experiment has a different strategy to attain a high sensitivity. The major concepts for the new generation Compton cameras were dedicated to a good energy resolution of the ARM, a large effective area using heavy material as the scattering material, and a large field of view. However, the gaining of the effective area using heavy scattering material mismatches the lessons proposed by Schönfelder.

Liquid Xenon Gamma-Ray Imaging Telescope (LXeGRIT)

The Liquid Xenon Gamma-Ray Imaging Telescope (LXeGRIT) is a balloon-borne Compton telescope that consists of a liquid xenon time projection chamber as a scatterer and an absorber as shown in Fig. 4.7. It covers an energy range between 0.15 MeV and 10 MeV, has a field of view of 1 sr, an active volume of 20 cm × 20 cm × 7 cm, a detection efficiency close to 20% at 1 MeV corresponding a large effective area of ~ 20 cm^2, which has an ability of the high energy electron tracking, and an angular resolution of $\sim 4^o$ at 1.8 MeV (1σ) [72, 73, 74]. LXeGRIT was launched in 1999 [75] and 2000 [76], and a total of 36 hours of data were taken at an altitude of 39 km. During the flight, the Crab nebula was within the field of view, and it was being analyzed to verify the imaging performance of LXeGRIT, with which the significance of the 10σ level was expected. However, the report of the Crab detection has yet to be reported so far.

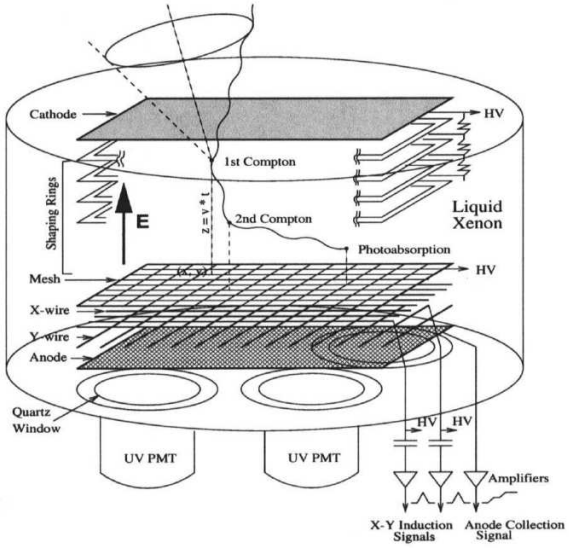

Fig. 4.7.— Schematics of LXeGRIT [77]

Nuclear Compton Telescope (NCT), (COSI)

The Nuclear Compton Telescope (NCT) [78] is a balloon-borne Compton telescope in the MeV band between 200 keV and 20 MeV. It consists of ten high-purity germanium crossed-strip detectors that work as the both scatterer and absorber, and thus a high sensitivity is basically accomplished by the improvement of the angular resolution. Each detector measures $8 \times 8 \times 1.5$ cm^3, and has 37 strips on each side with a pitch of 2 mm to enable the measurement of the 3-dimensional points of the scattering and absorption point, as shown

in Fig. 4.8. The NCT has an active shield made of BGO scintillator, and the field of view is constrained to be 3.2 sr. The balloon-borne experiment was performed from Ft. Sumner, in the U.S., in 2009, and Crab nebula was successfully detected with 4 sigma confidence level by the Maximum Likelihood Expectation Maximization (MLEM) method using 29.3 ks observation data [79] as shown in Fig. 4.9, whereas this signal was not seen with no use of the MLEM. In fact, the MLEM uses a maximum likelihood statistic to simply refine the raw backprojection, and then the point sources become clearer and other features such as background fluctuation are also sharpened. We note that against the detected source signal of 667 events, 2.9×10^5 events of the background remain. NCT aims to be developed for the progressive satellite mission, Advanced Compton Telescope (ACT).

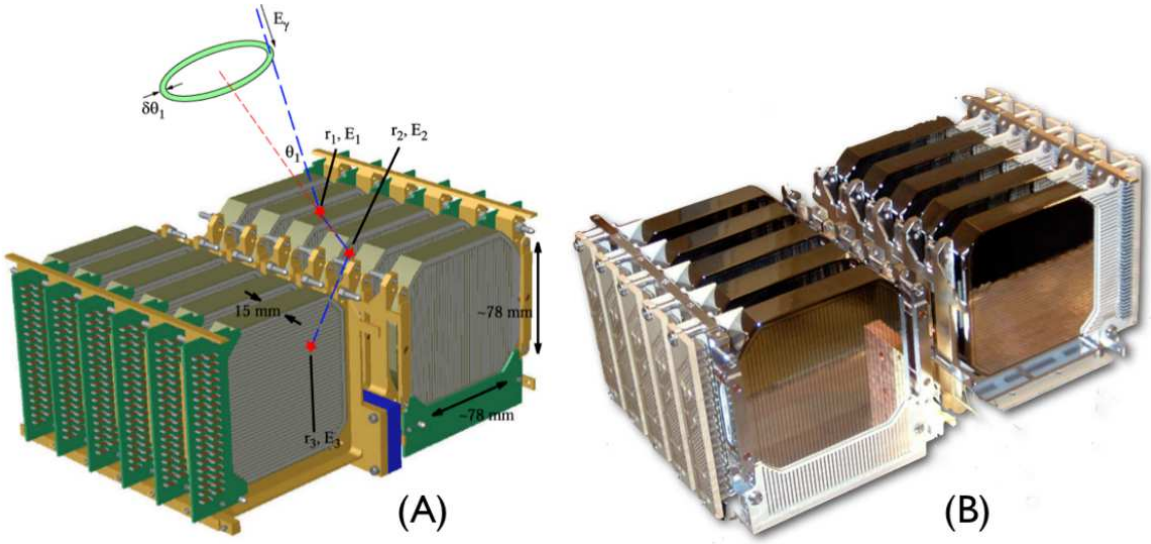

Fig. 4.8.— NCT detector overview. (A) CAD model of germanium detectors. (B) photographs of ten germanium detectors [80].

Hitomi/Soft Gamma-Ray Detector (SGD)

Soft Gamma-Ray Detector (SGD) aboard *Hitomi* was a Compton telescope with a narrow field-of-view of 0.6° (FWHM) active shield where Compton kinematics is utilized to reject backgrounds [81]. The Compton telescope consists silicon and CdTe sensors and the active shield comprises BGO crystal. Internal background can be rejected by checking the inconsistency between the constraint on the incident gamma-ray direction from Compton kinematics and that from the field-of-view of the collimator. SGD performed the Crab nebula observation on Mar. 25, 2016, and the observation data was successfully obtained [82].

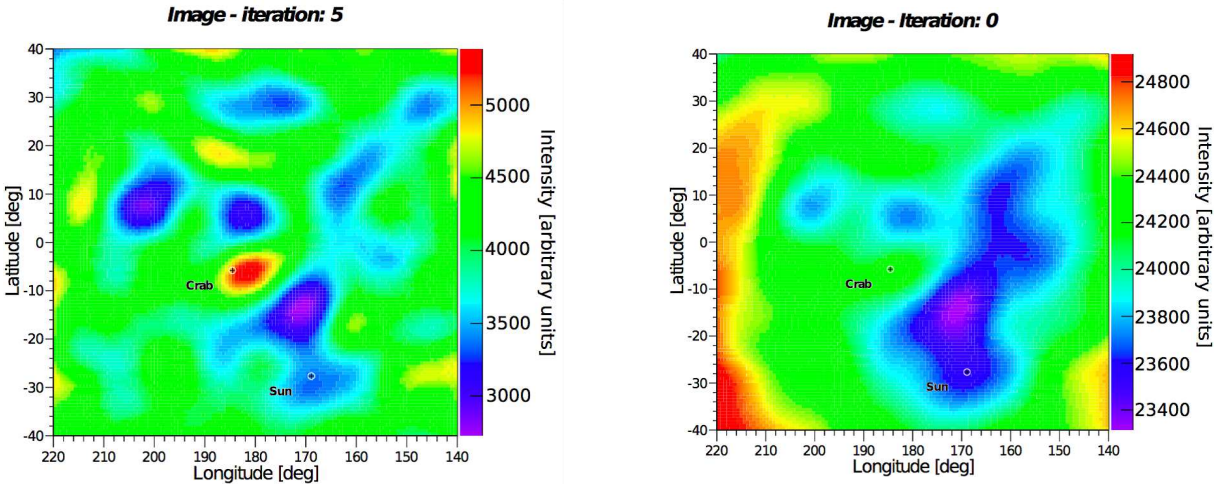

Fig. 4.9.— Crab image obtained by NCT with use of MLEM (left), and with no use of MLEM (right) [79].

4.3.2 Coded aperture imaging

INTEGRAL

International Gamma-Ray Astrophysics Laboratory (*INTEGRAL*) was launched in 2002. It has two gamma-ray detectors: the Imager on-Board the *INTEGRAL* Satellite (IBIS) and the Spectrometer for *INTEGRAL* (SPI). IBIS is a coded aperture imaging system consisting of 95×95 masks of rectangular tungsten tile and 128×128 Cadmium-Telluride tiles (ISGRI- Integral Soft Gamma-Ray Imager) and 64×64 planes of Caesium-Iodide tiles (PICsIT- Pixellated Caesium-Iodide Telescope). The distance between the mask and IBIS detector is 3.2 meters and the spatial resolution, field-of-view, and the energy range of the IBIS is 12 arcminutes, $9° \times 9°$, and 15 keV - 10 MeV, respectively SPI is also a coded mask aperture system with an energy range of 18 keV 8 MeV, a detector area of 500 cm^2, a (fully coded) field-of-view of 14 16 degrees, and an angular resolution of 2.5 degrees (FWHM) [83]. SPI consists of an array of 19 hexagonal high purity germanium detectors optimized for the high energy resolution of 2.5 keV FWHM at 1 MeV, and weighs 1300 kg. The mask is made of 3 centimeter thick tungsten. The detectors are shielded by BGO crystal as a veto counter to reduce the background.

Swift/**BAT**

Swift was a NASA mission dedicated to exploring the gamma-ray bursts, with three instruments: Burst Alert Telescope (BAT) for imaging and localizing GRBs with a wide

field of view and an energy range in 15 - 150 keV, X-ray Telescope (XRT) that provides more precise positions of GRBs, and Ultraviolet/Optical Telescope (UVOT) to detect the afterglow of GRBs. BAT is a kind of coded aperture imaging systems, consisting of a 5200 cm^2 array of $4 \times 4\,\mathrm{mm}^2$ CdZnTe elements located 1 meter behind a 2.7 m^2 coded mask with $5 \times 5\,\mathrm{mm}^2$ elements. The field of view and point spread function of BAT are 1.4 steradian and 14 arcminutes, respectively [84]. Swift detected GRBs about 1000 events so far, and the BAT sensitivity to 1-sec flux is $\sim 3 \times 10^{-8}\,\mathrm{erg\,cm^{-2}\,s^{-1}}$, or $\sim 0.3\,\mathrm{photons\,cm^{-2}\,s^{-1}}$, as shown in Fig. 4.10 [85, 86].

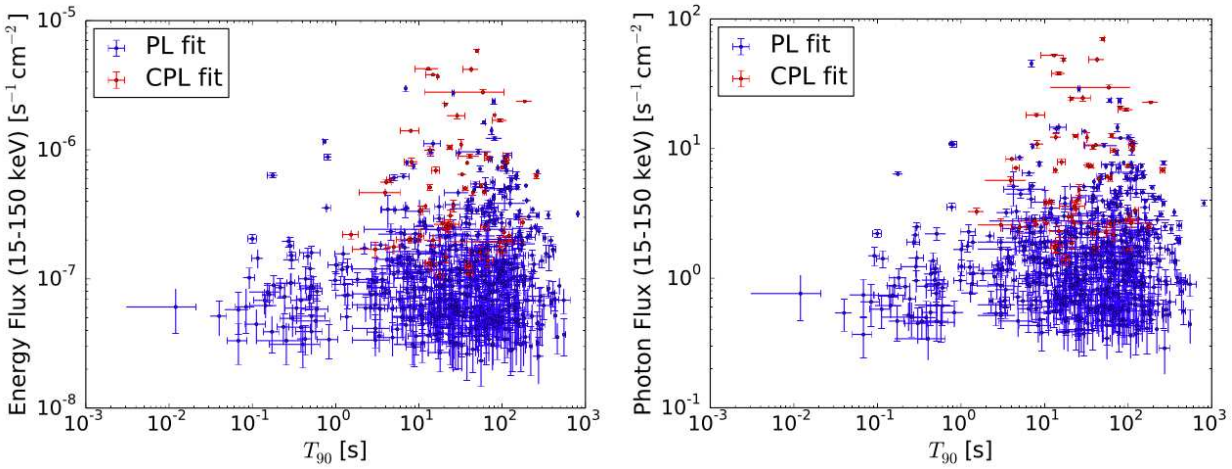

Fig. 4.10.— 1-s peak flux (15 - 150 keV) vs. T_{90} (left) and 1-s peak photon flux (15 - 150 keV) vs. T_{90} obtained by *Swift*/BAT [85]. In the both plots, the fluxes are estimated by the better fit model of the power law or the cut-off power law models.

4.3.3 Electron-tracking Compton camera

An Electron-Tracking Compton Camera (ETCC) reconstructs the both incident direction and energy of the gamma ray by measuring the momenta of the scattering gamma ray and recoil electron. The reconstructed energy E_0 and unit vector of the momentum direction $\vec{s}_{\mathrm{rcs}}$ are expressed as

$$E_0 = E_\gamma + K_e, \tag{4.1}$$

$$\vec{s}_{\mathrm{rcs}} = \left(\cos\phi - \frac{\sin\phi}{\tan\alpha}\right)\vec{g} + \frac{\sin\phi}{\sin\alpha}\vec{e} \tag{4.2}$$

$$= \frac{E_\gamma}{E_\gamma + K_e}\vec{g} + \frac{\sqrt{K_e(K_e + 2m_e c^2)}}{E_\gamma + K_e}\vec{e}, \tag{4.3}$$

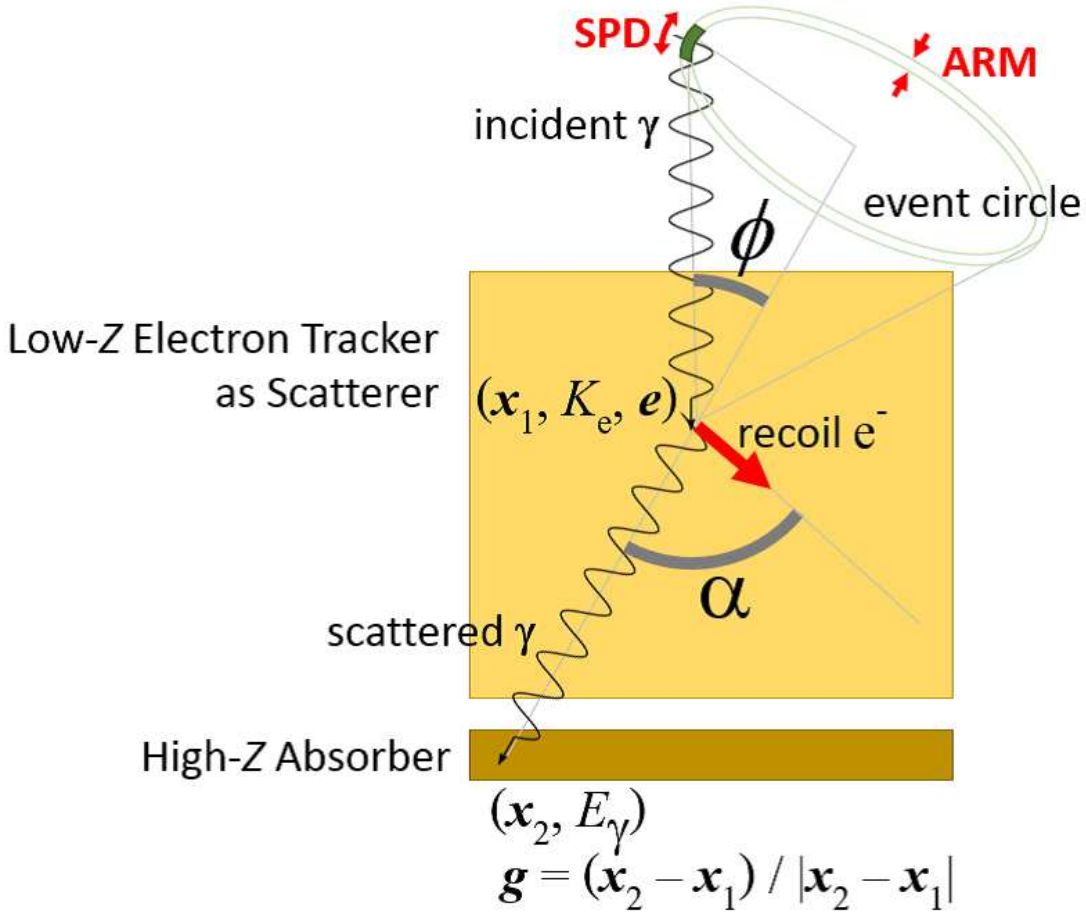

Fig. 4.11.— Schematic of an Electron-Tracking Compton Camera. It consists of an electron tracker as the scatterer made of low-Z material and an absorber made of high-Z material. The scatterer measures the scattering position $\vec{x}_1$, and the kinematic energy and momentum unit vector of the recoil electron, $\vec{e}$ and K_e, respectively. The absorber measures the absorption position $\vec{x}_2$ and energy of the scattered gamma ray E_γ, as well as classical Compton cameras. The momentum unit vector of the scattered gamma ray is obtained by calculating $(\vec{x}_2 - \vec{x}_1)/|\vec{x}_2 - \vec{x}_1|$.

where E_γ and K_e, and $\vec{g}$ and $\vec{e}$ are the kinetic energies and unit vectors of momentum directions of the scattering gamma ray and the Compton-recoil electron, respectively, ϕ is the scattering angle of the gamma ray, and α is the angle between the $\vec{g}$ and $\vec{e}$ as shown in Fig. 4.11. The uncertainty of the reconstructed direction has a shape of the arc and parametrized by the two elements of the angular resolution. One is the uncertainty of the scattering angle ϕ, referred as the angular resolution measure (ARM), and the other is of the scattering plane of the gamma ray, referred as the scattering plane deviation (SPD) as shown in Fig. 4.11. The definitions of ARM and SPD lead the concerning residuals. The errors of the reconstructed direction concerning the ARM and SPD, $\Delta\phi_{\rm ARM}$ and $\Delta\phi_{\rm SPD}$ are derived by

$$\Delta\phi_{\rm ARM} = \arccos\left(\vec{s}\cdot\vec{g}\right) - \arccos\left(1 - \frac{m_e c^2}{E_\gamma + K_e}\frac{K_e}{E_\gamma}\right), \tag{4.4}$$

$$\Delta\nu_{\rm SPD} = \mathrm{sign}\left(\vec{g}\cdot\left(\frac{\vec{s}\times\vec{g}}{|\vec{s}\times\vec{g}|}\times\frac{\vec{s}_{\rm rcs}\times\vec{g}}{|\vec{s}_{\rm rcs}\times\vec{g}|}\right)\right)\arccos\left(\frac{\vec{s}\times\vec{g}}{|\vec{s}\times\vec{g}|}\cdot\frac{\vec{s}_{\rm rcs}\times\vec{g}}{|\vec{s}_{\rm rcs}\times\vec{g}|}\right) \tag{4.5}$$

where $\vec{s}$ and $\vec{s}_{\rm rcs}$ are the true and reconstructed unit vectors of the incident gamma ray.

Compton kinematics leads the relation between ϕ, α, and the recoil angle ψ and measured E_γ and K_e:

$$\cos\phi = 1 - \frac{m_e c^2}{E_\gamma + K_e}\frac{K_e}{E_\gamma}, \tag{4.6}$$

$$\cos\alpha_{\rm kin} = \left(1 - \frac{m_e c^2}{E_\gamma}\right)\sqrt{\frac{K_e}{K_e + 2m_e c^2}}, \tag{4.7}$$

$$\cos\psi = \left(1 + \frac{m_e c^2}{E_\gamma + K_e}\right)\sqrt{\frac{K_e}{K_e + 2m_e c^2}}, \tag{4.8}$$

where the denotation $\alpha_{\rm kin}$ means the angle is estimated by kinematical information. On the other hand, α can be measured geometrically by definition,

$$\cos\alpha_{\rm geo} = \vec{g}\cdot\vec{e}. \tag{4.9}$$

$\alpha_{\rm geo}$ and $\alpha_{\rm kin}$ are independently measured, and therefore we can choose the Compton-like events by applying the condition

$$|\alpha_{\rm kin} - \alpha_{\rm geo}| < \delta\alpha, \tag{4.10}$$

where $\delta\alpha$ is the permissive angle error between the two angles. If the event is triggered by random coincidence, the estimate of α by Eq. 4.7 has no means and thus Eq. 4.10 is generally not satisfied.

In realistic case, the electron before recoil process is not free but bound to a nucleus and therefore modifications in cross section and scattering angle distribution are needed.

Moreover, the energy of the scattering gamma ray with a certain incident energy and scattering angle has not the single value but a broadened distribution according to a distribution of momentum of the bound electron. This effect is called as Doppler broadening effect. Since scattering angle is calculated by measured energy of the scattering gamma ray, the Doppler broadening effect determines the measurement limit of the ARM. Figure 4.12 shows how Doppler broadening affects to the ARM distribution in terms of the energy level of the bound electron. Electrons in outer shell has lower binding energy and thus the broadening of the ARM distribution is limited. The ARM dependence on the atomic number of the scattering target is shown in Fig. 4.13. It has a trend that the targets with larger atomic number have broader ARM distributions. the average FWHM of ARM distribution decreases as the incident gamma-ray energy increases because the electron momentum less contributes to Compton kinematics as shown in Fig. 4.14.

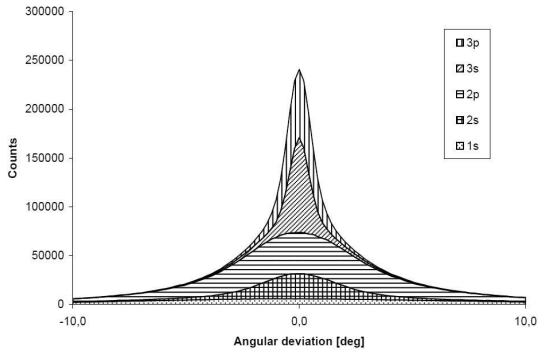

Fig. 4.12.— ARM distribution dependence on the bound state of the electron (E_0 = 200keV, Si) [87]

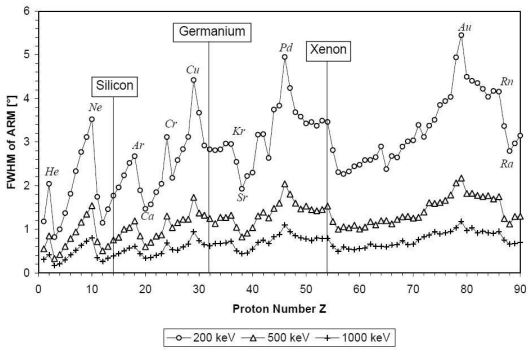

Fig. 4.13.— Dependence of the ARM FWHM on the atomic number of the scattering matter [87]

What determines the lower limit of the broadening of the SPD? the broadening of the SPD distribution results from the uncertainty of the measured momentum directions $\vec{g}$ and $\vec{e}$. The accuracy of $\vec{g}$ is determined by the position resolutions of the both scatterer and absorber and the distance between the scattering and absorption points. On the other hand, the uncertainty of $\vec{e}$ is determined by the ratio of the electron-tracking resolution to the scale of the multiple scattering effect in the scatterer. In ordinary case, as classical Compton cameras couldn't catch the electron track, the lower limit of the broadening of the SPD is determined by the process of the multiple scattering of the recoil electron. The deviation of the scatter angle by the multiple scattering process is well explained by Molière's theory. it has a gaussian distribution with the small scatter angle and the deviation of the angle on the projected plane where the electrons travel a distance of x is approximated by

$$\theta_{\mathrm{rms}} = \frac{13.6\,\mathrm{MeV}}{\beta cp}\sqrt{\frac{x}{X_0}}\left[1 + 0.088\ln\left(\frac{x}{X_0}\right)\right], \tag{4.11}$$

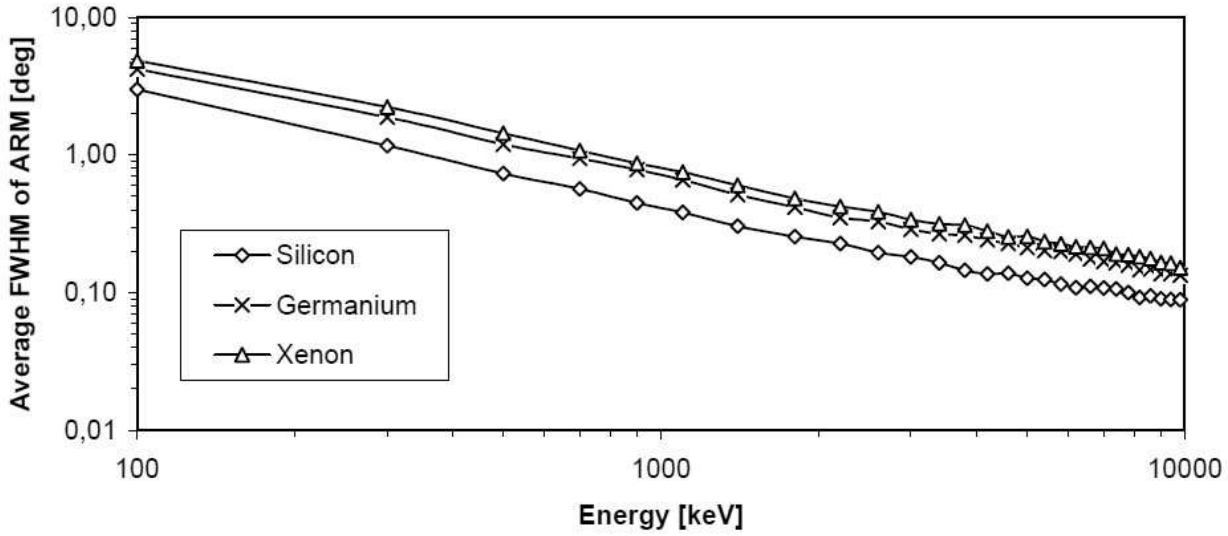

Fig. 4.14.— ARM FWHM dependence on the incident gamma-ray energy [87]

where βc and p is the velocity and the momentum of the electron, and X_0 is the radiation length of the material [88]. Figures 4.15 and 4.16 show the scatter angle calculated by Eq. 4.11 in the scattering material Ar, Xe, and Si. Let us suppose to use the silicon strip detector with a pitch of a few hundreds of micrometers to measure the trajectory of the recoil electron. At least the two trajectory points are required to calculate the momentum direction, and then path length becomes several hundreds of microns. In such case, the scatter angle deviation is about 60 degrees even if the kinetic energy of the electron is 500 keV. On the other hand, a gaseous tracker filled with argon gas of 1 atm makes the the deviation of the scatter angle about 15 degrees with a trajectory length of 1 mm and an electron kinetic energy of 50 keV. In terms of the tracking ability with small multiple scattering, the gaseous tracker has a potent advantage against the silicon strip detectors.

Like other optical, NIR, and X-ray telescopes, the point spread function (PSF) of the Compton camera can be defined to contain a half of the gamma rays emitted from the point source within the angular radius θ. Obviously, the PSF of the Compton cameras must be evaluated based on the two angular resolution parameters, ARM and SPD, ideally. The cumulative ratio in the PSF for gamma rays from a point source as a function of its angular radius for various angular resolutions of the Compton cameras calculated by a Monte Carlo simulation is shown in Fig. 4.17 [90]. We note that the PSF is predominantly dependent on the worse one of the ARM and SPD, which suggests that the sensitivity of classical Compton cameras cannot be simply determined by the ARM by calculation. Let us estimate the sensitivity of the gamma-ray telescope, by considering the statistical variation in the measured counts that consists of the events from the possible unknown source and

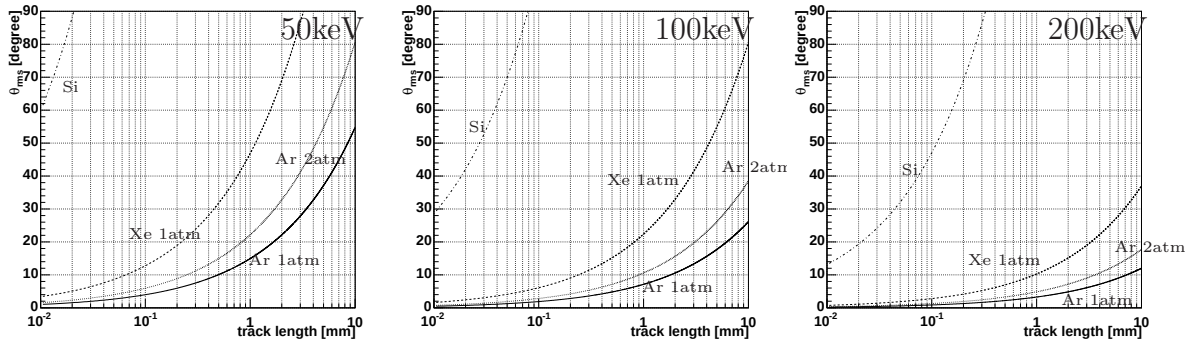

Fig. 4.15.— scatter angle deviation with different kinetic energies of the electron (left: 50keV, middle: 100keV, right: 200keV; Temperature: 20°C) [89].

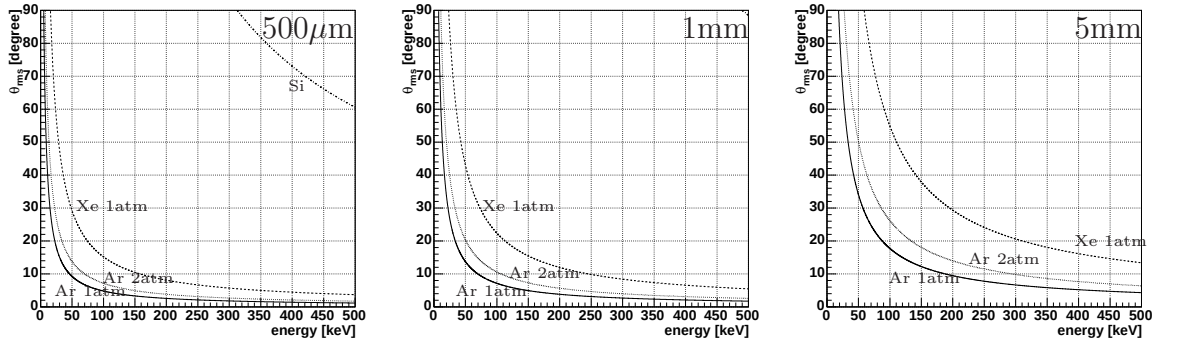

Fig. 4.16.— scatter angle deviation with different ranges of the electron (left: 500μm, middle: 1mm, right: 5mm; temperature: 20°C) [89].

the background. The minimum detectable flux $F_{\rm min}$ yields

$$F_{\rm min} = \frac{n}{\alpha}\sqrt{\frac{\frac{dF_{\rm B}}{dE}\cdot\Delta E\cdot\Delta\Omega}{A_{\rm eff}(E,\Theta,\Phi)\cdot T_{\rm obs}}} \tag{4.12}$$

where n is the number of the standard deviations of the background fluctuations, $\Delta\Omega$ is the solid angle of the circle on the celestial sphere as the source region, which corresponds to the PSF for the point source, α is the fraction of the gamma-ray events from the point source to be reconstructed within the source region, $\frac{dF_{\rm B}}{dE}$ is the energy spectrum of the background events, ΔE is the energy resolution of the telescope, $A_{\rm eff}$ is the effective area of the telescope, and $T_{\rm obs}$ is the effective observation time. We cannot simply apply the ARM to the source region in this calculation, and therefore the classical Compton camera cannot have better sensitivity for gamma rays with only improvement of the ARM.

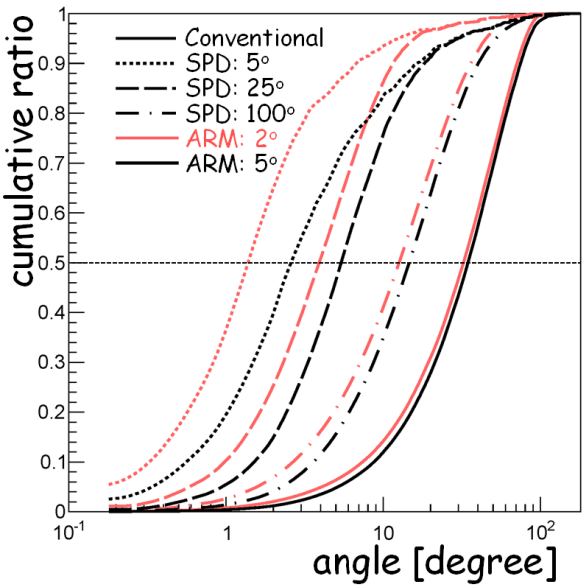

Fig. 4.17.— Point spread function of Compton cameras depending on the angular resolutions of ARM and SPD, described by the cumulative ratio for gamma rays from a point source as a function of its angular radius [90].

SMILE-I/Electron-Tracking Compton Camera (ETCC)

SMILE, an acronym of Sub-MeV gamma-ray Imaging Loaded-on balloon Experiment, is a series of balloon-borne observatories of celestial sub-MeV gamma rays based on an Electron-Tracking Compton Camera (ETCC). The ETCC consists of a gaseous time projection chamber (TPC) based on a micro pattern gas detector as a scatterer to measure the

energy and 3-dimensional track of the Compton-recoil electron and a scintillation camera as an absorber to measure the energy and absorption point of the scattering gamma ray. Using the kinematics, we can determine the energy and direction of the incident gamma rays as the point in the sky event by event.

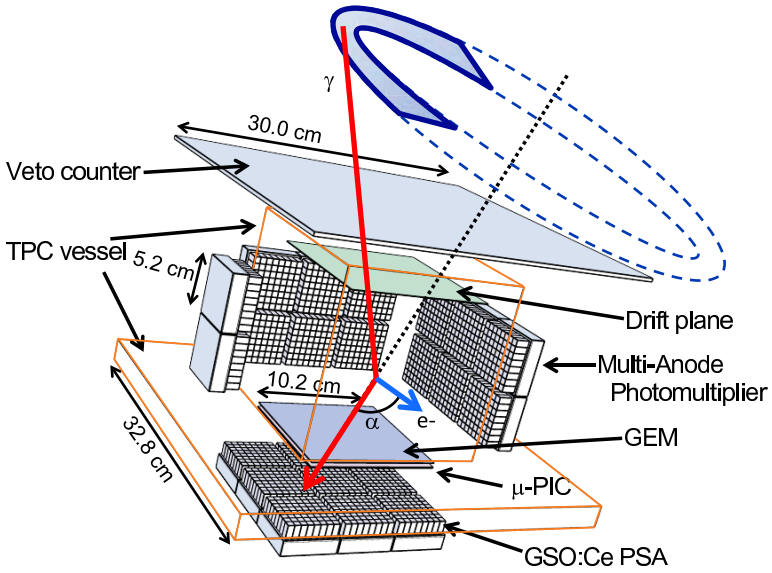

Fig. 4.18.— Schematic view of SMILE-I/ETCC [91].

The first balloon experiment, SMILE-I, was launched from Sanriku Balloon Center, Japan, located at 39°.16 N, 141°.82 E on September 1, 2006 (JST). The main purpose of SMILE-I was to demonstrate the gamma-ray detection capability due the background rejection methods at high altitudes, where the particle identification by the energy loss rate in the TPC was used for it as shown in Fig. 4.21 [91]. The SMILE-I/ETCC consists the gaseous tracker with Xe-based gas of 1 atm to gain the efficiency of Compton scattering, while losing the angular resolution, of which the active volume is $10 \times 10 \times 14\,\mathrm{cm}^3$, and the 2112 pixels of $6 \times 6 \times 13\,\mathrm{mm}^3$ scintillation crystal made of $Gd_2SiO_5 : Ce$, as shown in Fig. 4.18. The detection efficiency and the field of view of the SMILE-I/ETCC are about 10^{-4} and 3 sr, respectively. SMILE-I observed with the level flight at an altitude of 35 km for a real time of 4 hours (3 hours live time) to successfully extract 420 events of the diffuse cosmic and atmospheric gamma rays from huge background events of $\sim 10^5$, which is consistent with the estimation by the Monte Carlo simulation and previous observations performed by other experiments in terms of their flux [91] as shown in Fig. 4.19 and 4.20. Thus, SMILE-I has shown the dramatic ability of noise reduction by the electron tracking and the dE/dx particle identification.

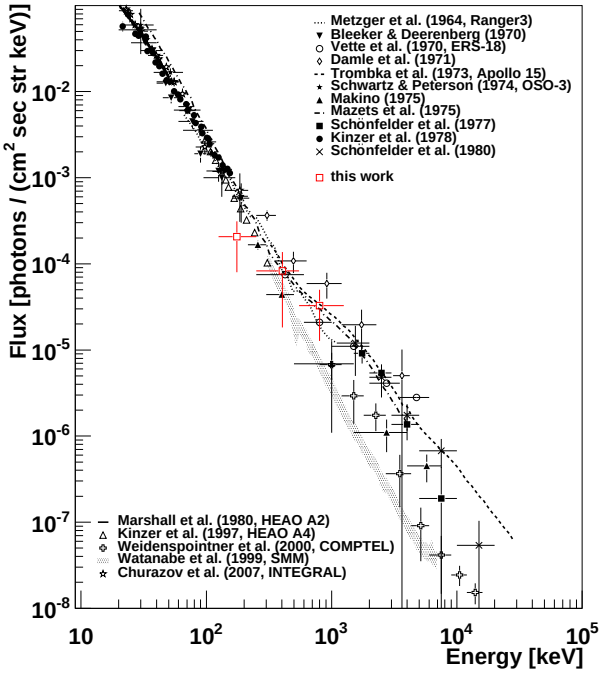

Fig. 4.19.— Spectrum of the cosmic diffuse gamma rays [91].

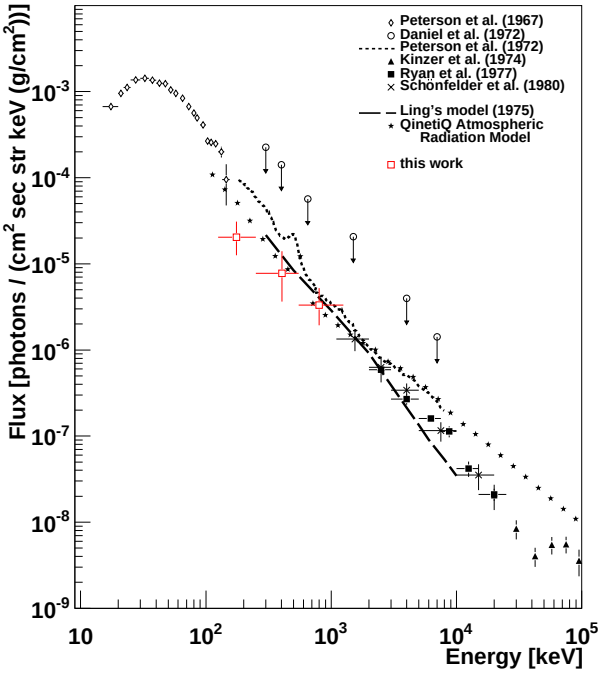

Fig. 4.20.— Spectrum of the atmospheric gamma rays [91].

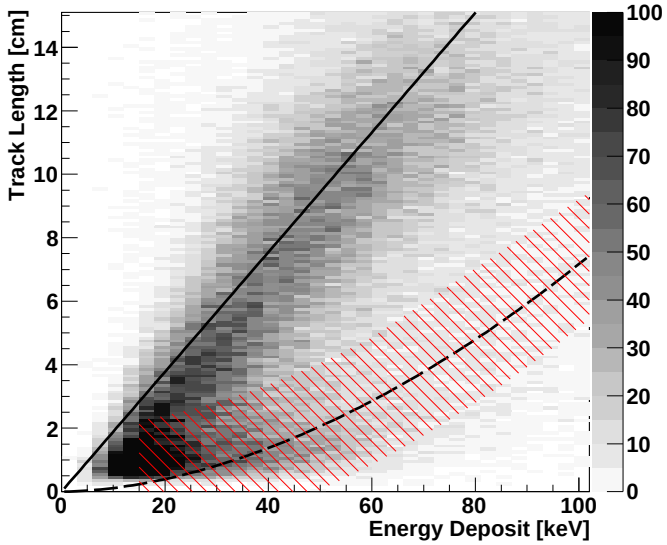

Fig. 4.21.— Energy loss rate in the TPC at the SMILE-I flight. The solid line represents the MIP events, and the dashed line represents the events of the electrons that stopped in the TPC, calculated by Monte Carlo simulation [91].

Chapter 5

SMILE-II Mission

5.1 Mission concept

Though the ETCC on board SMILE-I demonstrated the enough background rejection ability, it had a too small effective area of 0.004 cm^2 for 662 keV to observe celestial objects individually during a short duration flight. The second balloon experiment, SMILE-II, aims to the demonstration of the imaging ability of bright celestial objects such as the Crab nebula and Cyg X-1 at high altitudes.

Let us estimate the required sensitivity with which we can detect the Crab nebula, the 'standard candle' in the high energy astrophysics. We use Eq. 4.12 to calculate such sensitivity. Practically, we suppose the one-day balloon flight in the middle latitude with an altitude of 40 km, and, for example, the observation time for the Crab nebula is about several hours as shown in Figure 5.1. As seen in the SMILE-I flight, the major background events in the balloon flight for the ETCC were the cosmic diffuse and atmospheric gamma rays rather than instrumental gamma rays that are produced by hitting of the cosmic rays to the equipments. Table 5.1 shows the intensities of the cosmic diffuse and atmospheric gamma rays, and the flux of Crab nebula for each energy band. The fluxes of the cosmic diffuse gamma rays and the Crab nebula are attenuated by passing through the atmosphere. Here, as the atmospheric gamma-ray intensity, the model introduced by Ling is used and extrapolated down to 100 keV [92]. The intensity of the extragalactic diffuse gamma rays were measured by HEAO 1 [93] and modeled with the power law below 400 keV,

$$I_{\mathrm{diffuse}}(E) = 2.62 \times 10^{-3} (E/100\,\mathrm{keV})^{-2.75}. \tag{5.1}$$

Here we assumed this power law to be extrapolated up to 1 MeV. Table 5.1 shows the transparency of the atmosphere for gamma rays at an altitude of 40 km η, the flux of the Crab

nebula $F_{\rm Crab}$, the intensity of the diffuse cosmic gamma rays $I_{\rm diffuse}$, and atmospheric gamma rays $I_{\rm atmos}$, as a function of a certain energy range. We note that the photons that come from Crab nebula and the diffuse cosmic background are attenuated by the atmosphere. We calculate the source flux $F_{\rm min} = \int dE\, \eta F_{\rm Crab} = 2.1 \times 10^{-2}\,{\rm cm^{-1}s^{-1}}$ and background $\frac{dF_{\rm B}}{dE}\Delta E = \int dE(\eta I_{\rm diffuse} + I_{\rm atmos}) = 2.6 \times 10^{-1}\,{\rm cm^{-1}s^{-1}sr^{-1}}$. For the source region within the circle on the celestial sphere with a radius of the PSF of the ETCC, $\alpha = 0.5$ is used. In order to detect the Crab at the 5σ level, with $n = 5$, $T_{\rm obs} = 3$ hours, and $\Delta\Omega = 2\pi(1 - \cos(10^\circ))$ sr, the required effective area $A_{\rm eff}$ is estimated to be $\sim 0.5\,{\rm cm^2}$ under the condition of the PSF of 10 degrees. Considering that most of the events are in the lower energy band, a large effective area is critical for lower energy band. Thus we set the requirement for the effective area to be $0.5\,{\rm cm^2}$ for $150 - 300$ keV, and for the PSF of the ETCC to be 10 degrees.

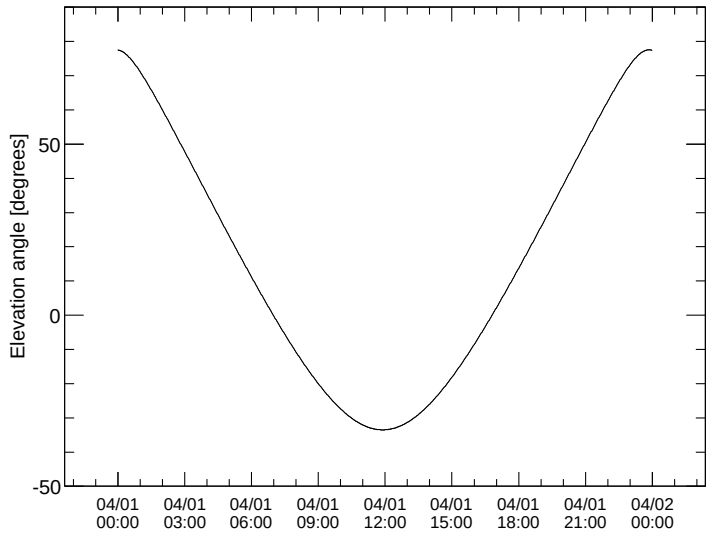

Fig. 5.1.— Elevation angle of Crab nebula at Fort Sumner on Apr. 1, 2018. The time is shown in the UTC time.

The required effective area has to be ~ 50 times larger than that in SMILE-I. To compensate the gap of the effective area, we considered two key improvement factors: the size of the active volume of the scatterer and the efficiency of the electron tracking, with which the effective area is enlarged by $10\times$ and $10\times$, respectively. First, the active volume of the scatterer must be enlarged. At SMILE-I, Xe-based gas mixture was used for the scatterer in order to increase the Compton scattering probability. However, the Xe gas has a large atomic number and therefore the multiple scattering effect makes worse the determination accuracy of the Compton recoil electron momenta, which is unsuitable for the improvement of the sensitivity. Instead, the SMILE-II uses the Ar-based gas with an active volume of

Table 5.1— Photon flux of Crab nebula and intensities of cosmic diffuse and atmospheric gamma rays

E_g [a]	η [b]	$F_{\rm Crab}$ [c]	$\eta F_{\rm Crab}$ [d]	$I_{\rm diffuse}$ [e]	$\eta I_{\rm diffse}$ [f]	$I_{\rm atmos}$ [g]
$150-200$	0.64	1.0×10^{-2}	6.5×10^{-3}	3.8×10^{-2}	2.5×10^{-2}	4.9×10^{-2}
$200-300$	0.67	9.3×10^{-3}	6.3×10^{-3}	3.1×10^{-2}	2.1×10^{-2}	5.2×10^{-2}
$300-400$	0.70	4.2×10^{-3}	3.0×10^{-3}	1.3×10^{-2}	9.2×10^{-3}	2.7×10^{-2}
$400-500$	0.73	2.3×10^{-3}	1.7×10^{-3}	6.9×10^{-3}	5.0×10^{-3}	1.7×10^{-2}
$500-600$	0.76	1.5×10^{-3}	1.1×10^{-3}	4.2×10^{-3}	3.1×10^{-3}	1.2×10^{-2}
$600-700$	0.77	9.8×10^{-4}	7.5×10^{-4}	2.8×10^{-3}	2.1×10^{-3}	8.6×10^{-3}
$700-800$	0.79	6.9×10^{-4}	5.4×10^{-4}	2.0×10^{-3}	1.5×10^{-3}	6.6×10^{-3}
$800-900$	0.80	5.1×10^{-4}	4.1×10^{-4}	1.5×10^{-3}	1.2×10^{-3}	5.2×10^{-3}
$900-1000$	0.81	3.9×10^{-4}	3.1×10^{-4}	1.1×10^{-3}	8.9×10^{-4}	4.2×10^{-3}
$150-1000$			2.1×10^{-2}		7.7×10^{-2}	1.8×10^{-1}

[a] Photon energy range (keV).
[b] transparency of the atmosphere at an altitude of 40 km (a residual mass of 2.9 g/cm^2).
[c] photon flux from Crab without attenuation (cm^{-2}s^{-1}) [94].
[d] unit in cm^{-2}s^{-1}.
[c] Cosmic diffuse gamma-ray intensity without attenuation (cm^{-2}s^{-1}sr^{-1}) [93].
[f] unit in cm^{-2}s^{-1}sr^{-1}.
[g] atmospheric gamma-ray intensity (cm^{-2}s^{-1}sr^{-1}) [92].

$30\times30\times30\,\mathrm{cm}^3$, which is enlarged by a factor of 18 (2 for depth and 9 for geometrical area) compared to that of SMILE-I. Figure 5.2 shows the Compton scattering probability for various gas compositions with a depth of 30 cm. For an active volume of $30\times30\times30\,\mathrm{cm}^3$, the Compton scattering probability reaches several square centimeters with 1-atm argon gas. Second, the efficiency of the data acquisition of the electron tracking should be improved. The SMILE-I/ETCC data suggested that only about 10% of the electron tracking data had an enough quality for the estimate of the electron momentum direction, because the rest of the data had too few hit points less than 3. The reason for that problem was found to be the hardware preprocessing of the encoding track data, as explained at Section 5.2. The improvement of the data acquisition of the track data recovers the efficiency by a factor of 10. Finally, the coverage factor of the absorber should be enough high to catch the scattered gamma rays effectively. For the low energy incident gamma rays with 150 - 300 keV, the angular dependence of the cross section of Compton scattering is less influenced by the relativistic effect, and therefore the scatterer should be covered with the absorber so as to catch the scattered gamma rays with a scattering angle of around 90 degrees. Thus, the absorber should be placed at both the sides and the back of the gas tracker. Since we are focusing on the gamma rays with an energy of 150 - 300 keV for SMILE-II, the thickness of the absorber

should be larger or comparable to the radiation length. In this way, the ETCC can obtain an enough effective area of about $1\,\mathrm{cm}^2$, which is estimated by a Monte Carlo simulation developed as Chapter 6.

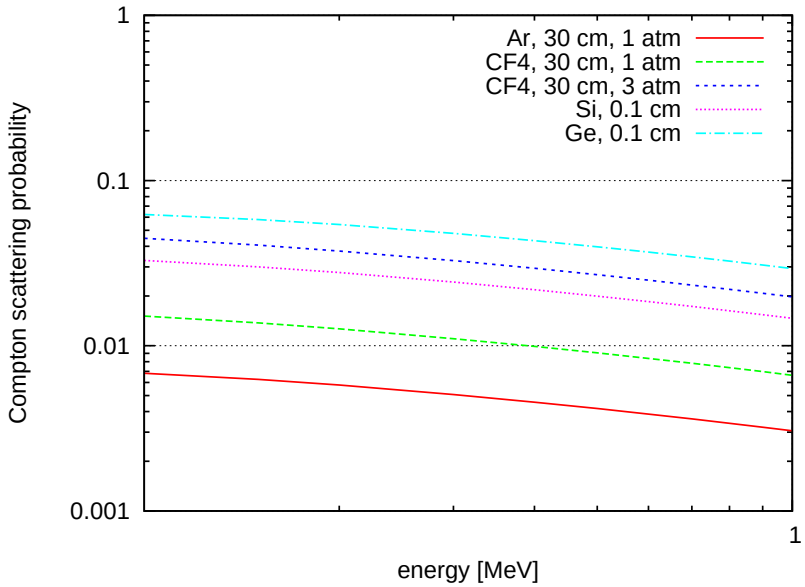

Fig. 5.2.— Compton scattering efficiencies for various materials.

The electronics system of the SMILE-I/ETCC cannot be simply used to the SMILE-II/ETCC due to a couple of defects. First, as mentioned above, the data acquisition of the electron tracking must be upgraded to recover the event efficiency of the electron tracking from about 10% to about 100%. Second, the trigger rate during the SMILE-II flight cannot be tolerated with the SMILE-I data acquisition system in terms of the live time. Figure 5.3 shows the dead time at SMILE-I, indicating that it was about 20% at the horizontal flight with an altitude of 35 km. If the size of GSO crystal is increased by a factor of 3.4, which is supposed at the SMILE-II configuration, the extrapolated dead time would increase to the critical level of $> 50\%$. Thus most of the observation time would be lost for the data acquisition. Therefore the data acquisition system that is tolerant with high-rate trigger is mandatory. Third, the SMILE-I/ETCC used general-purpose electronics such as NIM modules, which were originally developed for ground-based physics experiments, and therefore the large power consumption of the SMILE-I electronics was not well designed for a balloon flight. The total power consumption of the system is required to be below 600 W for the next balloon flight. However, we cannot merely enlarge the system without the reduction of the power consumption because the total power consumption of SMILE-I was about 350 W. Thus, SMILE-II/ETCC electronics should be replaced to the special ones designed for the lower power consumption. Reduction of the weight is also preferable because the heavy equipments become the local background source due to the scattering of the cosmic rays. In this way, most of the electronics of the SMILE-II/ETCC have been newly developed so as to satisfy these requirements.

5.2 Time Projection Chamber (TPC) based on a Micro Pixel Chamber

As the scatterer of the SMILE-II/ETCC, the position resolution of the track is an important factor. In order to achieve a PSF of 10 degrees, the SPD should be better than 100 degrees, as indicated in Fig. 4.17. Then, the position resolution of the gaseous tracker should be better than 1 millimeter, because the scatter angle deviation in argon gas with 1 atm becomes about 10 degrees for 50 - 200 keV as shown in Fig. 4.15. Thus, we adopted a time projection chamber based on a micro pixel chamber (μ-PIC) as the scatterer. The μ-PIC, which is a kind of micro pattern gaseous detectors, is a two-dimensional imaging detector with a fine-pitch electrode manufactured based on the printed circuit board technology [95]. Each pixel of the μ-PIC electrode has a pitch of 400 μm to be placed on a polyimide substrate, and works as a proportional counter as shown in Fig. 5.4. The anode and cathode pixels are connected by copper strips on the backside and topside of the substrate orthogonally, respectively, to form a two-dimensional readout. Considering the standard deviation of the

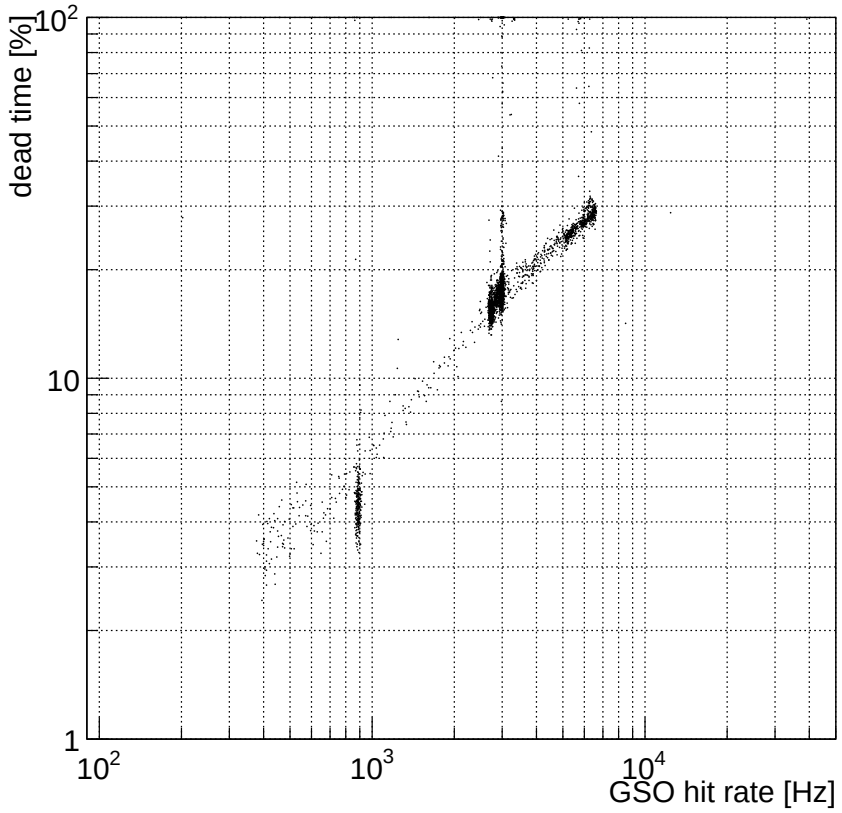

Fig. 5.3.— Trigger rate of GSO crystal versus the dead time ratio at SMILE-I. At the level flight of 35 km, the hit rate was 3 kHz.

uniform distribution, a μ-PIC has a position resolution of $400/\sqrt{12}\mu\mathrm{m} \simeq 120\mu\mathrm{m}$. The μ-PIC in the SMILE-II/ETCC has 768×768 strips, and has an effective area of 30.72×30.72cm. The energy loss of a minimum ionization particle in the argon gas is 2.54 keV/cm at 1 atm, which produces only ~ 3.9 electrons per 400 μm path length. Due to the constraint of the noise level of the electronics of the μ-PIC, the effective gas gain has to be $\sim 2 \times 10^4$ but the μ-PIC itself can obtain only 6000 under the stable operation. Then, we use a Gas Electron Multiplier [96, 97], GEM, to compensate the gas gain gap combining with the μ-PIC in the gaseous tracker of the ETCC. A GEM, originally developed by Sauli *et al.*, has the structure of electrode-insulator-electrode layered foil with many holes as shown in Fig. 5.5. In the operation, we supply different voltage to the two electrodes and the avalanche occurs in the holes at which a strong electric field is present. The GEM used in the flight model has an effective area of 32×32 cm^2 and made of copper electrodes and liquid crystal polymer insulator with a thickness of 100 μm. The diameter of the holes is 70 μm and the hole pitch is 140 μm. The combination of the μ-PIC and the GEM is used as a time projection chamber (TPC), in which the electric drift field is applied to the active volume and the drift time for which the electrons reach to the detector x-/y- plane is used for the determination of the position along to the z-axis, with an active volume of $30 \times 30 \times 30$ cm^3, and it has an advantage of reduction of the ion feedback to the drift electrode less than 1%. The filling gas of the TPC is argon based mixture (Ar 95%, CF_4 3%,iso$-C_4H_{10}$ 2%) of 1 atm, and the gas gains of the μ-PIC and GEM are 2000 and 10, respectively. To increase the cross section of the Compton scattering, the replacement of the filling gas to Xe- or CF_4- based gas is one of the solutions, but requires the operation of the higher voltage between the electrodes.

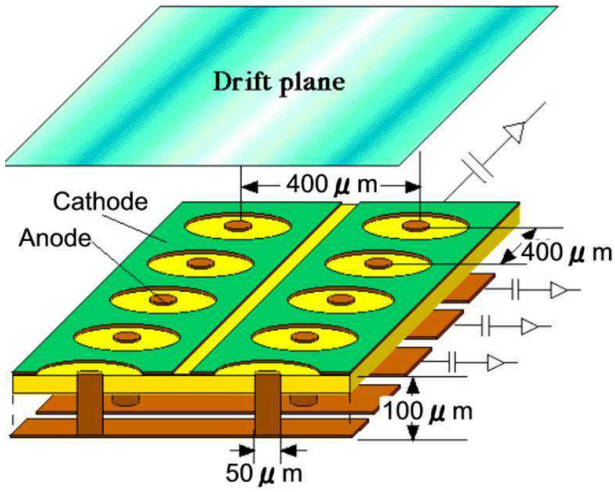

Fig. 5.4.— Schematics of μ-PIC [89].

As pointed out before, the lower power consumption of the electronics is one of the

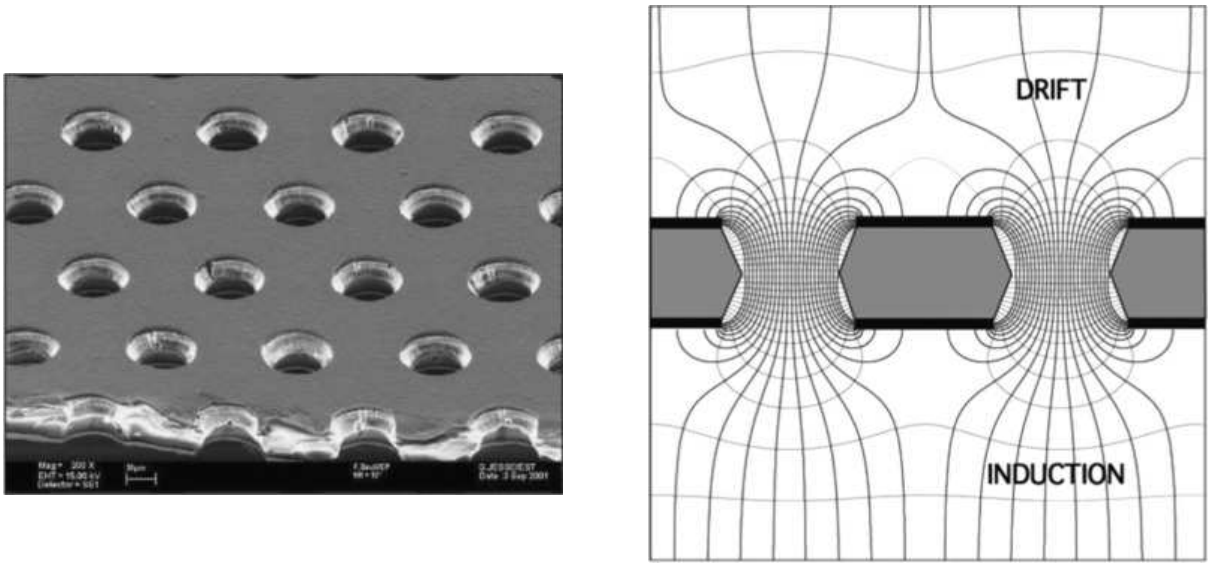

Fig. 5.5.— (Left) A photo of s typical GEM electrode [98]. (Right) An electric field in the region of the holes of a GEM electrode [98].

requirements in the SMILE-II mission. For the the front-end readout electronics of the μ-PIC in the SMILE-I mission, the amplifier-shaper-discriminator (ASD) integrated circuits, were used, which had been developed for the ATLAS detector in the large hadron collider [99]. For the digital signal processing, a position-encoding system with 8 field-programmable gate arrays (FPGAs) clocked at 100 MHz was used. The total power consumption for each strip was 130 mW. The requirement for the power consumption of the μ-PIC readout on the SMILE-II/ETCC is to keep it as low as at SMILE-I, while the number of the strips increase by a factor of 3. To attain this required power consumption, we developed a new CMOS application specific integrated circuit (ASIC) chip, FE2009bal for the front-end readout of the μ-PIC [100]. The requirements for the FE2009bal were a power consumption less than 20 mW per channel, which is the half of the total readout power consumption, high integration of 16 ch per chip, a wide input dynamic range in -1 to 1 pC, and a low noise level with an equivalent noise charge of 6000 e^- for the detector with a capacitance of 100 pF. To achieve these requirements, we designed an ASIC chip using the SPICE simulation. The chip was fabricated by the Taiwan Semiconductor Manufacturing Co., Ltd. with a 0.5 μm CMOS process. The primary specifications of the ASIC are shown in Table 5.2. Also, we used an 800 μm pitch readout that involved grouping two adjacent anode and cathode electrodes, which results in reduction of power consumption and cost of the electronics.

Figure 5.6 shows a diagram of the FE2009bal chip. The ASIC has 16 analog inputs (XIN0, ..., XIN15), 16 discriminated digital outputs with 2.5 V CMOS level (XDP0, ..., XDP15), and one 16-channel-summed analog output (XAOUT). It requires $\pm$2.5 V power supply and consumes 18 mW per chip, satisfying the requirements set out for this chip. The

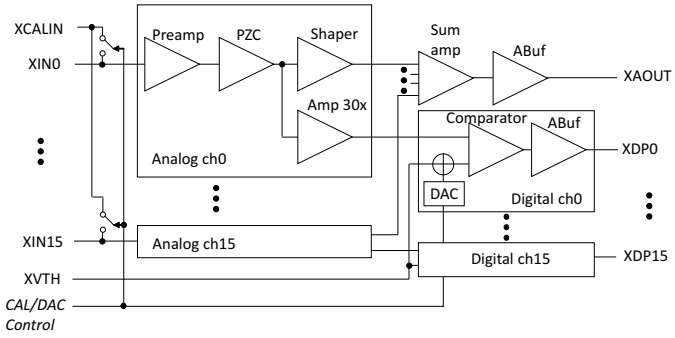

Fig. 5.6.— Schematic view of ASIC 'FE2009bal'.

Table 5.2— Specifications of FE2009bal.

Process	0.5 μm CMOS
Number of input	16 ch
Preamplifier gain	0.6 V/pC
Peaking time	$\sim$ 30 ns
Sum amplifier gain	0.8 V/pC
Dynamic range	-1 to +1 pC
Cross talk	$< 0.5\%$
Time walk	~ 6 ns (10 fC to 1 pC)
ENC at $C_{\rm d} = 100$ pF	$\sim 6000\, e^-$
Power consumption	18 mW per chip

gain of the preamplifier is 0.6 V/pC, and the time constant of the shaping amplifier is 20 ns, and the peaking time is practically 30 ns (See later chapter). Each output of the shaping amplifier is connected to the input of summing amplifier and the digitizing circuit. The summing amplifier scales the input signals down to one sixth of the input, and then sums out to one, of which the total gain of the system through the pre- and summing amplifier is 0.8 V/pC. The digitizing circuit consists of the amplifier that magnifies the signals by a factor of 30 and the comparator. In the comparator, each signal is compared with a common threshold voltage ($V_{\rm th}$), and digitized. Since the input bias voltage of a MOS FET transistor generally varies in each channel, each digitizing circuit has a 6-bit digital-to-analog converter (DAC) to compensate for its baseline voltage. There is another input (XCALIN) for a test of the response of the chip, and one can switch the position number of channels in which the

XCALIN channel is connected to the input of preamplifier.

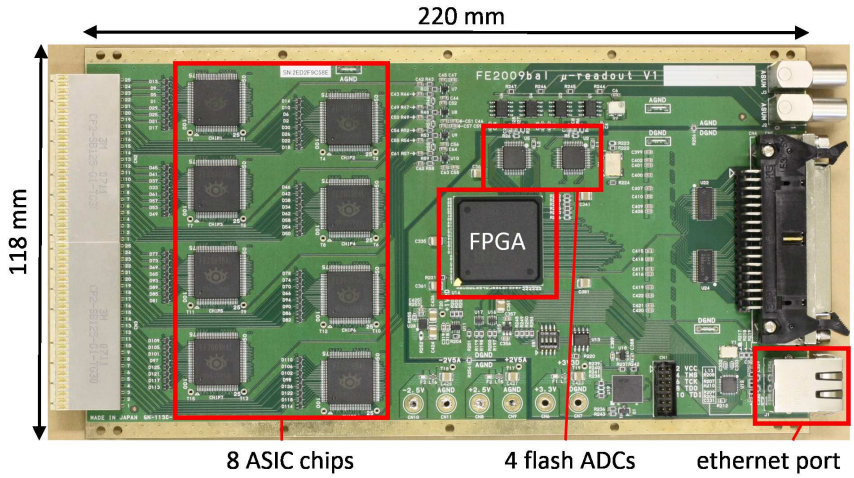

Fig. 5.7.— Picture of μ-PIC readout board [100]. The board size is 118×220 mm^2. It contains 8 CMOS ASIC chips (FE2009bal), an FPGA, 4 Flash ADCs, and an Ethernet port.

Figure 5.7 and Figure 5.8 are a photograph of the readout board [100], and a schematic view of the readout of the μ-PIC signals. The total power consumption of the readout electronics in the TPC is 45 W (30 mW per strip). The readout board contains 8 CMOS ASIC (FE2009bal), 4 flash ADCs, an FPGA, and an Ethernet port. It has 128 analog input channels which are discriminated by the ASICs to be fed to the FPGA with synchronization of 100 MHz (10 ns) clocks. The timing resolution of the hit signals of the TPC limited by the quantization error is therefore determined to be $(10/\sqrt{12}) \approx 3$ ns RMS from the central limit theorem. Thus, the position resolution along to the drift direction is about 120 micrometers if the drift velocity of the electrons in the TPC is assumed to be 4 cm/μs. The two of 16-summed analog signals from each chip pair are summed and fed to 10-bit, 50 MHz flash ADC, and then digitized summed signals are sent to the FPGA. These ADCs continuously digitize the waveforms of the summed signals, and in the FPGA, the 10-bit 50 MHz waveform data are converted into 8-bit 25 MHz for the data reduction [101]. The FPGA saves the 128-bit synchronized hit pattern and 4-ch digitized waveforms in the ring buffers. For the determination of the threshold for the hit pattern and the 6-bit DACs for the baselines in the ASICs, the SiTCP core [102] for the TCP/UDP protocol via the Ethernet is installed in the FPGA. These parameters to be set are stored in the main on the VME bus and downloaded via Ethernet to the all chips on the readout boards at every startup process.

Figure 5.9 shows a timing chart of the data acquisition of the TPC. The TPC readout board has several I/Os for data acquisition: three inputs (trigger, transfer, and clear) and three outputs (process, data-exist, and transfer end). In the idle (ready) status, the FPGA

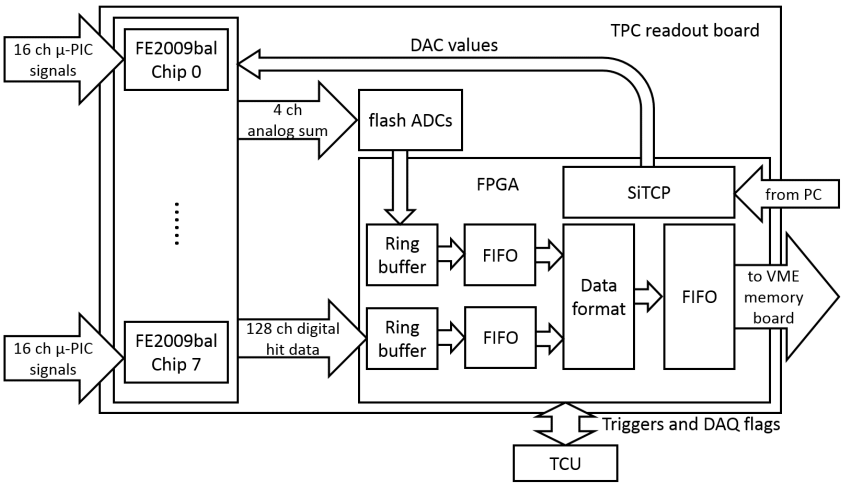

Fig. 5.8.— Block diagram of μ-PIC readout board [100].

saves the latest hit and waveform data continuously in the ring buffer, as mentioned above. Once a 'trigger' signal is set to the FPGA, it stops writing the hit data in the ring buffers and starts transferring the formatted latest data saved over 10 μs to latter first-in first-out (FIFO) buffers. This time duration is determined so as to measure the whole electron track within an active volume of the TPC, considering that the electron cloud produced near the drift plane reaches to the detector plane in about 6 microseconds. The 'process' signal is an output from the FPGA to the trigger-control-unit (TCU), while the TPC board reads the ring buffers. The TCU is explained later, in the section describing the ETCC data acquisition. If any hit exists in the ring buffer, the FPGA sends the 'data-exist' signal to TCU. In return, at the end of the process, TCU sends the 'transfer' signal to the all TPC readout boards to start data transfer from the FIFO in the FPGA to the VME memory module, which stores data of several thousand triggered events. This is how the DAQ system reduces the dead time due to the latency of the main DAQ system in the VME CPU and data transfer time from the VME memory module to the CPU memory. Upon data transfer from the ring buffers to the FIFO in the FPGA, a trigger identification number (trigger ID) is attached to the top of each event data. On the other hand, when the all readout boards have no hit signals and therefore no 'data-exist' signal inputs to TCU, TCU sends a 'clear' signal to the all readout boards to discard the event. When the FPGA finishes data transfer or receives the 'clear' signal, they are all reset and start recording the hit and waveform data to the ring buffers, again. Since the VME memory module stores the data of several thousand events, the CPU on the VME bus can reduce the number of the access to the memory modules for the storage of the data to the disks, because the CPU interrupt for the access to the VME system requires a longer latency time of the order of milliseconds.

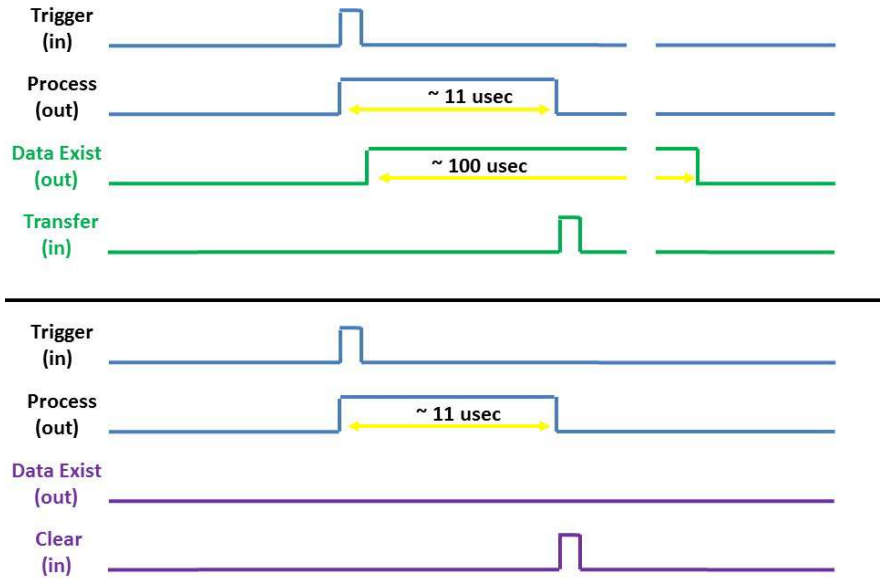

Fig. 5.9.— Timing chart of TPC DAQ system.

In the FPGA logic on the readout board of the TPC, TPC hit data are formatted. Especially, the hardware-coded anode-and-cathode coincident data only were stored in the SMILE-I data acquisition system. When the rising edge of the anode (cathode) hit coincided within 10 ns (100 MHz clock) to that of cathode (anode), the addresses of the both anode and cathode and the clock count were encoded in the FPGA and transfered to the CPU. However, a gate of 10 ns was too restrictive for the coincidence between anode and cathode signals of μ-PIC, mainly due to the slow rise time of the amplifiers (16 ns) and the difference in delay timing in the circuit path of each channel in the FPGA, resulting in considerable loss of hit strips (only a few 10% of hits remains). This loss becomes a serious problem for the ETCC, because low-energy recoil electrons with a kinetic energy of few tens of keV in Compton scattering have only several hit strips in the TPC. In fact, the tracking efficiency of the obtained Compton events in which at least 5 hit points were required, for the previous TPC-readout algorithm, was one order of magnitude less than that calculated from the Compton scattering cross section of the gas in the TPC. In the new algorithm, to recover almost all the hit strips in the TPC, all hit-strip addresses on the both anode and cathode are transfered with hit timing to the memory module without hardware-implemented coincidence in the FPGA. In the off-line analysis, an adequate gate width is applied to anode and cathode hit strips using the hit timing. In addition, as depicted in Figure 5.10 the time between the rise and fall of the hit pulse is recorded as the time-over-threshold (TOT), which is roughly proportional to the pulse height or charge. Figure 5.11 and 5.12 show the distributions of the

number of hits in the TPC, and typical tracks of electrons and minimum ionizing particles, obtained by the new and old data acquisitions, respectively. One can see the number of the hits points has dramatically increased by applying the new track data acquisition. Moreover, the width of the hit points along to the vertical axises for each strip means the TOT. We note that the electron track obtained by the new algorithm provides a indicator of the Bragg peak at the track end point, showing the long TOT, and shows continuously hit points without an order of loss of the hit points. It is found that this new reconstruction method provides a much better efficiency of the detection of the recoil electrons of nearly 100% (See the Chapter 6).

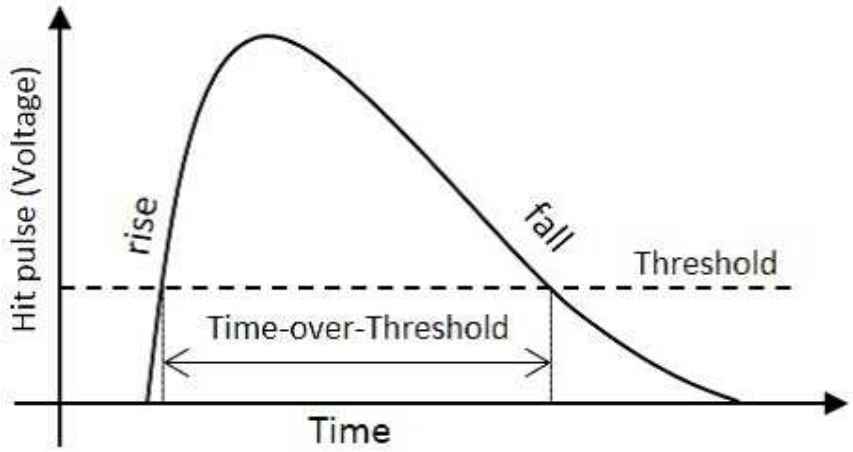

Fig. 5.10.— Schematic view of time-over-threshold (TOT) [100].

Figure 5.13 a spectrum obtained by the TPC based on the μ-PIC and GEM under the irradiation of X-rays from radioactive source ^{109}Cd, and one can clearly see the peak of X-ray fluorescences of Ag Kα (22.2 keV), Pb Lα (10.6 keV), Cu Kα (8.0 keV) and possibly Ar Kα (3.0 keV), indicating that the threshold level of the TPC is about 1 keV. As mentioned above, each TPC readout board has 4 flash ADCs, and for the $30 \times 30\,\mathrm{cm}^2$ μ-PIC, it needs $3+3$ boards in total to read the signals from μ-PIC. Then, each electrode of the anode and cathode can obtain 12 channels of waveforms respectively, and one can divide the entire effective area of the μ-PIC to 12×12 sub-regions and estimate the gain variations due to the position of the electrode by obtaining the cross point of the most energetic waveforms of anode and cathode channels. Figure 5.14 shows the uniformities of gas gain and energy resolution of the TPC as divided to the 144 sub-regions, respectively. In the current operation, the typical gas gain is about 22000 and their non-uniformity is about 9% RMS. On the other hand, the typical energy resolution is 21% at FWHM for 22.2 keV, as shown in Fig. 5.15. One can see the border of the TPC has a trend of lower gas gain and worse energy resolution than those at

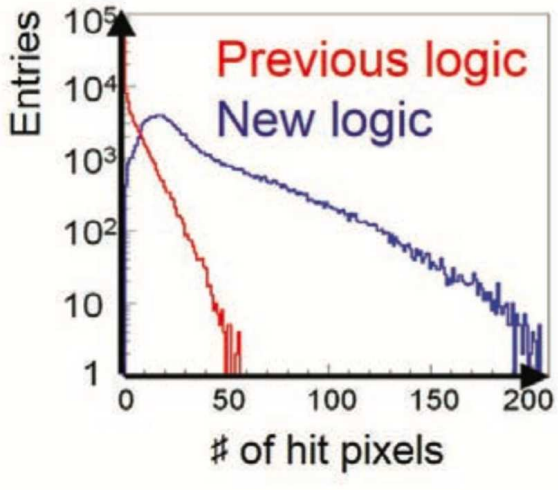

Fig. 5.11.— Distributions of the number of the hits in the TPC, obtained by the old track data acquisition (red) and the new one (blue) [103].

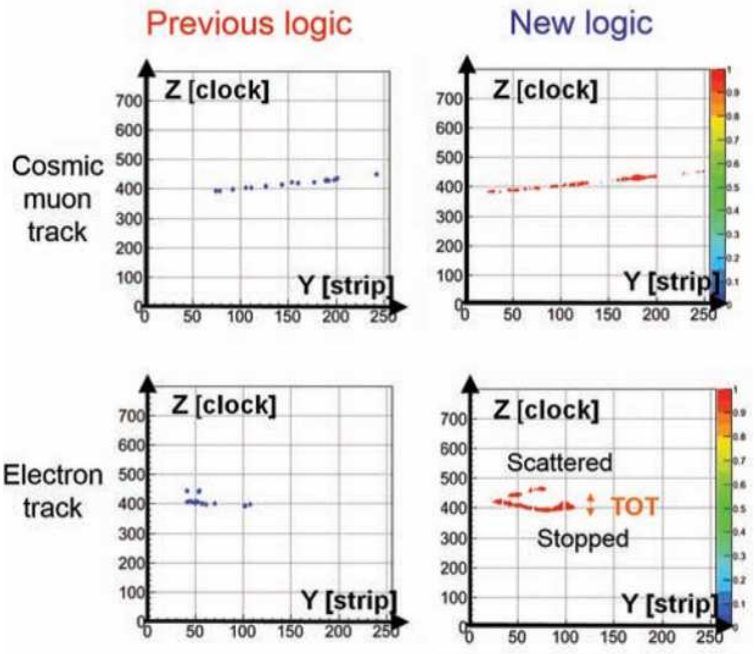

Fig. 5.12.— Examples of TPC 2-d projected track data obtained by the old logic (upper) and the new one (lower). On each strip, one can derive the time-over-threshold by counting the number of the continuously lasting hits, which is a indicator of the energy loss [103].

the center, which suggests the inefficiency of the charge collection due to the distortion of the electric field near the boundary of the μ-PIC. Figure 5.16 shows a clock-count distribution of ^{137}Cs irradiation experiment with the ETCC, which represents the drift time of ionized electrons produced in the TPC. The 'trigger' signal was made by the PSA hit timing with a delay of 8 μs, and the time when the ring buffer stops is at 1023 on the clock time. Since the encoding clock is 100 MHz, the rising-edge timing of the GSO trigger is approximately 220. Therefore, the events distributed within the clock count of 240-710 are coincidence events between TPC and PSAs. The width of the clock distribution for coincidence events gives the maximum drift time in the TPC, and the estimated drift velocity is about 6.6 cm/μs. That velocity is consistent with the simulation by Magboltz [104]. Figure 5.17 shows a correlation between the track range and the energy loss in the TPC derived with the new algorithms. Compared to the old one as shown in Fig. 4.21, the new algorithm provides the better identification of recoil electrons that stop in the TPC from minimum-ionizing particles such as cosmic rays and penetrating high-energy recoil electrons escaping from the TPC. The broken line shows the numerical calculation for fully-contained electrons, which is consistent with the measurement.

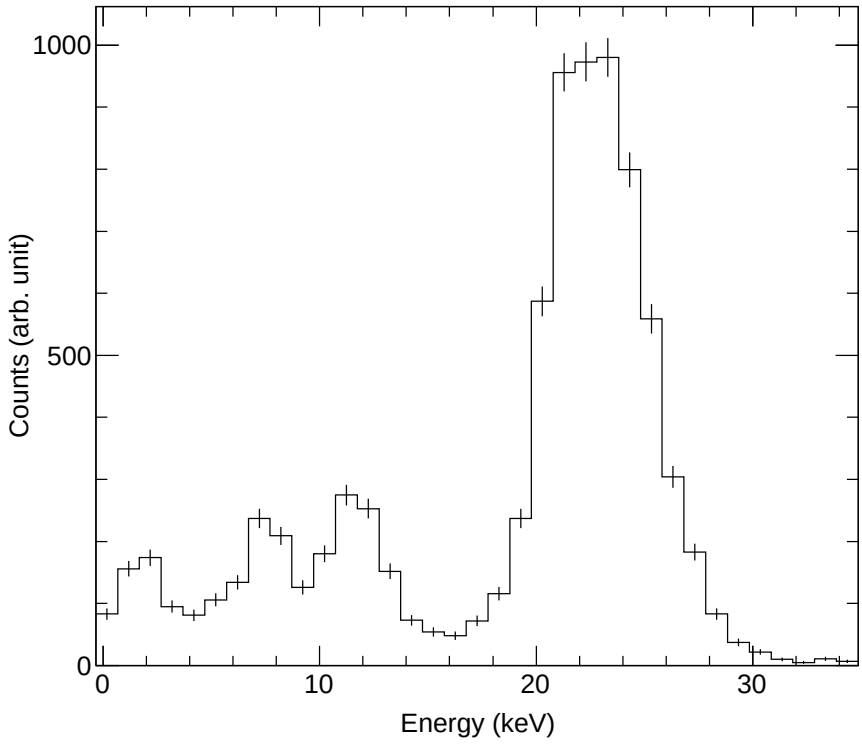

Fig. 5.13.— Spectrum obtained by irradiation of radioactive isotope source of ^{109}Cd. photoelectric peaks can be seen at Ag Kα (22.2 keV) from ^{109}Cd, and Pb Lα (10.6 keV), Cu Kα (8.0 keV) and possibly Ar Kα (3.0 keV) from the materials that are used for the TPC.

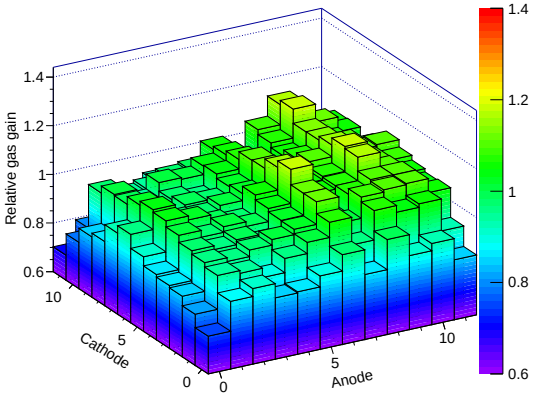

Fig. 5.14.— Gas gain map of the TPC. Color maps represent the relative gas gain with respect to the mean gas gain of the whole region.

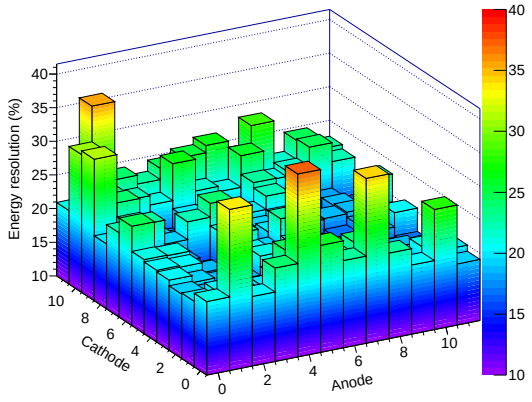

Fig. 5.15.— Distribution of the energy resolution for Ag Kα (22.2 keV). The mean energy resolution is about 21% (FWHM).

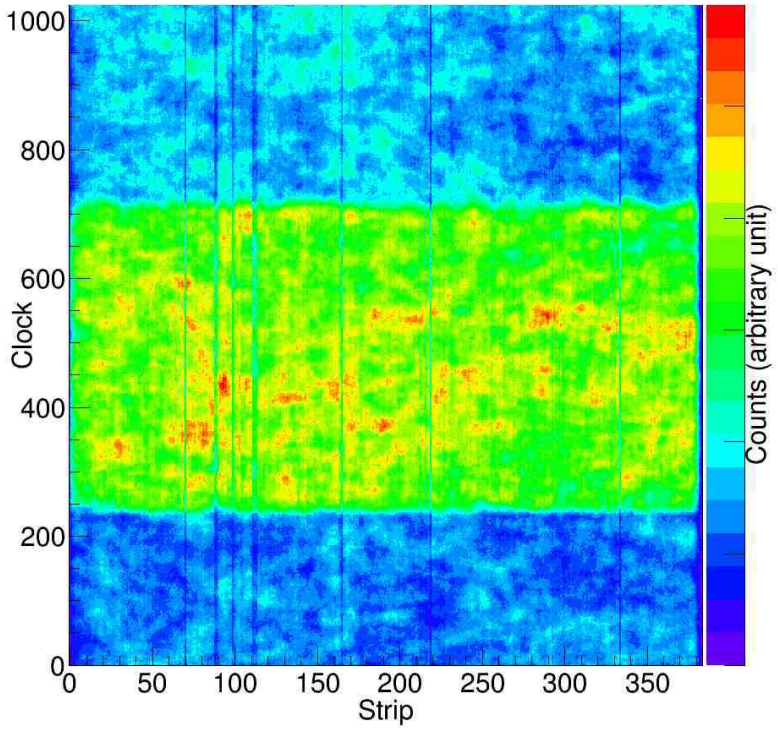

Fig. 5.16.— Clock-count distribution of ^{137}Cs irradiation experiment for each cathode strip. There is concentration in the range between 240 and 710 clock times, which represents coincidence events of ^{137}Cs.

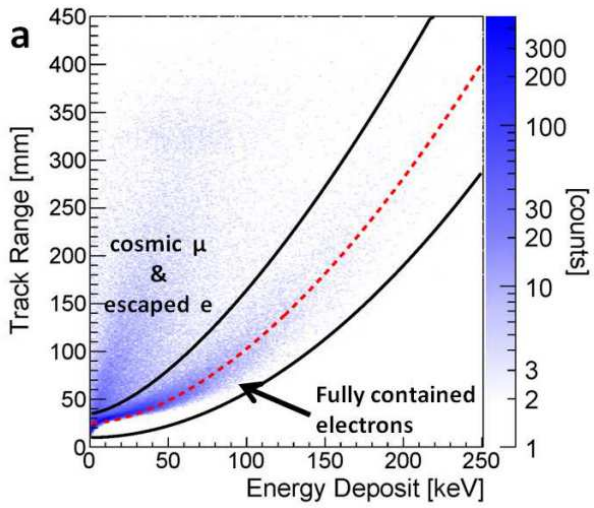

Fig. 5.17.— Track range vs the energy loss in the TPC under the condition of gamma-ray irradiation from ^{137}Cs (3 MBq) at a distance of 1 m in the laboratory [90]. The broken solid line represents the numerical calculation curves of the energy loss for fully-contained electrons.

5.3 Scintillation Camera

For an absorber of Compton cameras, scintillators and solid state detectors are widely used because of their quite better strong stopping power. We developed a Pixel non-organic Scintillator Array (PSA) [105] as the absorber of the ETCC of the SMILE-II mission with improved electronics. The PSA has some advantages compared with the solid state detector. Compared with solid state detectors, non-organic scintillator has much stopping power. Moreover, solid state detectors such as silicon or germanium detector need a cooling system and therefore they need much power consumption and space, while the scintillation camera doesn't. Also, the PSA is more suitable compared with the Anger camera using monolithic scintillator, due to a good uniformity than that of Anger camera. In term of the energy resolution, which is the critical factor of the angular resolution of the ARM for Compton cameras, the solid state detectors generally have better resolutions, and therefore we carefully chose the material of the scintillator comprehensively. Table 5.3 shows the basic properties of the various scintillators. In space use, since the radiation hardness, deliquescence, and tolerance against self-activation are required for the long operation, we adopted the GSO:Ce scntillator for the absorber of the SMILE-II ETCC, which has a moderate energy resolution of $8-9\%$ at 662 keV (FWHM), a strong radiation hardness of 10^6 Gy, and no self-activation. Since the PSA has a large readout channels of several thousands, the low power consumption and compact readout system are necessary. This requirement is critical for SMILE-II due to the increase of the coverage area of the large TPC by a factor of 3. Thus we introduced a dedicated readout system as the SMILE-II/PSA, considering both low power consumption and light weight. As a photon sensor, we chose a multi-anode Flat Panel Photomultipier tube (PMT) H8500 manufactured by Hamamatsu Photonics as shown on the left in Fig. 5.18, which was already used in SMILE-I and has an advantage of a stable gain against the operating temperature compared with a semiconductor detector such as a silicon photomultiplier and an avalanche photodiode. This PMT has a common photocathode and 64-segmented anodes with an area of 6×6 mm^2 for each pixel. The geometrical area is 52×52 mm^2 and thus the effective area is 89% of that geometrical. The typical ratio of the maximum gain to the minimum one is ~ 3. Each pixel scintillator has an incident area of 6×6 mm^2 according to the PMT pixel size and a height of 13 mm determined by the radiation length of GSO:Ce crystal (radiation length $\sim$ 13 mm). 8×8 pixels of GSO crystal forms an array unit with a reflector of ESR manufactured by 3M is inserted between the pixels, and is mounted on the PMT with an optical cement, BC-600 manufactured Bicron. To cover the TPC sufficiently, the SMILE-II/ETCC has 108 H8500 PMTs and therefore the total number of the scintillator pixels is 6912. They are placed the back and four sides of the TPC.

To reduce the number of the readout channels, the SMILE-II system uses the discretized position-sensitive circuit (DPC) [106] as well as that of SMILE-I, consisting of the array of

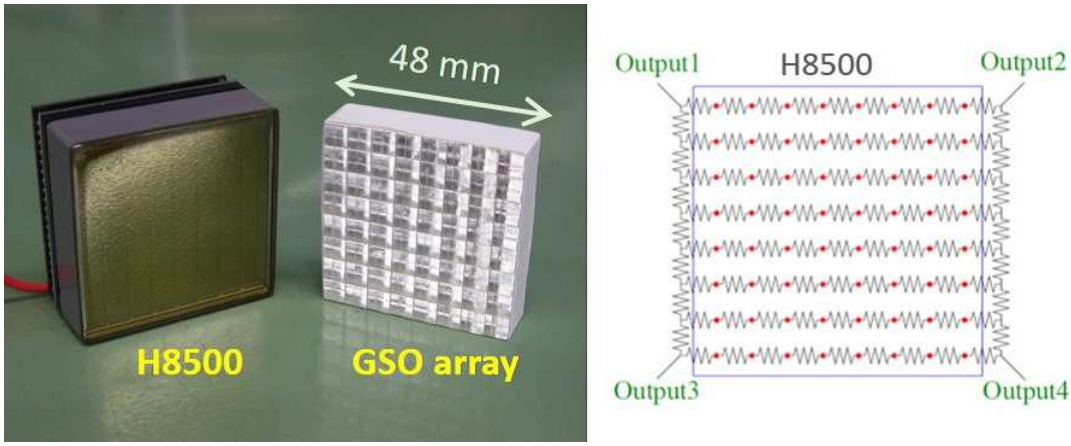

Fig. 5.18.— (Left) Multi-anode photomultiplier Hamamatsu H8500 and pixel scintillation arry of GSO crystal (8×8 pixels) [100]. (Right) Schematic view of the resistor matrix attached to a PSA, which has 64 inputs from a PSA (red circle) and 4 outputs of divided charge at the corner. [100]

the resistors that provide positional charge division as shown on the right in Fig. 5.18. In this way, 64 signals are reduced to be 4 charge-divided signals for each PMT. Figure 5.19 shows pictures of PSA readout modules, and Fig. 5.20 shows a block diagram of the front-end readout system of the scintillation camera. The readout modules of the PSA consists of a front-end module, Clear Pulse Model 80256 [100] that handles six PMT units and a VME module of a digital-signal processing board, Clear Pulse Model 80057 that manages 4 modules of the front-end modules with Ethernet cables. 4 signals of the anodes for each PMT are connected to the relatively slow pre-amplifiers ($\sim 5\,\mu$s), the shaping amplifiers ($\sim 5\,\mu$s), the sample and hold circuit and 12-bit ADCs in the readout modules, and then the pulse heights of the signals are calculated and processed to the back-end buffer in the VME module 80057. On the other hand, the last dynode signal of the PMT is connected to a fast amplifier ($\sim 1\,\mu$s) to make the trigger signal. To use the amplifiers with different time constants, this readout system provides the both fast trigger and low power consumption simultaneously. The total time between the trigger and the AD conversion is about 20 μs per event.

The energy E and position (X, Y) of the gamma-ray events are reconstructed by a summation of the pulse heights and a technique of the center of gravity (CoG), yielding

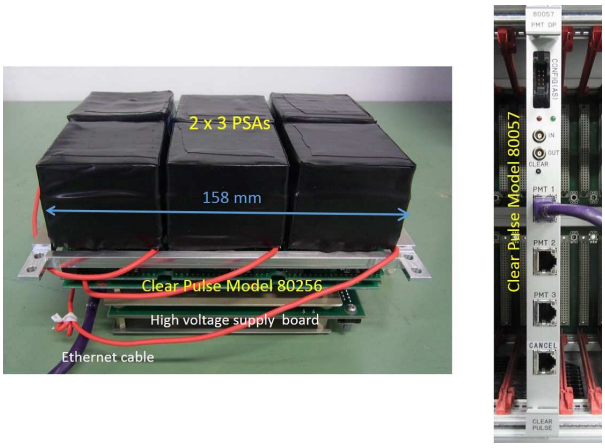

Fig. 5.19.— (Left) Photo of readout module [100]. A Front-end module, Clear Pulse Model 80256 is mounted on the back of the six PMT units. Also, the high voltage supply board is mounted on the back of the Model 80256. (Right) photo of VME digital-signal processing board that manages the signals from the four readout modules, the Clear Pulse Model 80057.

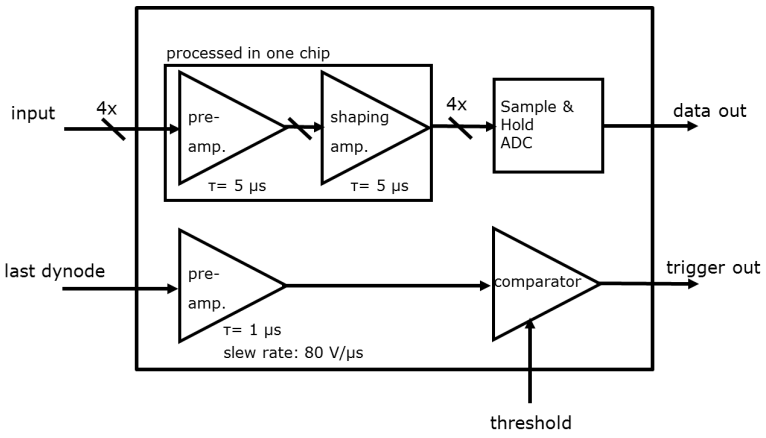

Fig. 5.20.— Block diagram of the readout system of scintillation camera.

$$E = Q_1 + Q_2 + Q_3 + Q_4 \tag{5.2}$$

$$X = \frac{Q_1 + Q_2 - Q_3 - Q_4}{Q_1 + Q_2 + Q_3 + Q_4} \tag{5.3}$$

$$Y = \frac{Q_1 - Q_2 + Q_3 - Q_4}{Q_1 + Q_2 + Q_3 + Q_4} s, \tag{5.4}$$

where Q_1, Q_2, Q_3, Q_4 are the digitized pulse heights of the charge-divided signals. For example, reconstructed hit distribution for the gamma rays with an energy of 662 keV (butterfly image) is shown in Fig. 5.21.

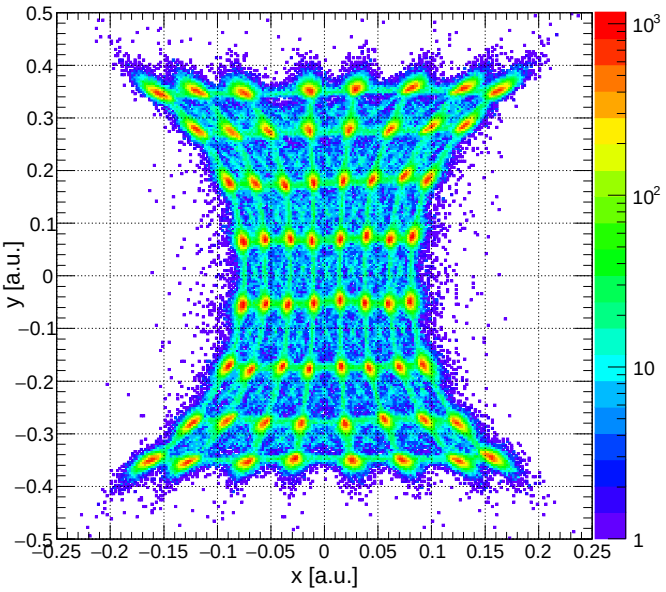

Fig. 5.21.— Reconstructed hit distribution image of the one unit of the PSA for the gamma rays with an energy of 662 keV [100].

The DAQ system of the PSA is as follows. First, when the dynode signal, which is the summation of the all signals of one PMT, from the PSA exceeds the threshold of the comparator, the PSA readout module always sends a hit signal to the trigger-control unit (TCU; as mentioned later). TCU immediately sends the analog-to-digital conversion start signals to the all readout modules, and then the all modules start processing ADCs of the PSA signals regardless of any coincidence of hits in the TPC. After sending 'start' signal, TCU sends 'clear' signals in the case of no signal in the TPC or 'valid' signals in the case that any signals exists in the TPC, alternatively. The PSA readout module discards the digitized data for the clear signal, or transfers the data to the data-processing board for the valid signal, respectively. In both cases, the PSA readout module begins to wait for the next PSA hit signal after processing the clear or valid signals.

High voltages for the six PMT units on the readout module are supplied by the high voltage supply board that is mounted on the back of the readout module, as shown in Fig. 5.22. On that board, three high voltage generator are installed and each generator supplies the high voltage to two PMT units. The supplied voltage is determined by feeding reference voltage to the high voltage generator via the microprocessor and the DAC on the board, and controlled with the RS-232C signal interface on the board.

The performance of the PSAs is summarized in Fig. 5.23 and 5.24. The distribution of the gain of the all GSO pixels in the SMILE-II/ETCC is shown in Fig. 5.23 (a), and has a deviation of 25% at 1σ. The energy resolutions of the all pixels for the same condition are distributed from 10% to 14% at 662 keV, as shown in Fig. 5.23 (b). The energy resolution dependence on the gamma-ray energy as the entire scintillation camera is shown in Fig. 5.24, and the energy resolution of the entire scintillation camera system is approximately 11% at 662 keV.

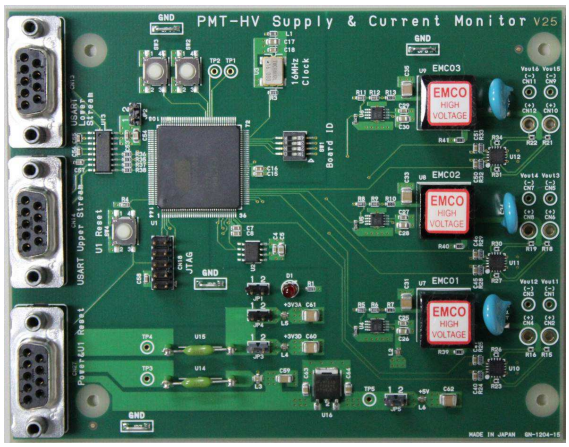

Fig. 5.22.— Photo of HV supply board for the scintillation camera.

Table 5.3— Comparison of inorganic scintillator

Name (activator) (abbreviation)	NaI(Tl)	CsI(Tl)	BaF_2	Gd_2SiO_5(Ce) GSO	$Bi_4Ce_3O_{12}$ BGO	$LaCl_3$	$LaBr_3$	$Lu_3Al_5O_{12}$(Pr) LuAG
density [g cm^{-3}]	3.67	4.51	4.89	6.71	7.13	3.79	5.29	6.7
Energy resolution*[%] FWHM at 662 keV)	6-7	6-7	9	8-9	10-12	3-4	3	8
Radiation length [cm]	2.59	1.86	2.03	1.38	1.12	2.4	2.1	∼13.5
Attenuation time constant [nsec]	230	680,3340	0.6,620	30-60	300	28	16	20
Maximum emission wavelength [nm]	415	540	220,310	440	480	350	380	310
Light yield(NaI(Tl)=100)	100	45	5,16	20	7-10	130	160	30
diffraction	1.85	1.80	1.56	1.85	2.15	~ 1.9	~ 1.9	n/a
melting point [^{o}C]	650	621	1350	1900	1050	859	783	1970
Deliquescence?	Yes	Yes but weak	No	No	No	Yes	Yes	No
Radiation hardness [gray]	10	10^3	10^{3-4}	10^6	10^{2-3}	$> 3.4 \times 10^3$	$> 3.4 \times 10^3$	n/a
Self-activation?	No	No	No	No	No	Yes	Yes	Yes

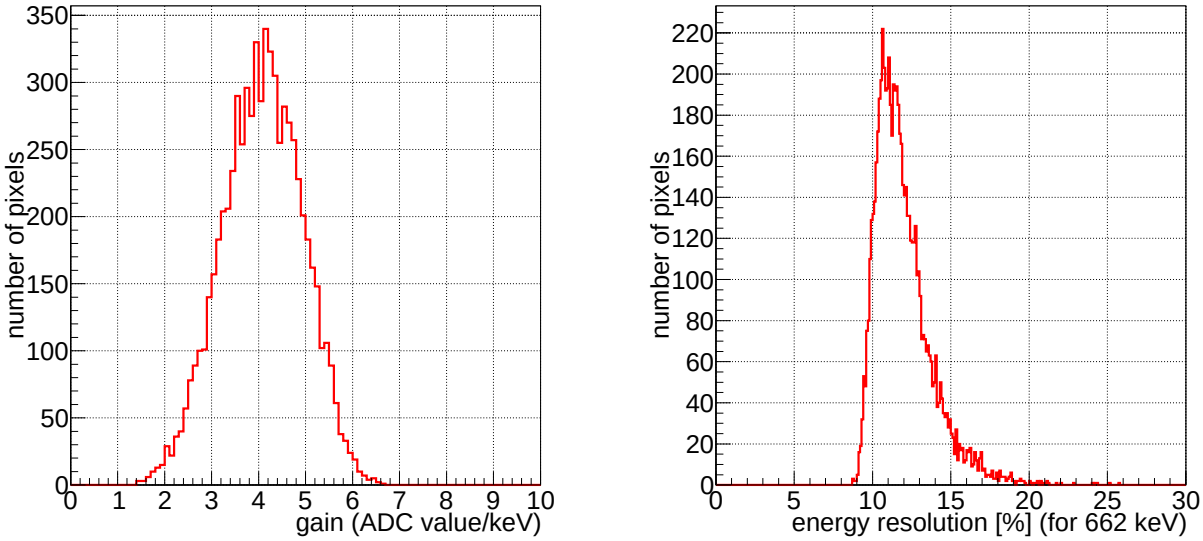

Fig. 5.23.— (a) Gain distribution of the whole channels of the scintillation camera [100]. The unit of the gain is ADU/keV and divided by the average. (b) the same but for the energy resolution at FWHM for 662 keV [100].

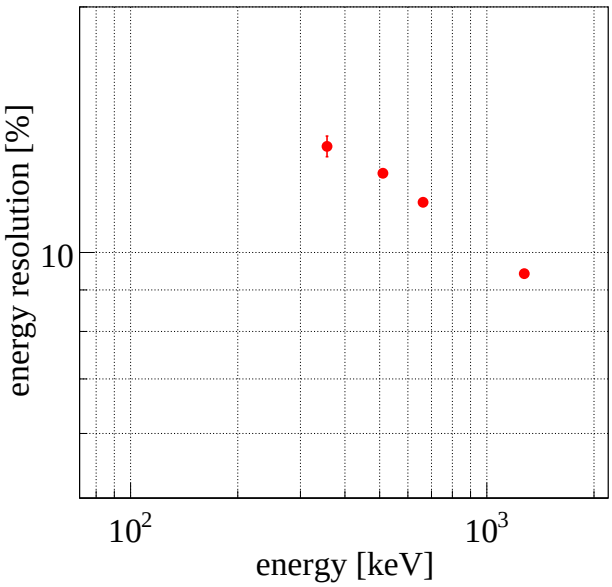

Fig. 5.24.— Energy resolution of the entire scintillation camera as a function of the incident gamma-ray energy [100].

5.4 ETCC DAQ system

The SMILE-II/ETCC DAQ system has been improved completely from that of SMILE-I, and comprises two main parts: the front-end system consisting of the TPC readout, PSA readout and trigger-control unit (TCU), and the memory buffers or VME-bus system as the back-end system including CPU. Each system of TPC or PSA works individually and the data are continuously stored in the memory module in the VME to reduce the dead time. A block diagram of the SMILE-II/ETCC DAQ system is shown in Fig. 5.25. In the front-end system, TCU manages the trigger signals to control start/stop of the data acquisition. TCU consists of a stack of several boards: one main board, two TPC-input/output(I/O) boards, three PSA-I/O boards, one GPS-I/O board, and one power supply board as shown in Fig. 5.26. On the main board, an FPGA with a clock of 100 MHz and an Ethernet port are installed, which is controlled by the DAQ CPU via Ethernet. The FPGA on TCU main board controls the TPC readout boards and the PSA readout modules, via TPC-I/O and PSA-I/O boards, respectively. The TPC-I/O board has four sets of I/O ports and can manage 4 boards of the TPC readout boards. The PSA-I/O boards has six sets of I/O ports for six PSA readout modules. TCU can expand the number of the I/O ports by stacking the I/O boards according to the scale of the ETCC system. The GPS-I/O board generates another trigger from peripheral equipments such as a GPS and an anti-coincidence counter and manages the global time. It has a serial input port to obtain the global time from the GPS, a PPS signal input for a force trigger, and five veto trigger inputs for charged particle event rejection.

TCU has three DAQ modes: ETCC, TPC-calibration, and PSA-calibration modes. The flow chart of the ETCC mode is shown in Fig. 5.27. First, at the stand-by state, TCU waits for the signal from the PSAs that is generated when the dynode signal exceeds the threshold. When TCU receives any signals from PSAs, it in return sends a trigger signal (GSO signal) to the all PSA readout modules via PSA-I/O boards. Synchronously, TCU also sends a trigger to the all TPC readout boards after $8\,\mu$s at the GSO trigger. While the PSA readout modules immediately start the analog-to-digital conversion, the TPC readout boards check if there are any hits within the latest $10\,\mu$s in the ring buffer that stores the hit position data, of which duration time is determined by the longest drift time in the TPC of $\sim 6\,\mu$s for the argon-based CF_4-mixture gas. If TCU receives any data-exist flags from the TPC readout boards, TCU sends to the all system the valid signal to inform that event should be stored. Otherwise, if no data-exist flag is sent, TCU sends the clear signal to discard the current data and returns to the stand-by state. Once the valid signal from TCU is received, all the TPC readout boards and PSA readout modules send their data to the corresponding memory-buffer and data-processing boards on the VME bus. After sending the data, they recover to the stand-by state to wait for the next event. Anytime, the on-board CPU in the

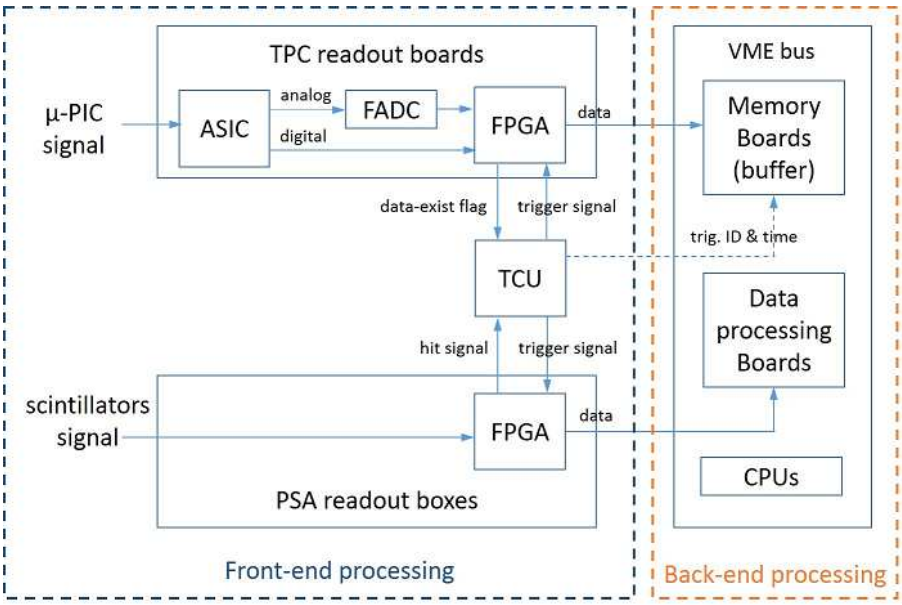

Fig. 5.25.— Block diagram of SMILE-II/ETCC DAQ system [100].

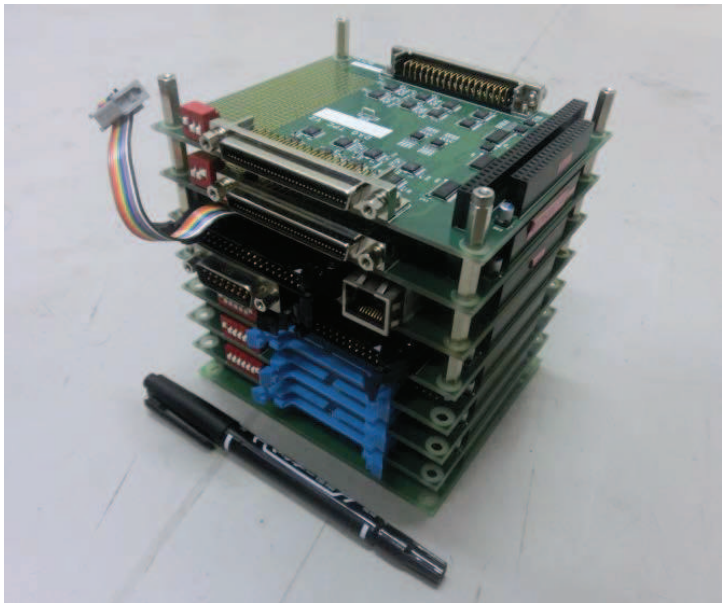

Fig. 5.26.— Picture of Trigger-Control Unit (TCU), consisting of a main FPGA board, two TPC-I/O boards, three PSA-I/O boards, one GPS-I/O board, and one power-supply board [100].

VME bus can read the multi events data on the memory-buffer and data-processing boards. In this way, the interrupt latency of the CPU is dramatically reduced and the front- and back- end circuits can be processed in parallel. Figure 5.28 shows the live time of the new DAQ system as a function of the valid signal rate, and the live time is about 80% at 100 Hz. The minimum requirement for the SMILE-II DAQ system is that the live time is more than 70% at 100 Hz, and thus the new DAQ system satisfies that requirement.

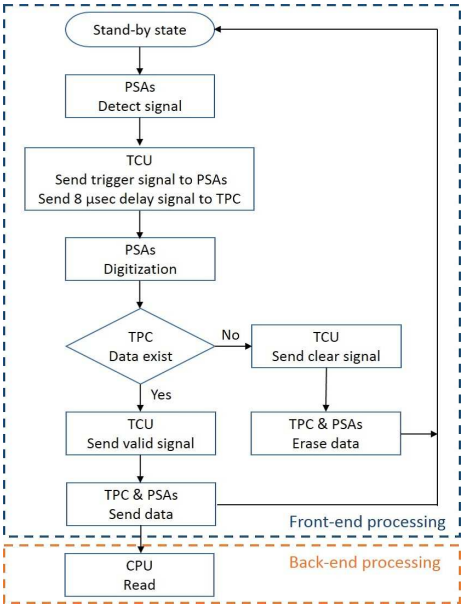

Fig. 5.27.— Flow chart of the ETCC mode in the SMILE-II/ETCC DAQ system [100].

In the case of the TPC- or PSA- calibration modes, there is no necessity of the coincidence between the PSA and TPC signals. Therefore, in the PSA-calibration mode, TCU generates the valid trigger as soon as it receives the hit trigger from the PSAs regardless of the state of the TPC. On the other hand, in the TPC-calibration mode, TCU regard the first hit signal from the TPC readout boards as the event trigger instead of the trigger from the PSAs.

5.5 Event Reconstruction and Selection

An event reconstruction and a selection of Compton event from the background is performed in an off-line analysis software, which is developed using C++ and the ROOT toolkit [107]. The analysis software consists of several modules as shown in Fig. 5.29, in which the module dependence is depicted by arrows, meaning that for example 'PSA Center

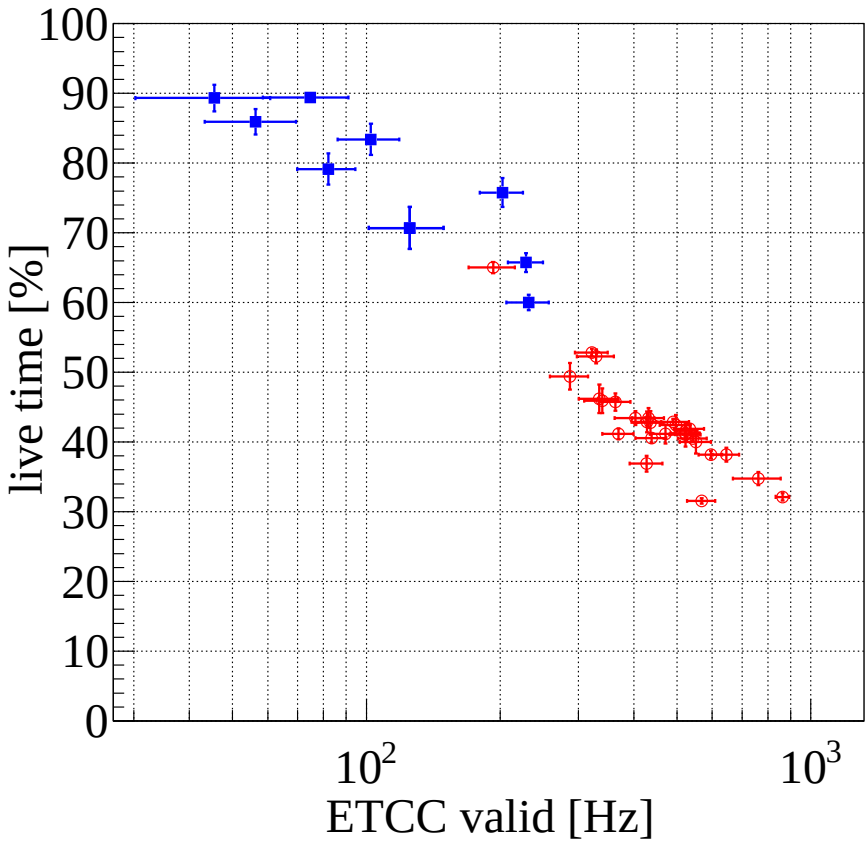

Fig. 5.28.— Live time dependence on the vaild signal rate [100]. The filled squares and open circles show data measured in the laboratory and RCNP, respectively.

of Gravity' module should be called after 'PSA decode' module is processed. In the 'PSA decode' module, we require following criteria, and then ADC values are extracted. (1) The PSA hits should not be multiple per event, because a complete Compton event should have one gamma-ray hit on the PSA. For the current SMILE-II ETCC configuration, the PSA readout electronics can recognize the multiple hit events if there are some hits at more than one unit of PMT. (2) The ADC value of the PSA should not be saturated, because the energy lose of the MIPs such as cosmic muons is high enough to saturate the signal of the PSAs. Then, the ADC values of the PSA satisfying those conditions are passed to the 'PSA Center of Gravity' module and the gamma-ray hit position on the PSA is calculated. The 'PSA calibration' module calibrates the scattered gamma-ray energy from the data, in which the gain in the PSA amplifier is compensated by the calibration database. The reconstructed 'absorption' position and energy are used to the 'Compton reconstruction' and 'TPC hit analysis' modules. The analysis of the TPC data is started from the 'TPC decode' module, which converts the raw hit data to the two sets of two-dimensional time-projected hit data of the strip-clock plane, and decodes the raw flash ADC data to a pulse height. The 'TPC calibration' module calculates the energy loss in the TPC using the pulse height. The hit positions are processed in the 'TPC hit analysis' module, where the vertex points, momenta and range of the recoil electrons are calculated. The 'Compton reconstruction' module requires the energy losses and vertex positions in the PSA and TPC, respectively, and the momentum direction and range of the charged particle in the TPC, and stores these data as the event table.

Algorithms to calculate the scattering and absorption positions of the gamma-rays and the direction of the recoil electrons are important for the angular resolutions of the both ARM and SPD. To determine the coordinate of the absorption point in the PSA, the scintillator pixel is firstly identified in the butterfly image, and then the coordinate of the center of the pixel is regarded as the absorption point, because one cannot know the real absorption point within the scintillator pixel. The Compton-scattering points and the direction of the recoil electrons are determined by the two sets of the two-dimensional hit images whose space are the clock of the TPC (z-axis) versus the position number of the μ-PIC strip (x-axis for cathode and y-axis for anode). First, the three-dimensional track is reconstructed by the off-line coincidence of the x-z and y-z images in the three-dimensional space. Next, the projection to the x-y plane is made from the three-dimensional track. We consider that the scattering point projected to the x-y plane must be located at the closest hit point from the absorption point [103]. We also consider that the z-coordinate of the scattering point corresponds to the mean of the hits in the 3-d track satisfying the condition on the x-y projected plane. The direction of the recoil electron is determined as a composite sum of two vectors of the gradients of the obtained two-dimensional hit images of x-z and y-z planes.

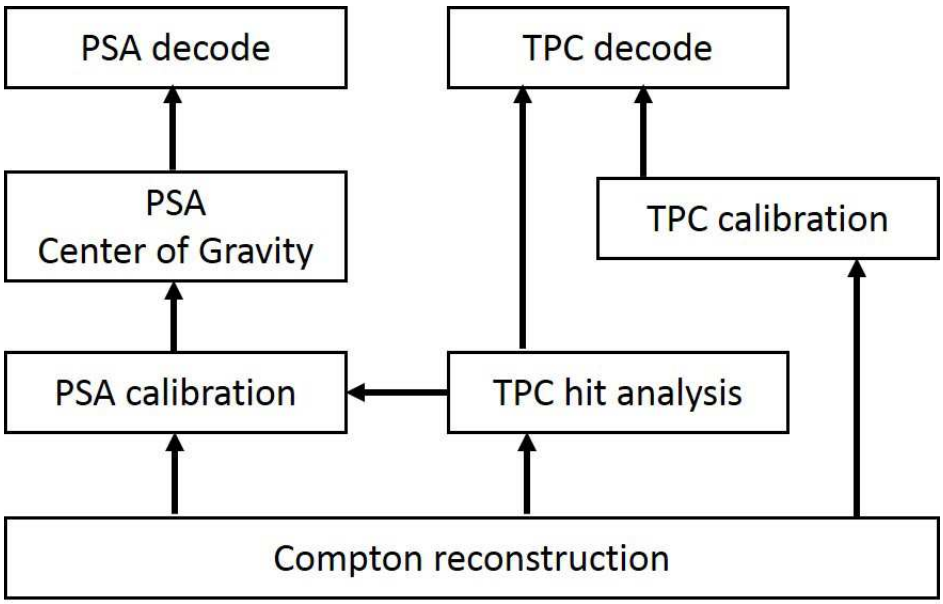

Fig. 5.29.— Diagram of the ETCC reconstruction modules and their dependence. The arrows point from the dependents at the tails to the providers at the arrowheads.

Real Compton events are taken with a coincidence between the TPC and PSAs in the ETCC. There exists, however, background events such as random coincidence events, charged particles such as cosmic muons, environmental gamma rays, and incomplete events with a lack of information on vertex or energy loss for the Compton events from the source of interest. To extract the events in which Compton scattering occurs in the active volume in the TPC, the Compton-recoil electron stops within that active volume, and the photoelectric absorption arises in the scintillator by scattered gamma ray, the coincidence events are examined for a couple of following selection criteria.

Energy loss rate cut Energy loss rates (or, stopping power) varies depending on β, or the velocity of the particle. For the electrons in the argon gas with an energy up to a few hundred keV, the practical range R_p is approximately described as $R_p = 0.71 \left(\frac{E}{1\,\mathrm{MeV}}\right)^{1.72} \mathrm{g\,cm^{-2}}$, where E is the energy of the electron [108]. To reject the high energy electrons escaping from the active volume of the TPC or heavy ions, energy loss rate cut is applied as follows,

$$\begin{cases} R_p \leq (1/\rho)0.71 \times E_e^{1.72+a_u} + b_u \\ R_p \geq (1/\rho)0.71 \times E_e^{1.72+a_l} + b_l \\ R_p < R_p^{\mathrm{lim}} \end{cases}, \tag{5.5}$$

where E_e is the energy loss in the TPC, ρ is the density of the gas of the TPC, and R_p is the practical range of the charged particle trajectory in the TPC. a_u, b_u, a_l, b_l, and R_p^{lim} are constants for the event selection. The range R_p is derived by calculating the length of the diagonal of the rectangular that surrounds the three-dimensional particle trajectory, formally described as

$$R_p = \sqrt{(x_{\max} - x_{\min})^2 + (y_{\max} - y_{\min})^2 + (\min(z_{\mathrm{x,max}}, z_{\mathrm{y,max}}) - \max(z_{\mathrm{x,min}}, z_{\mathrm{y,min}}))^2} \tag{5.6}$$

where $x_{\max}$ and $x_{\min}$ are the maximum and minimum position coordinates in the cathode hits, respectively, $y_{\max}$ and $y_{\min}$ are the same but for the anode hits, $z_{\mathrm{x,max}}$ and $z_{\mathrm{y,max}}$ are the maximum position coordinates of the hits in the drift direction for cathode and anode strip data, respectively, and $z_{\mathrm{x,min}}$ and $z_{\mathrm{y,min}}$ are the same but for the minimum position coordinates.

Fiducial volume cut charged particles coming from the outside of the active volume of the TPC cannot be measured the total kinetic energy properly. To remove such events, the events for which there are hits near the edge of the active volume in the TPC are considered as bad events transporting the boundary of the active volume.

Total energy loss cut For the calibration source, the incident energy of the gamma rays is already-known. To test the detection efficiency of the gamma rays from radioisotopes,

we lay down the condition where the summation of the energy losses in the TPC and PSA should be equal to the incident gamma-ray energy, or

$$\left| \frac{E_{\rm tpc} + E_{\rm psa}}{E_{\rm inc}} - 1 \right| \leq p, \tag{5.7}$$

where $E_{\rm tpc}$, $E_{\rm psa}$ and $E_{\rm inc}$ are the energy losses in the TPC and PSA, respectively, and the incident energy, and p is the fraction of acceptable residual.

5.6 Performance of the SMILE-II/ETCC

The first performance test of the SMILE-II/ETCC was investigated using the radioisotopes of ^{139}Ce (166 keV), ^{133}Ba (356 keV), ^{22}Na (511 keV), ^{137}Cs (662 keV), and ^{54}Mn (835 keV). Here, the parameters in event selection criteria are set to be as follows. For the energy loss rate cut, $a_u = -0.22$, $b_u = 3.5\,[\rm cm]$, $a_l = +0.22$, $b_l = 1\,[\rm cm]$, $R_p^{\rm lim} = 32.5\,[\rm cm]$, and $\rho = 1.74 \times 10^{-3}\,[\rm g\,cm^{-3}]$. As the fiducial volume cut, the fiducial volume is set to be the rectangular covered with the six planes of $z = -30\,[\rm mm]$, $z = -300\,[\rm mm]$, $x = \pm 145.6\,[\rm mm]$, and $y = \pm 145.6\,[\rm mm]$, while the active volume of the TPC is the one of $x = \pm 153.6\,[\rm mm]$, $y = \pm 153.6\,[\rm mm]$, $z = -7.9\,[\rm mm]$, and $z = -319.9\,[\rm mm]$. Figure 5.32 shows the energy resolution of the ETCC, and its dependence on the incident gamma-ray energy is described as

$$\frac{\Delta E}{E} = 10.7 \times \left(\frac{E}{662\,\rm keV} \right)^{-0.5} [\%] \quad (\rm FWHM). \tag{5.8}$$

Hereafter, the parameter p on the energy cut is set to be the FWHM, corresponding to the energy range of ± FWHM from the incident energy. The effective area is calculated by counting the events under the condition where the total energy loss is consistent within the twice FWHM of the energy resolution from the incident gamma-ray energy. Figure 5.30 shows background-subtracted energy spectra of ^{137}Cs. The black points represent the raw data, and the red, green, and blue points the remaining events after applying the energy loss rate cut, the fiducial volume cut, and the total energy cut, respectively. One can see about half of the raw events are rejected by the energy loss rate cut, and this fraction agrees to prediction by the simulation (See Figure 6.22). Figure 5.31 shows a correlation between the scattering angle $\phi_{\rm kin}$ and $\phi_{\rm geo}$, that are one derived by kinematics and one geometrically, respectively. One can see that the correlation is enhanced after applying the energy loss rate cut. Figure 5.33 shows the line-of-site effective area of the SMILE-II/ETCC with a simulation result (See the chapter 6), which has a good consistency with errors of +26%, −6%, −14%, −6%, and −10% for 166 keV, 356 keV, 511 keV, 662 keV, and 835 keV, respectively. One of causes of the discrepancy for an energy of 166 keV is thought to be the detection inefficiency of the events which are absorbed in the PSA with a low gain. This is because that data of

gamma-rays with an energy near the energy threshold would have too low signal-to-noise ratio to reconstruct the position, and then some of them cannot be used to reconstruct the direction. On the other hand, one of the reason for the systematical discrepancy at higher energy is thought to be chance coincidence. In fact, there is still some excess at an energy range higher than 700 keV on the background subtracted spectrum of ^{137}Cs, suggesting the chance coincidence between the environmental and radioisotope gamma rays. We fitted that excess by a first order polynomial function, and then found that we would have overestimated the measured detection efficiency of RI sources by a factor of $\sim 20\%$ at worst due to the contamination of that excess. In order to reduce such systematic errors, further cuts such as the kinematics test and constraint for the incident direction will work efficiently. Figure 5.34 shows the angular resolution of the ARM for the SMILE-II/ETCC measured, and the calculations for GSO and $LaBr_3$ crystals derived by the uncertainty of the measurement of the energy of the scattering gamma rays. The measured ARMs are close to the limit of the calculation, and comparable to that of Compton cameras based on a semiconductor detector. For example, NCT at the balloon experiment in 2009 had an ARM of 7.4° for Crab, which was limited by the position resolution [79]. The discrepancies between the measured ARMs and the calculation indicates the uncertainty of 8 mm for the measurement of the scattering position in the TPC. Figure 5.35 shows the SPD distribution for the radioisotope of ^{137}Cs (662 keV), and the FWHM of the SPD is about 200 degrees, which is about two times worse than the expected SPD resolution, due to multiple scattering in the gas. The deterioration of the SPD resolution is mainly due to an ambiguity from multi-hits on the orthogonal two-dimensional strip readout in the TPC. In general, n-hits on anode and cathode strips in the same timing generate n^2 points as the coincidence hits, and thus a part of the track running horizontally to the μ-PIC is obtained as a square instead of a line. In this analysis, a timing resolution of near 10 ns from the clock of the FPGA (100 MHz) was used. To overcome this issue, an improvement of the track data analysis is being carried out (See [90]).

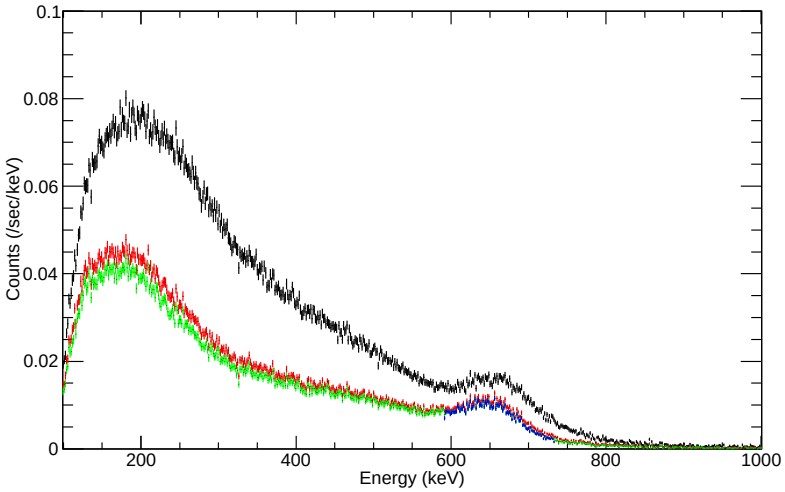

Fig. 5.30.— Energy spectra of the ^{137}Cs irradiation experiment for the all events (left top) and remaining events after applying the energy loss rate cut (right top), the fiducial volume cut (left bottom), and the total energy cut (right bottom), respectively.

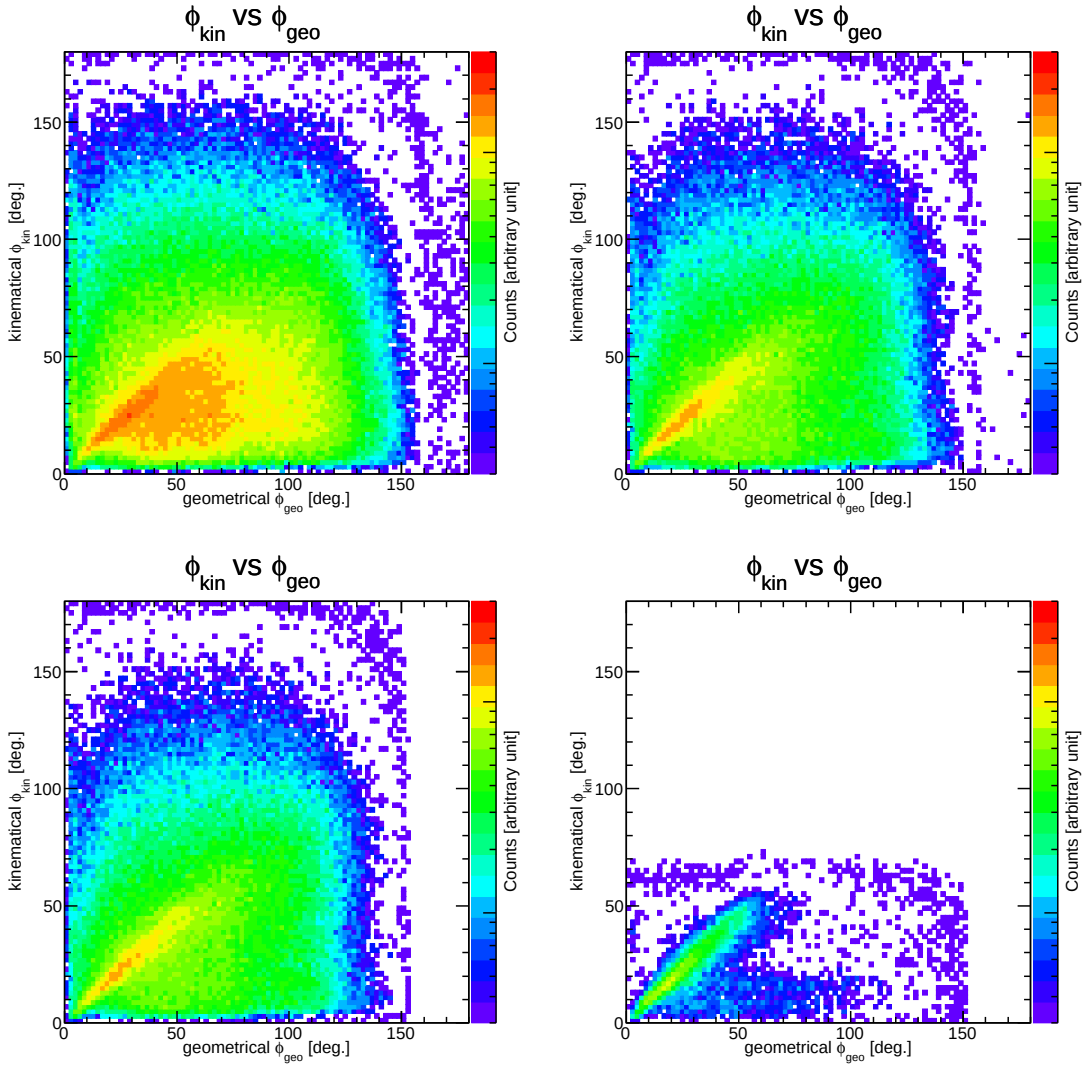

Fig. 5.31.— Correlation between $\phi_{\rm kin}$ and $\phi_{\rm geo}$ of the ^{137}Cs irradiation experiment for the all events (left top) and remaining events after applying the energy loss rate cut (right top), the fiducial volume cut (left bottom), and the total energy cut (right bottom), respectively. The data set is the same as that of Figure 5.30.

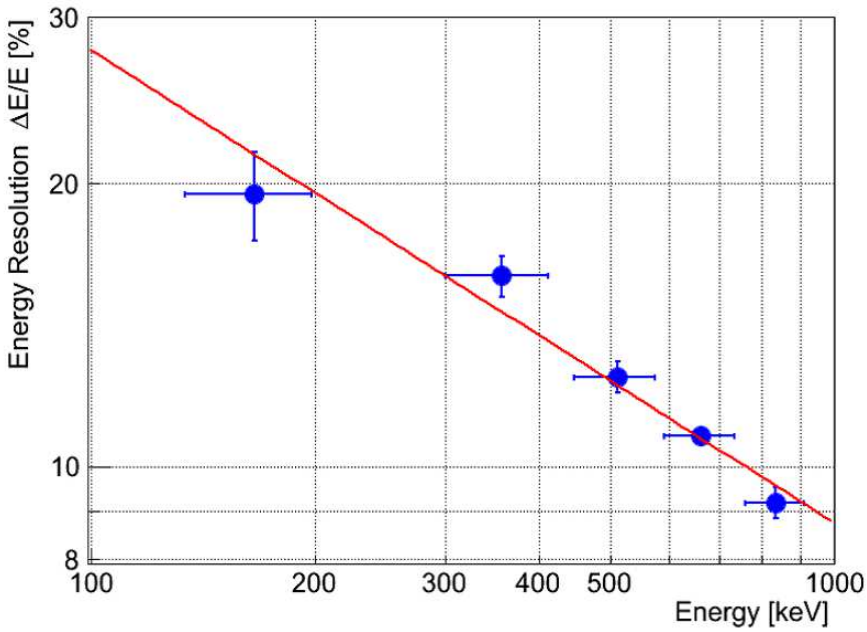

Fig. 5.32.— Energy resolution of the SMILE-II/ETCC. The fitted line is also shown with the red line.

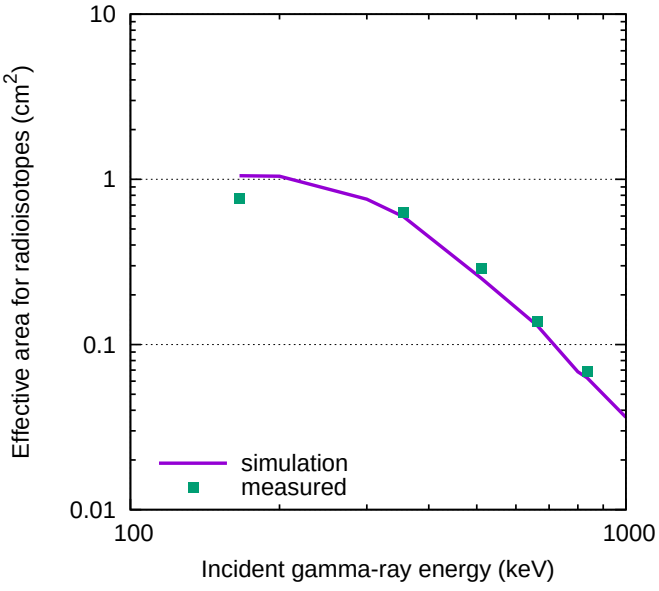

Fig. 5.33.— Effective area of the SMILE-II/ETCC for the RI sources (green solid triangle). The simulated effective area is also shown with the purple line.

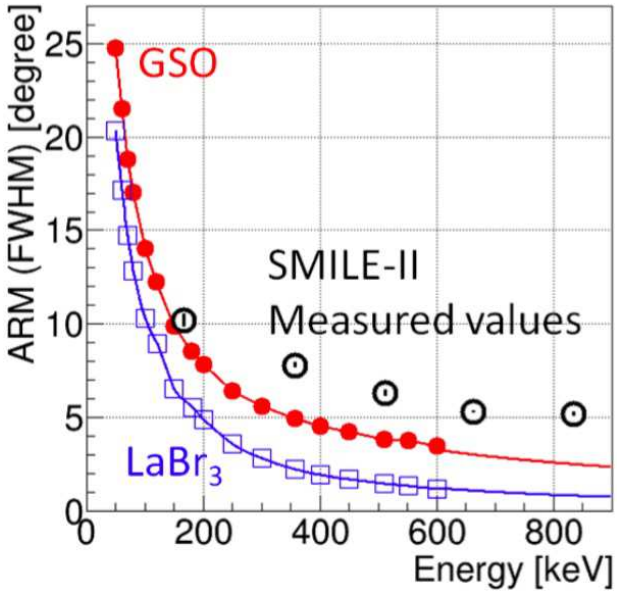

Fig. 5.34.— The energy dependence of the ARM of the SMILE-II/ETCC (open black circle). Calculations by the energy uncertainty are plotted with filled red circle and open blue square for GSO and $LaBr_3$ crystals, respectively [90].

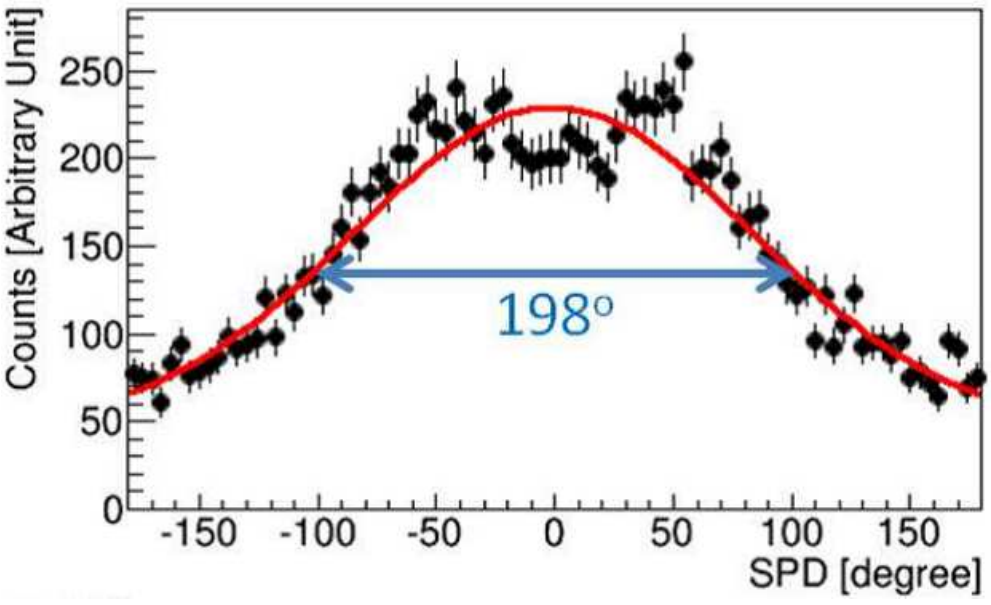

Fig. 5.35.— SPD distribution of the SMILE-II/ETCC using the simple track reconstruction method for an incident gamma-ray of 662 keV [90].

Chapter 6

Detector Simulation

A detector simulator is essential for both the development and the observation. First, in order to obtain the gamma-ray flux of the celestial objects from raw event data, the response of the detector such as the detection efficiency must be accurately estimated. However, the event selection efficiency such as the energy loss rate cut cannot be estimated quantitatively only with the experimental data. Second, for the future development, one should know what is the predominant factor for the detection efficiency. Third, the precise detector simulator will provide a test bench for the algorithm to determine the vertexes and momenta of Compton-recoil electrons, which is critical for the improvement of the SPD and therefore PSF. The configuration of the SMILE-II ETCC is quite different from that in SMILE-I, and there were no detector simulators which reproduce electron track data obtained with the SMILE-II TPC. Therefore we developed a detector simulator, which reproduces the electron track data. The goal of the development of the simulation is to validate the measured detection efficiency comparing to the simulator within 10% level. Since the interaction between gamma-ray and matter occurs not only in the active volume of the detector but also the equipment and surrounding systems, we need a Monte Carlo calculation so as to consider such influence. In this chapter, the detection efficiency is calculated by two steps; the first is the one responsible for the structure of the detector and physics process for the detector design, and the next is the one including the circuit response and reconstruction algorithm for the practical use. The selection efficiency of Compton-recoil electron events is also discussed. Consequently, which is the predominant factor for the detection efficiency is discussed.

6.1 Physics Model

To study the detection efficiency of Compton scattering events with an ETCC, we developed a Monte Carlo simulation software based on the Geant4 tool kit (ver. 4.9.5p01) [109]. Since the energy range of the SMILE-II FM is designed to be between 0.15 and a few MeV, we used the Livermore package for the electromagnetic process, which simulates precisely the process of the interaction between material and low-energy gamma rays with an energy of less than 1 MeV including the Doppler broadening effect. The detection criteria of the Compton scattering events on the simulation are following conditions: (a) Compton scattering occurs in the TPC volume, (b) the photoelectric absorption occurs in the PSA for the scattering gamma ray, (c) the recoil electron should be stopped in the TPC, (d) the energy deposits in the TPC and PSA exceed the detector thresholds, and (e) without the loss of the incident photon energy within a certain energy resolution, formally described as Eq. 5.7. Here the particle identification by dE/dx of a recoil electron is emulated by the criteria 'c'. According to the real detector, the detector thresholds are set to be 1 keV and 90 keV for TPC and PSA, respectively. We used the energy resolutions of the TPC and PSA following Gaussian distribution with the FWHM of 22% for 22 keV and 10% for 662 keV, respectively, that is determined by measurements [110], having an energy dependence of $E^{-0.5}$ due to statistical fluctuations. In the criterion (e), we used $p = 0.1$ just for comparison of the efficiencies between the measurement and simulation. To simplify the detection criteria, we didn't limit the events where the gamma ray is scattered and then absorbed in the PSA, or the gamma rays is scattered with the TPC chamber on the way to the PSA.

To confirm the validity of this efficiency simulation, we compared the simulated detection efficiency to the measured one with a small ETCC. We note that here we focus on the detection efficiency depending on the dE/dx cut and the spectrum cut, and don't consider the directional cut by the on-source region according to the PSF. Its geometry is shown in Fig. 6.1. The TPC has an active volume of $14.1 \times 7.68 \times 7.68\,\mathrm{cm}^3$ with a gas mixture of Ar(90%)+C_2H_6(10%) at the gas pressure of 1 atm, which is sealed with the vessel made of aluminum and carbon fiber reinforced polymer. The PSA consists of the 9×9 multi-anode PMTs behind the TPC at a distance of 52 mm. Each PMT unit has 8×8 pixel scintillators made of GSO:Ce crystal with a size of $6 \times 6 \times 13\,\mathrm{mm}^3$. Figure 6.2 shows the comparison of the simulated and measured detection efficiencies, and the consistency between the simulated and measured ones is within 30% in 0.35 - 0.7 MeV. The large discrepancy at 662 keV is understood because the geometry, where the PSA is placed only on the bottom of TPC, enhances the forward scattering events, but in the simulation the multiple scattering in the PSA is allowed and gamma rays with an energy of 662 keV cause Compton scattering rather than photoabsorption. Nevertheless, it is implied that the dE/dx particle identification inefficiency caused by misidentification and circuit response is limited to be such level. In

other word, the ETCC can selectively extract most of the Compton events of which the recoil electrons stopped in the scatterer from the all triggered events.

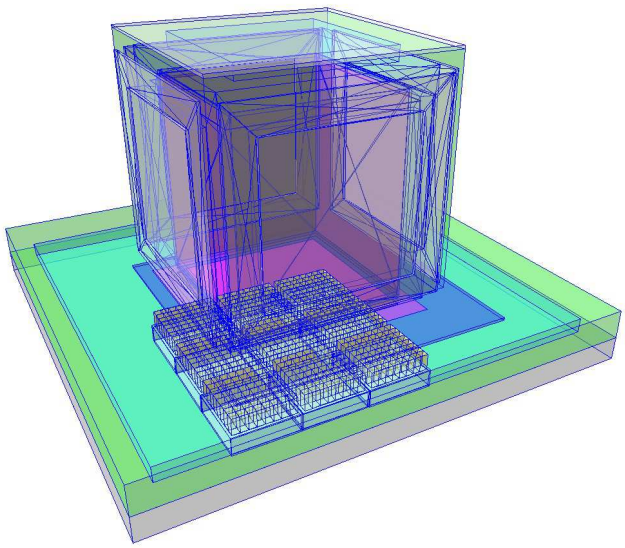

Fig. 6.1.— Geometry of 10-cm-cubic ETCC constructed in Geant4.

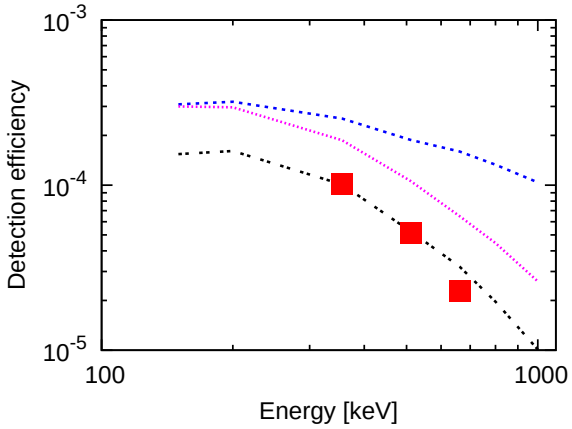

Fig. 6.2.— Comparison of the detection efficiency of the small ETCC between simulation and measured one. Each line represents the simulated detection efficiency based on 'a and b' (dashed blue), 'a, b, and c' (dotted magenta) and 'a, b, c, d, and e' (double-dashed black), respectively. Each alphabetical character such as 'a' represents the detection criteria as mentioned in the text. The plotted measured data (closed square) are quoted from Komura *et al.* [103].

6.2 TPC Detector Model

The readout electronics of the SMILE-II TPC with the new ASIC is improved in terms of two aspects. One is the software coincidence between anode and cathode hits, resulting the recovery of the hit detection efficiency. The other is the recording of the TOT on each strip channel, involving the information on the energy deposit that is useful to identify the vertex of Compton scattering. In this section, in order to estimate quantitatively the ability of energy loss rate cut of the TPC, simulations of the TPC are developed as following steps. First, the ionization and drift process in the TPC is modeled with a Monte Carlo method. Second, gas avalanche and μ-PIC waveform response is introduced. Finally, the electronics and the comparators that produce TOT outputs emulator is developed and compared with the experimental data derived by test pulses. Figure 6.3 shows a schematic block diagram of the TPC detector simulator. The practical use of the TPC simulator and the estimate of energy loss rate cut efficiency is discussed in the next section.

6.2.1 Primary ionization and drift

When a charged particle comes in a TPC, the gas in the TPC is ionized and electrons are emitted. These electrons travel along to the electric field in the drift space and then reach the surface of the μ-PIC. The number of produced electron-ion pairs n_0 is described as

$$n_0 = E/W, \tag{6.1}$$

where E is an energy deposited in the gas by an incident charged particle, and W is a mean energy to produce one ion-electron pair. The fluctuation in the production of the ion-electron pairs is described by the Fano factor F:

$$\sigma_{n_0}^2 = F n_0. \tag{6.2}$$

Produced electrons drift along the electrostatic field. The collision of electrons with gas molecules is a random process and therefore the spatial distribution of the electrons is determined by the diffusion coefficient. We use a simple model for the charge diffusion in the 3-dimensional space, as a Gaussian distribution with a standard deviation proportional to the square root of time, $\sigma(t) \propto \sqrt{t}$. In a constant electric field, the electron cloud drifts to the detector plane with a constant velocity, $v_{\mathrm{drift}} = z/t$, and then the width of diffusion distribution is proportional to the square root of the absolute drift distance z, or

$$\sigma = D\sqrt{z}, \tag{6.3}$$

where D is known as a diffusion coefficient. Since it has a dependence on the direction toward the electric field, there are transverse and longitudinal diffusion coefficients. The diffusion

coefficients also vary depending on the composition of the gas mixture and the electric field. Figure 6.4 shows the transverse and longitudinal diffusion constants of the gas filled in the SMILE-II TPC, calculated by the Magboltz [104] software.

In order to simulate such a situation, we started from the data set of energy loss of a charged particle that is derived by Geant4. The step limit used in Geant4 is set by a path length of 40 μm, which is small enough compared to the pitch of the electrodes of μ-PIC. Let us suppose that the data set is denoted as $\{(x_i, y_i, z_i, E_i)|i = 1, 2, 3, \cdots, M\}$. Next, we calculate the number of produced seed electrons according to Eq. 6.1 fluctuated by a Gaussian distribution with a variance of Eq. 6.2 to derive the data set of $\{(x_i, y_i, z_i, N_i)|i = 1, 2, 3, \cdots, M\}$. The total number of the ionized electrons $N_{\rm seed}$ yields $N_{\rm seed} = \sum_{i=1}^{M} N_i$. For each seed electron, spatial fluctuation is randomly given according to the diffusion effect of Eq. 6.3. $N_{\rm seed}$ of electrons are counted on the projected 2-dimensional histograms of which the bin size is 800 μm for the strip pitch and 1/20 of the TPC clock of 10 ns for drift direction.

6.2.2 μ-PIC Response

An avalanche process and a current waveform of μ-PIC are investigated [111] with a Monte Carlo method. First, we calculate the electric field near the μ-PIC with Gmsh [112] and Elmer [113], and then simulate the drift and avalanche of electrons with Garfield++ [114]. In the Gmsh, the geometry of the μ-PIC is constructed for a three dimensional finite element method as shown in Fig. 6.5, at which the unit cell size is $400 \times 400\,\mu{\rm m}^2$, and the gaseous drift area is placed with a depth of 1.5 mm above the anode and cathode electrodes. The composition of the gas mixture in the simulation is Ar(90%) + Ethane(10%) with a pressure of 1 atm. In the Elmer software, the electric field around the μ-PIC structure constructed with the Gmsh is calculated where the dielectric constants of the gas, polyimide substrate, and copper electrode are 1, 3.5, 10^{10}, respectively, and the voltages of the cathode and anode electrode and electric field of the gas are 0 V, 560 V, 1.0 kV/cm, respectively, for the boundary condition. The Garfield++ includes the electric field data calculated by the Elmer, and simulate the physical process of electrons in the gas such as the drift and multiplication near the anode. In this simulation, the seed electrons are placed on the drift gas region of $400 \times 400\,\mu{\rm m}^2$ randomly at 1.0 mm above the electrodes. The penning effect coefficient of the Ar(90%) + Ethane(10%) gas is set to be 0.31 [115]. Byrne proposed that the distribution of the avalanche of the gaseous detector, or the electron multiplication factor A is modeled by a Polya distribution:

$$P(A) = \left(\frac{A(1+\theta)}{\bar{A}}\right)^{\theta} \exp\left(-\frac{A(1+\theta)}{\bar{A}}\right) \tag{6.4}$$

where $\bar{A}$ is the mean of A, or the so-called gas gain [116]. θ is a parameter concerned with the fraction of the electrons that have enough energy to ionize the gas, and $0 < \theta < 1$. Figure 6.7 shows the distribution of the electron multiplication factor of the single electron for the μ-PIC calculated by Garfield++. The distribution is fitted by the Polya distribution and θ of μ-PIC is approximately 0.65, which is independent on the anode voltage. Figure 6.8 shows the simulated induced current signal of the anode with $A = 1$ for the μ-PIC. There are more than one component in the signal, with a slow time constant of a few tens of nanoseconds and a long time constant more than 1 microsecond, and the half of the total current concentrates on a few hundreds of nanoseconds (See Appendix A).

In the TPC simulator, the following implementation is applied. For each seed electron, the electron multiplication factor is chosen by the Polya distribution (Eq. 6.4), and the template of μ-PIC current response is chosen at random from 2000 samples as shown in Fig. 6.8. Then, The current input for the electronics is calculated by convolving the seed electron distribution and the μ-PIC response.

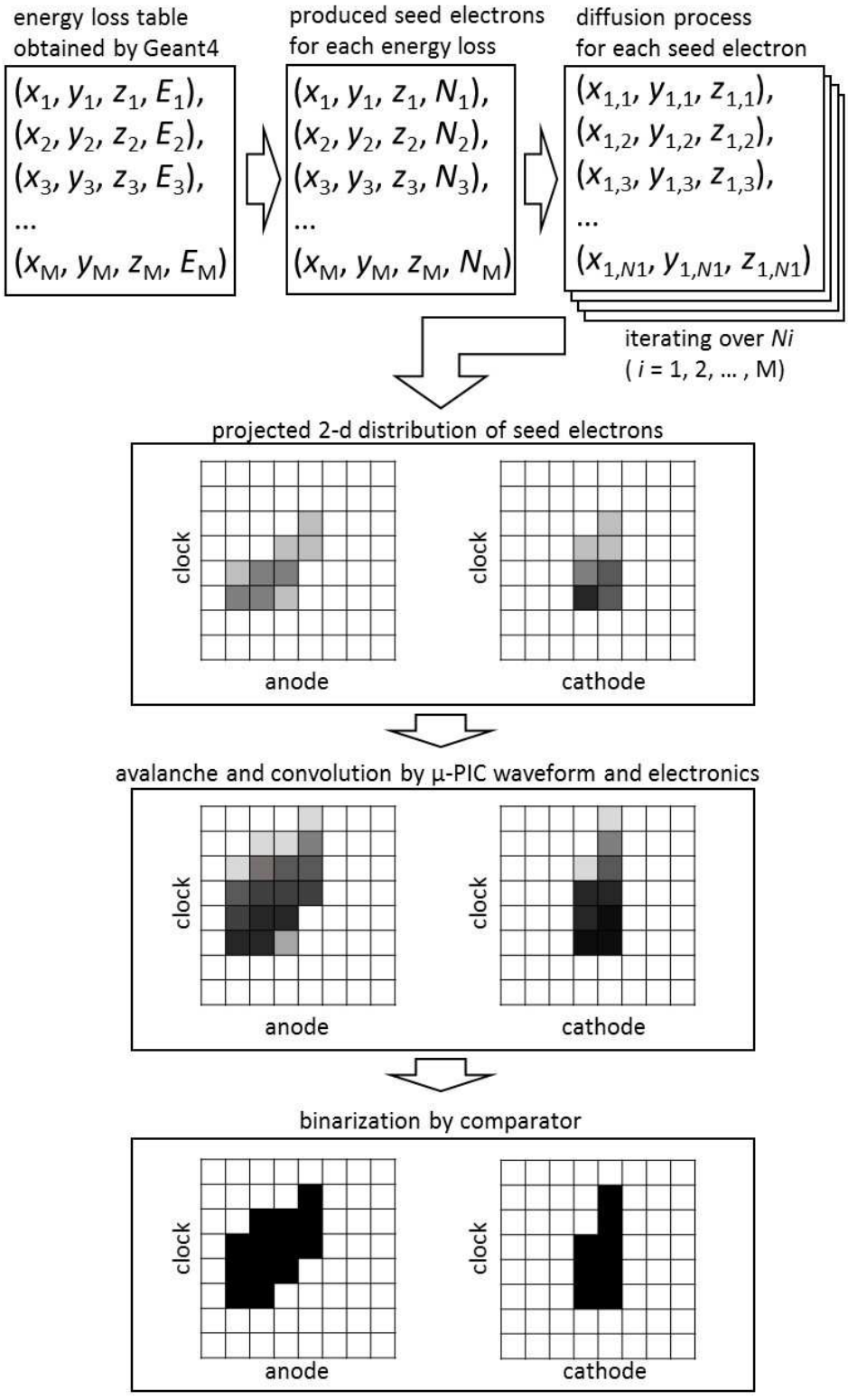

Fig. 6.3.— Schematic block diagram of TPC simulator.

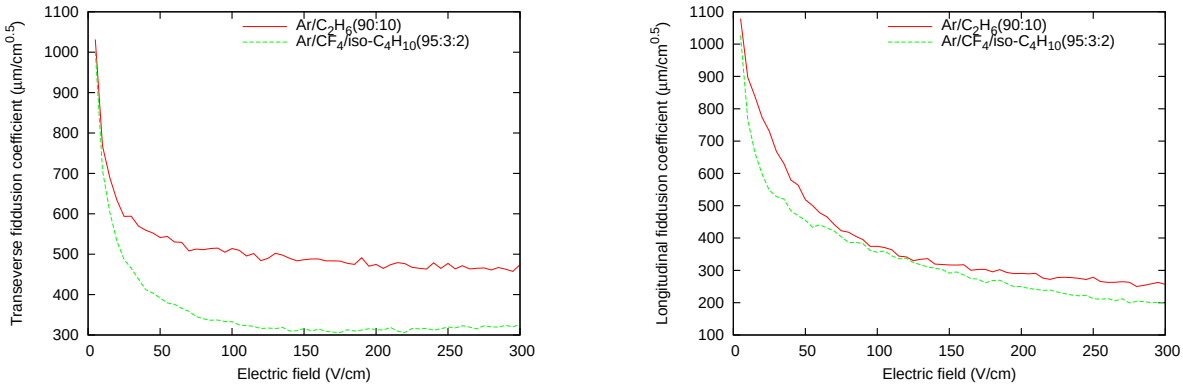

Fig. 6.4.— Simulated transverse (left) and longitudinal (right) diffusion coefficients by Magboltz [104]. The coefficients for the gas mixture for SMILE-II ETCC are shown with green broken lines, and as a reference, those of argon and ethane gas mixture are shown with red solid lines.

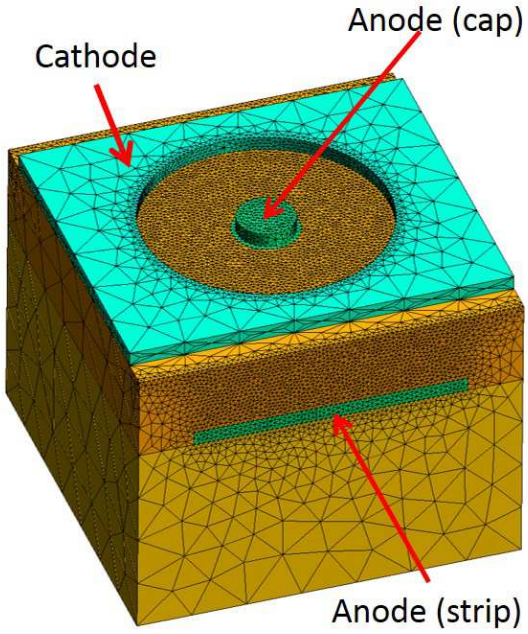

Fig. 6.5.— μ-PIC structure constructed by Gmsh with a finite element method [111].

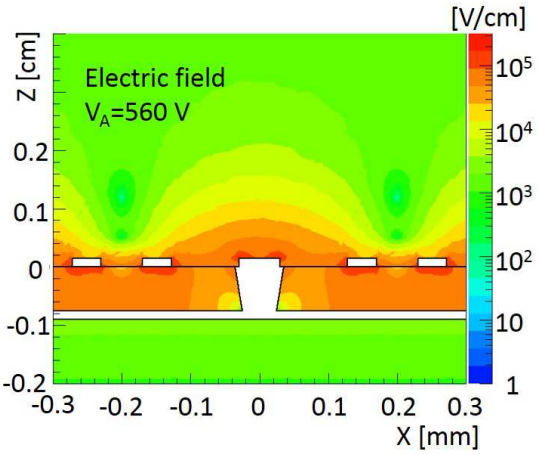

Fig. 6.6.— Simulated electric field around the μ-PIC by Elmer [111]. Applied voltages to the anode and cathode are 560 V and 0 V, and the electric field of the gas is 1.0 kV/cm.

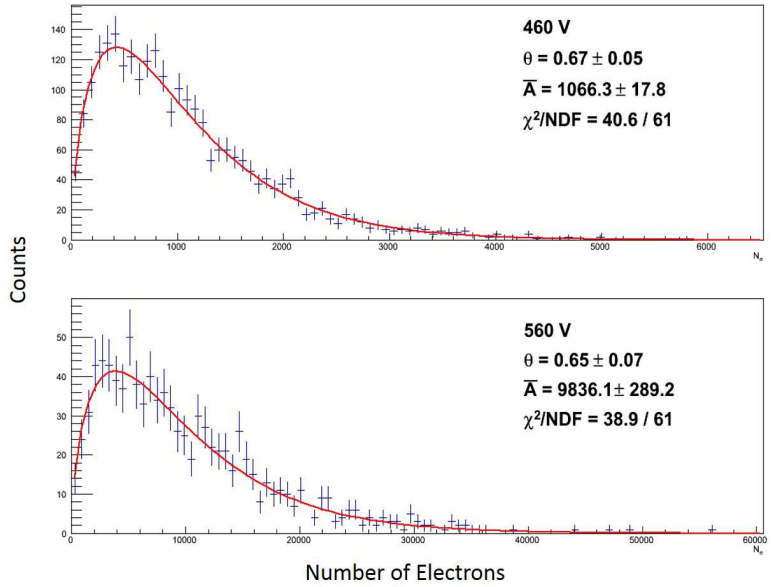

Fig. 6.7.— Distribution of electron multiplication factor of a single electron of the μ-PIC calculated by Garfield++ [111]. The distributions are fitted by a Polya distribution (solid line) and the estimated θ is approximately 0.65.

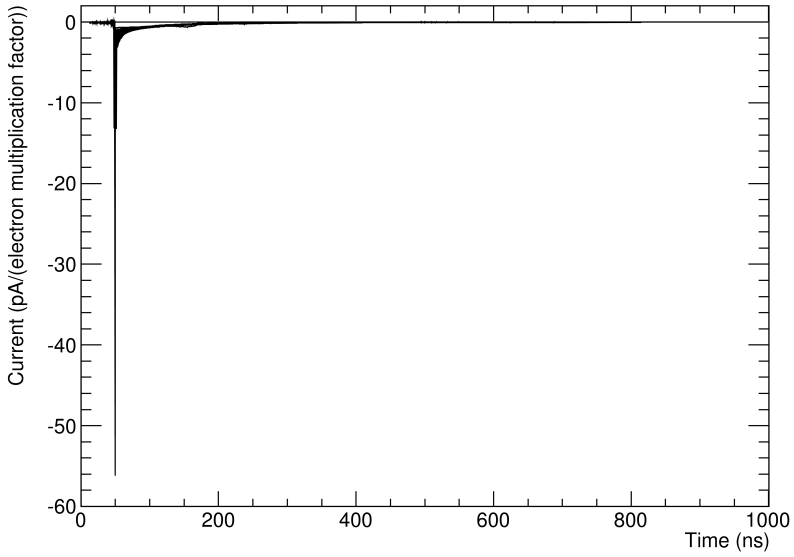

Fig. 6.8.— 2000 samples of μ-PIC current waveforms for the single seed electron. Each waveform is normalized by the electron multiplication factor.

6.2.3 Electronics Response

Since we replaced the ASD chip with the FE2009bal chip as the readout ASIC, we started to measure the waveform and gain for the input test pulse by the experiment. Analog summation-amplifier gain was measured by impulse charge input to the XCALIN (See Fig. 5.6) pins of the chips. The charge was fed by applying a step voltage to the AC coupling capacitor of 1 pF that is connected to XCALIN pins. The slope of the step voltage that results from the instrumental limit is 20 ns. Figure 6.9 shows the gain curve as a function of the input charge. The error bar represents the deviation of the outputs of 8 chips. The good gain linearity was obtained between -0.5 pC and $+0.5$ pC. The slope derived by fitting in the range between -0.5 pC and $+0.5$ pC is 770 mV/fC and then the reduced χ^2 is 1.6, which is fairly acceptable. The gain slope is moderately shallower as the more input charge is given.

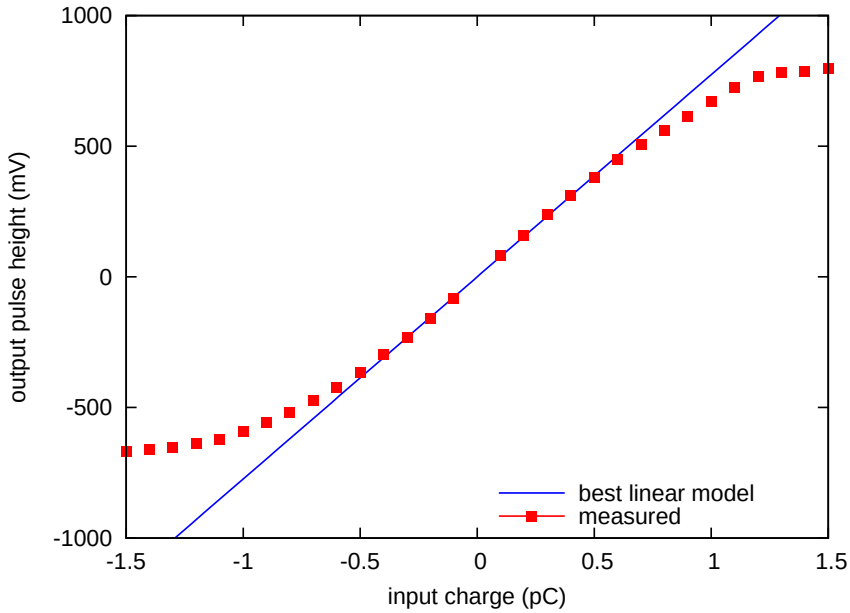

Fig. 6.9.— Gain linearity of analog summation-amplifier of FE2009bal chip. The best fit line is estimated within the range between -0.5 pC and $+0.5$ pC.

To obtain the 'typical' waveform of XAOUT (See Fig. 5.6) of the FE2009bal chip, we sampled waveforms for various impulse charge inputs and fitted them. To avoid the distorted waveforms due to over-input charge, the waveforms with inputs of ± 0.1, ± 0.2, ± 0.3, ± 0.4, and ± 0.5 pC are chosen. For each input charge eight waveforms derived by different eight chips are sampled by an oscilloscope with a sampling rate of 1.25 GHz. Figure 6.10 shows the overlaid 80 samples of waveforms (gray: positive charge inputs, red: negative) of which

the pulse heights are normalized to be 1 and the peak times are shifted to be 0. We fitted the average of the waveforms of the all 80 samples in the time range between -50 ns and 150 ns by the function (hereafter the CR-RC model) that describes the outputs of a shaping amplifier with the same integral and differential time constants:

$$V_{out} = \begin{cases} V_0(\frac{t-t_0}{\tau})\exp\left[-\frac{t-t_0}{\tau}\right] & (t \geq t_0) \\ 0 & (t < t_0) \end{cases} \tag{6.5}$$

where V_0 is the peak pulse height and t_0 and τ are the input time and the time constant of the shaper, respectively. The best estimate of the time constant is 2.0×10 ns and the corresponding χ^2/NDF is well acceptable of 252/249.

The TOT response of the FE2009bal for impulsive input is investigated by the both experiment and simulation. The experimental data was taken using an FE2009bal readout board by using the same impulse charge as the previous paragraph. The simulation data were obtained by convolving the input charge with duration of 20 ns and the two types of response models. The one is the function of Eq. 6.5 (CR-RC model) and the other is the average of waveforms sampled by the oscilloscope (hereafter the template model). The template model consists of 40 sets of the averages of waveforms and gain tables for the inputs of $\pm 0.1, \cdots, \pm 2.0$ pC as shown in Fig. 6.11 and 6.12. The gain in the both response functions is set to be the linear interpolation of the gain curve of Fig. 6.9 with a charge of each time bin. We took the time width of each bin 0.5 ns that is smaller than the clock of TOT, 10 ns. Figure 6.13, 6.14, 6.15, and 6.16 shows the TOT response for different $V_{\rm th}$. We note that the TOT responses of the positive and negative input charge behaves differently even if the input charge was small enough where the gain curve has a good linearity in the both positive and negative input charge. It indicates the fact that there is another intrinsic response difference between negative and positive input charge within the chip. The simulated TOT response using the CR-RC model (as shown in Fig. 6.13 and 6.14) of the cathode agrees well with the measured one within a few clocks, while the model of the anode fairly traces the measured ones and the maximum relative error of the CR-RC model is about 40% for a threshold of 300 mV. That discrepancy for the anode response is, however, not well reduced by applying the template model as shown in Fig. 6.15 and 6.16 of which the maximum relative error is still 40%, implying the distortion of the response waveform in the chips cannot be estimated directly by the measurements of the XAOUT outputs. Therefore we hereafter adopt the CR-RC model from the viewpoint of the simpleness of the model description, because the template model does not improve the impulsive TOT response. We note that, in the practical case, the input charge for the MIP event in the TPC, where the filling gas is 1-atm argon gas and the gas gain is 20000, is about $30 - 40$ fC, and this region is less discrepant compared to the input charge higher than 100 fC.

In the TPC simulator, the waveform for each strip is derived by the convolution of the

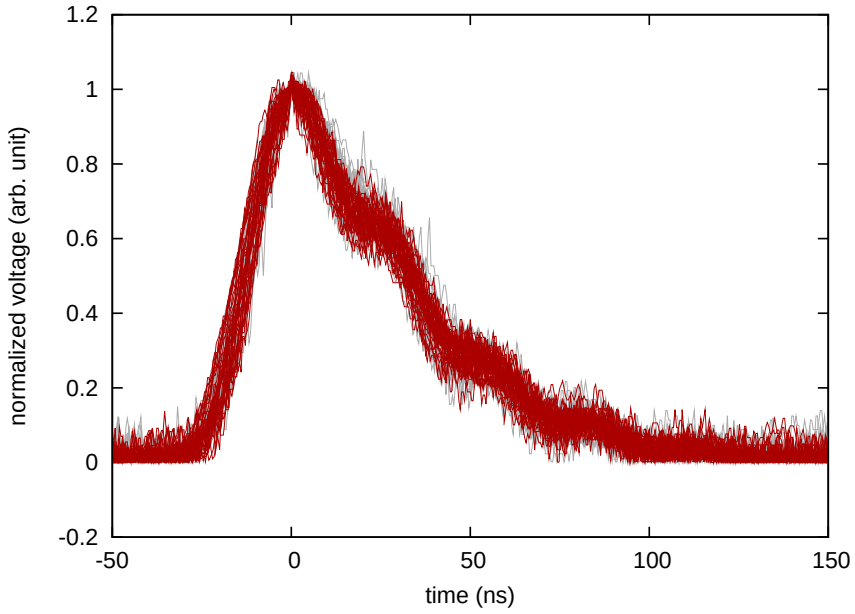

Fig. 6.10.— superpositions of waveforms of FE2009bal analog output 'XAOUT' with inputs of ±0.1, ±0.2, ±0.3, ±0.4, and ±0.5 pC. positive and negative charge inputs are shown in gray and red solid lines, respectively.

current input and the response of the electronics (as described Eq. 6.5). In practical case, the μ-PIC response is considered with a duration of 2000 ns and the waveforms are directly derived by the convolution of the seed electron distribution and the response of the μ-PIC and electronics response that is calculated in advance as shown in Fig. B.1. Those derived waveforms are compared with the voltage threshold $V_{\rm th}/A_{\rm comp}$ and binarized, where $V_{\rm th}$ is the threshold voltage applied toward the ASIC and $A_{\rm comp} = 150$ is the factor of the difference of the gains between 'XAOUT' and the signal that is connected to the comparator in the ASIC.

6.2.4 Validity of TPC simulator

A reproducibility of the TPC simulator is studied from the two points of view: the drift velocity and the number of the ionized electron.

Practically, the drift velocity of the electrons in the TPC is measured by calculating the width of the integral clock histogram as mentioned in the section 5.5. On the other hand, in the simulation the drift velocity is a given parameter. Figure 6.17 shows a differential hit distribution along to the z-axis, obtained using the TPC simulator by the incident particles of

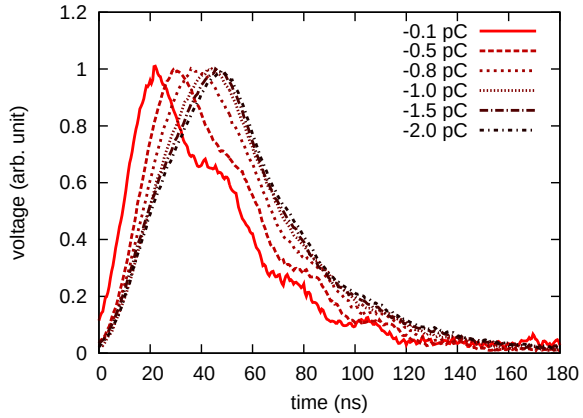

Fig. 6.11.— Normalized typical waveforms for anode with different input charges.

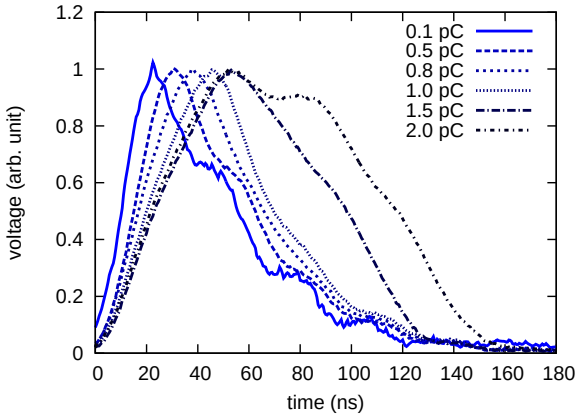

Fig. 6.12.— Normalized typical waveforms for cathode with different input charges.

Compton-recoil electrons with an initial position at random in the TPC, and an energy and angular distributions according to the Klein-Nishina equations 3.13 and 3.14 for the incident gamma-ray energy of 662 keV. The positive and negative peaks in the differential distribution represent the lower and upper borders of the drift region, respectively. The drift velocity calculated by the time-lag between the two peaks of the differential distribution is 6.58 cm/μs, while the given drift velocity with which the hit data are produced is 6.645 cm/μs, and thus the error of reproducibility in the calculation along to the drift direction is approximately 1%.

The procedure of the ionization in the TPC was introduced in 6.2.1. Though the definition of the W-value is the mean energy to create one ion-electron pair, the number of the ion-electron pair is calculated for each bin, and therefore the small energy losses less than W-value in the bins may not contribute to the ionization effectively. Figure 6.18 shows the energy loss consistency between the actual energy loss in the active volume of the TPC and the reconstructed one by the counting the number of the ionized electrons produced in the TPC. One can see a linear correlation with the energy range below 200 keV. The fitted relation between the reconstructed energy E' and the actual energy E is $E = 1.01 \times E' - 0.21 \pm 0.01$, implying that the almost all of the total energy loss is actually used to create the ion-electron pair in the simulation.

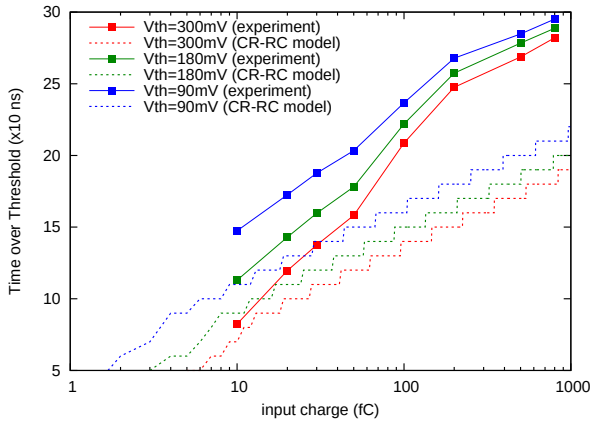

Fig. 6.13.— TOT response simulation for impulsive negative input charge with CR-RC model.

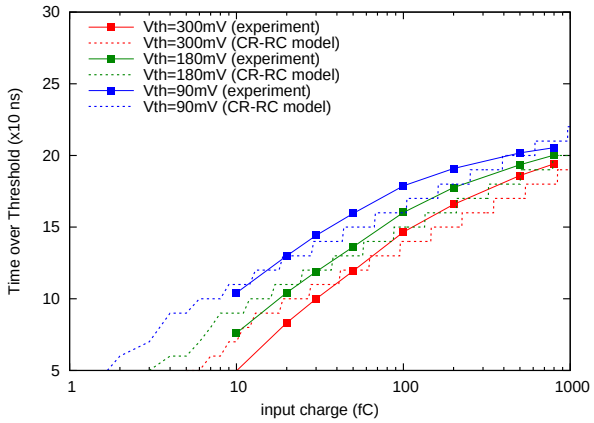

Fig. 6.14.— TOT response simulation for impulsive positive input charge with CR-RC model.

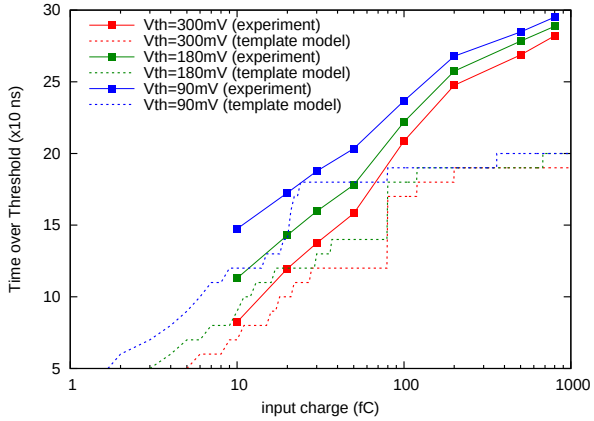

Fig. 6.15.— TOT response simulation for impulsive negative input charge with the template model.

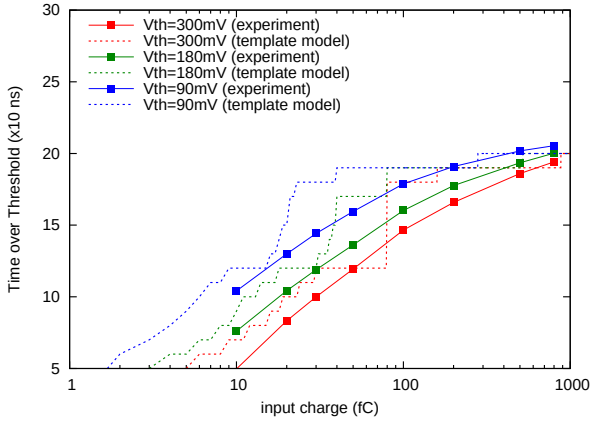

Fig. 6.16.— TOT response simulation for impulsive positive input charge with the template model.

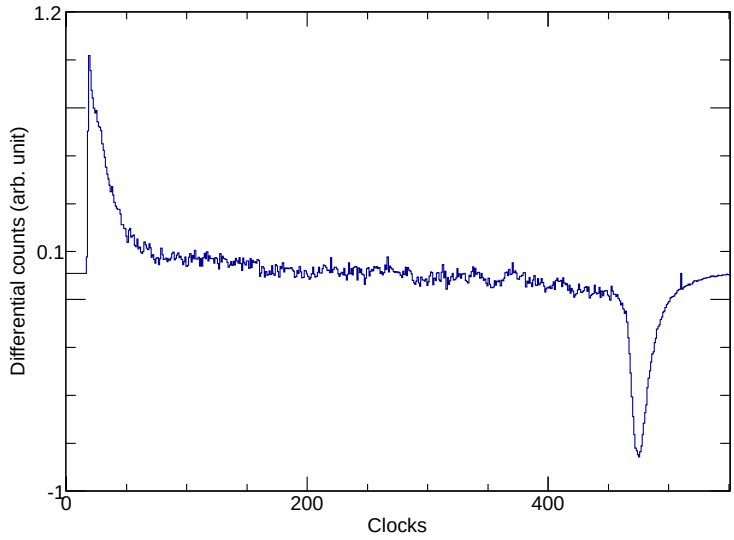

Fig. 6.17.— Differential hit distribution along to the z-axis derived by the TPC simulator. The positive and negative peaks in the distribution represent the lower and upper borders of the drift region.

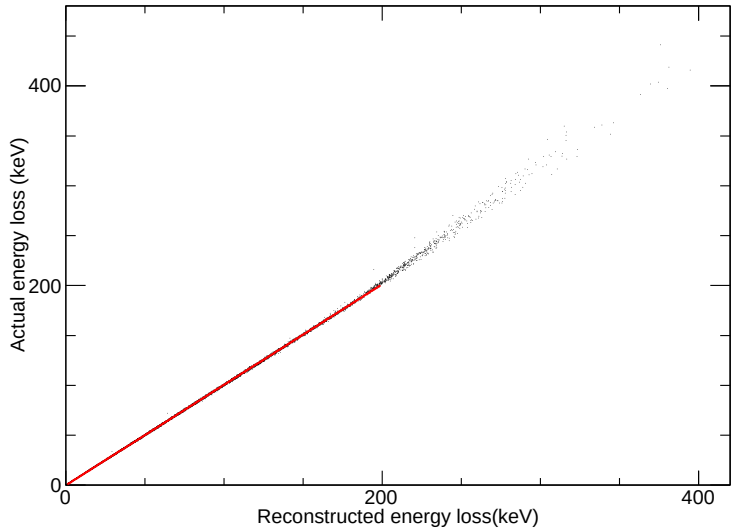

Fig. 6.18.— Energy loss consistency between the actual energy loss in the TPC and the reconstructed one by the counting the number of the carriers created in the active volume. A linear-fit line within the energy range below 200 keV is drawn with a red solid line.

6.3 TOT of Charged Particles

In the previous section, the TPC simulating model was introduced and then we can obtain 2-dimensional track of arbitrary kinds of particles by the simulation. Figure 6.19 shows examples of electron-like events measured by the real SMILE-II TPC (upper 6 images), and examples of simulated 2-d tracks of Compton-recoil electrons produced by the incident gamma-ray with an energy of 662 keV (lower 6 images). In both images, one can see that there are some long tails in the TOT, which are the signs of much energy loss, and appearances of them are quite similar.

To confirm the validity of the TOT response of the TPC simulator quantitatively, we compared the TOT responses for MIPs obtained in the experiment and simulation. In order to extract MIP-like events from the experimental data, we used background data of the SMILE-II/ETCC obtained in the calibration run. The detail is discussed in Appendix C. On the other hand, the TOT simulation was calculated with the following conditions. As the primary particles for the Geant4, we chose muons with a kinetic energy of 10 GeV, and the direction distribution where the projected angle distribution has a normal distribution with a deviation of 8.8 degrees so as to agree to those in the experiment. For the TPC condition, the gas gain, drift velocity, W-value, Fano factor, transverse and longitude diffusion constants, and $V_{\rm th}$ for the signals from anode and cathode are 19330, 6.65 cm/μm, 26 eV, 0.17, 313 μm/cm$^{0.5}$ and 269 μm/cm$^{0.5}$, 315 mV and 360 mV, respectively. The W-value and Fano factor are determined to be the literature values for argon gas, and the gas gain and drift velocity are set to be the values measured by the experiment. The diffusion constants are the calculated value by the Magboltz. As the emulation of the TPC electronics, the CR-RC model is used as mentioned in the previous section. Figure 6.20 shows the simulated TOT distribution (blue dashed line) overlaid with a measured one (red solid line). One can see the simulated TOT distribution well traces the measured one around the most probable value at 10 clocks and has a slight discrepancy at 20 clocks. The null hypothesis of the measured and simulated distributions are different is tested by the Kolmogorov-Smirnov test within the data of the TOT below 56, where the relative probable value is higher than 1%, and the p-value is calculated to be 0.098, so that we cannot exclude the null hypothesis with a significance level of 5%. Thus we conclude the TOT response for the MIP-like events are well explained by the simulation.

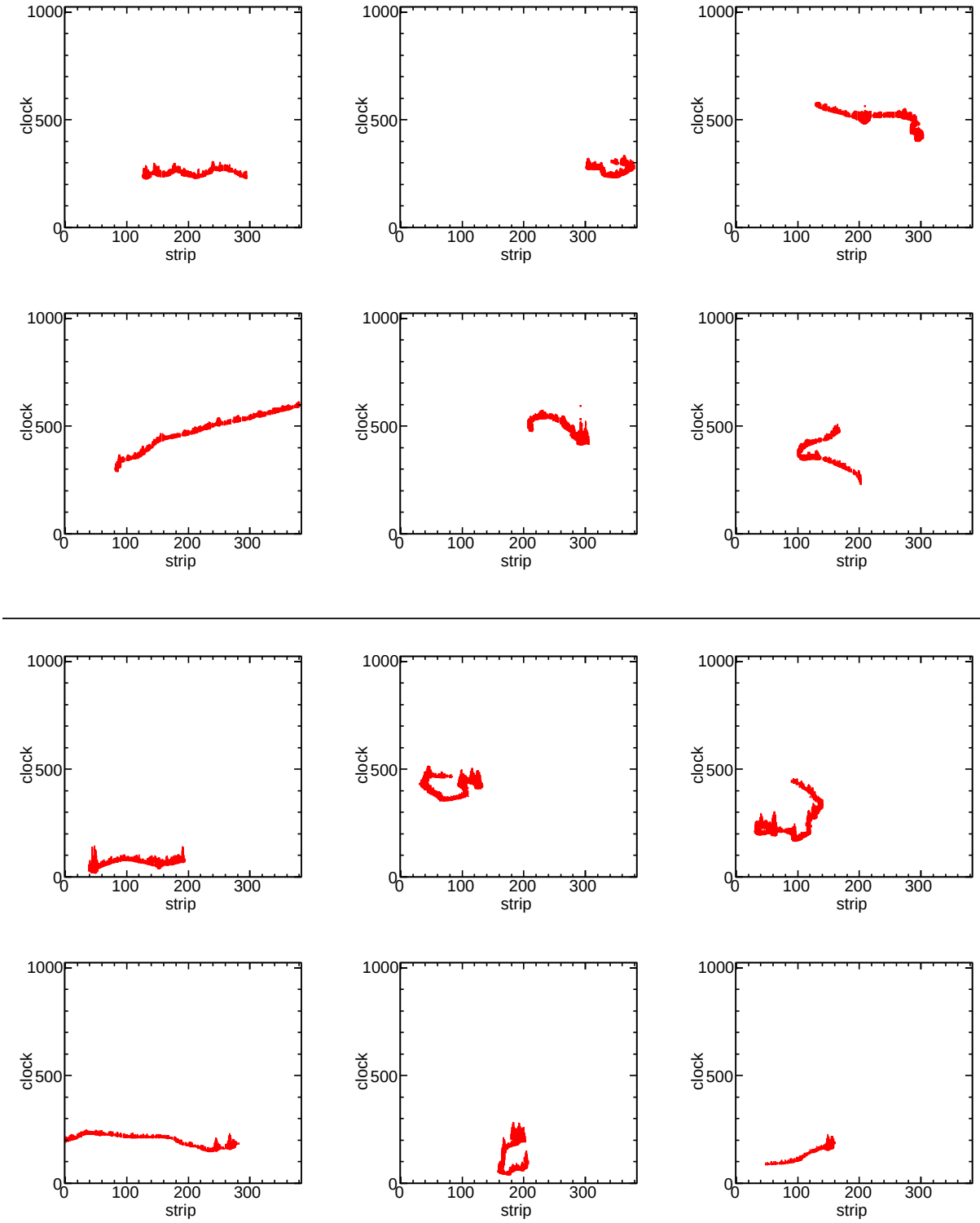

Fig. 6.19.— Examples of 2-d projected tracks of electron-like events measured by SMILE-II TPC (upper 6 images) and examples obtained by the TPC simulator (lower 6 images).

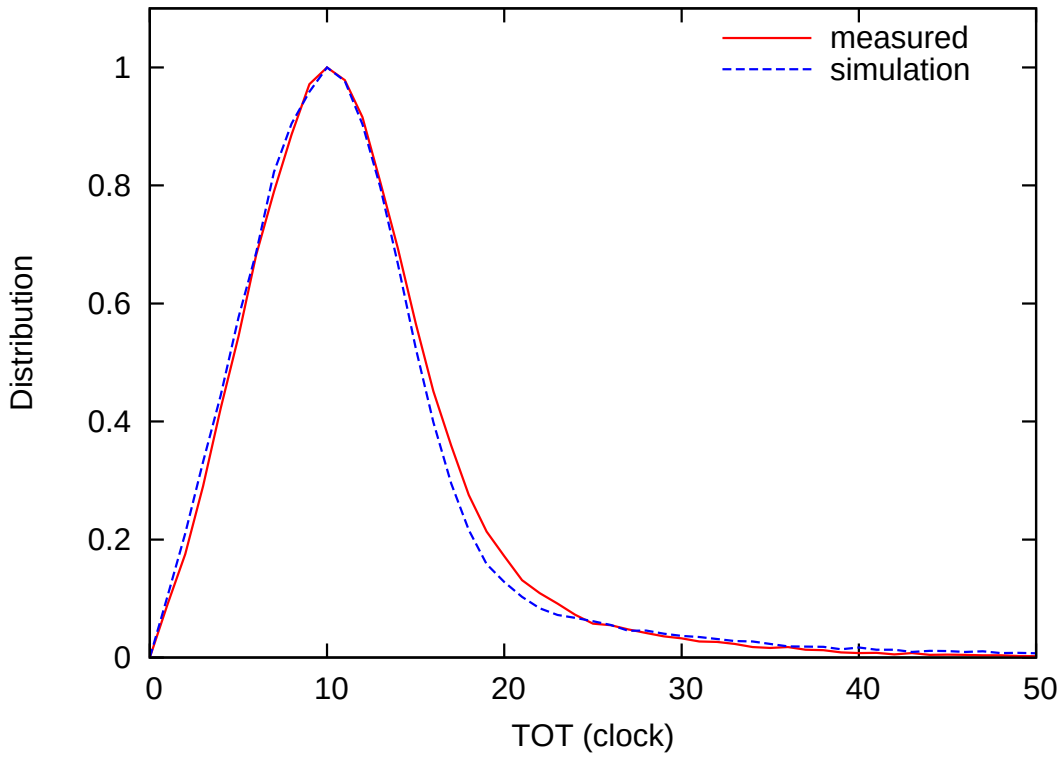

Fig. 6.20.— The distributions of the TOT of the tracks for MIP-like events obtained by measured (red solid line) and simulation (blue dashed line). The measured data is the same as the data of PSA and χ^2 cuts in the Figure C.3 (magenta points).

6.4 Particle identification by energy loss rate

Using the TPC simulator, the background rejection ability and the Compton-scattering event inefficiency for the energy loss rate cut in the plane of the energy loss and the track range in the TPC, or the dE/dX cut, are investigated.

The test data set for Compton scattering events is generated as follows. The parameters for the TPC simulator are the same as those in the TOT response study for experimental data. The initial particles are electrons of which energy and direction distribution follow the Klein-Nishina equation for an incident 662-keV gamma-rays from a line-of-sight. The Compton scattering point is chose at random in the TPC. Figure 6.21 shows the energy loss rate of the electrons on the plane of the energy loss versus the track range. Like the histograms obtained by experiments such as Fig. 5.17, there are two components in the histograms. In the lower rows in Fig. 6.21, the fully-contained electrons are plotted in the black dot and the electrons that protrude the active volume of the TPC are in the magenta dot. One can clearly see the two components in the energy-range plane resulting from the presence or absence of the protrusion of the track. On the right bottom in the Fig. 6.21, the boundary of the energy loss rate cut used for the measurement data and the expected line of the range-energy relation are drawn with three red solid lines. One can see the scatter plot of the black dots fairly traces the numerical approximation, and limited between the two energy loss cut lines. The selection efficiency of the fully-contained electrons and the (mis)selection efficiency of the escaping electrons are calculated using the energy loss rate cut condition with which the parameters are the same as those applied to the measurement. Then the selection efficiency of the fully-contained electrons and the (mis)selection efficiency of the escaping electrons for the incident gamma-ray energy of 662 keV are approximately 0.84 and 0.24, respectively.

The drop of the selection efficiency of fully-contained electrons and the increase of the (mis)selection efficiency of the escaping electrons result from the degeneration of the both events of the lower energy below 40 keV and 20 keV, respectively. In the practical case, however, the events are sifted not only by the energy loss rate cut but also by the fiducial volume cut. The (mis)selection efficiency of escaping electron events by the combination of the both cuts is less than 0.3% through an gamma-ray energy range of 150 - 1500 keV, which is acceptable. This result indicates that the combination of the energy loss rate cut and the fiducial volume cut is essential to avoid the contamination of the signal events by accepting the events of escaping electrons with low energy loss in the TPC.

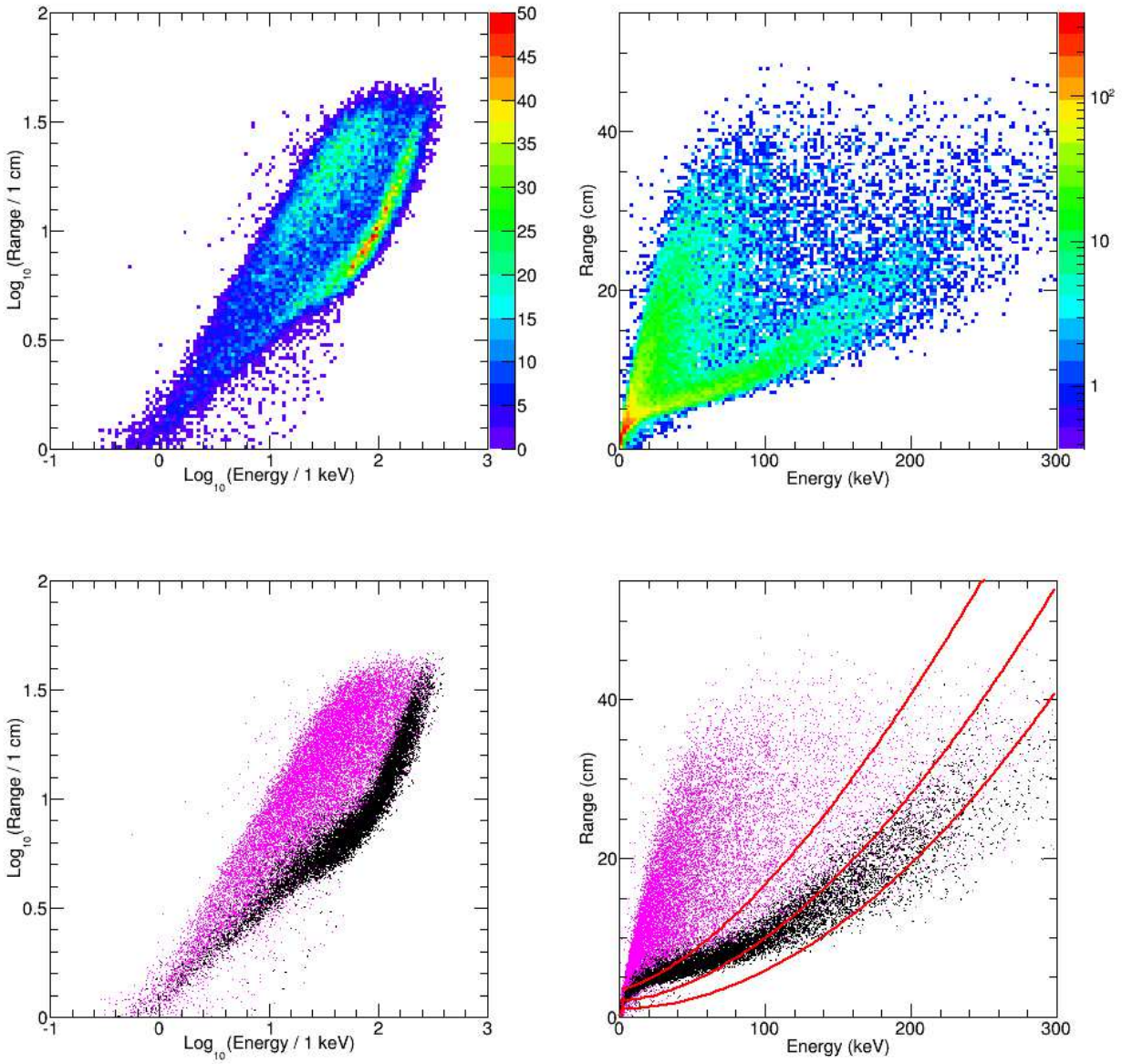

Fig. 6.21.— (Left top) Histogram of energy loss rate of the electrons in the plane of the energy loss versus the range in the double-logarithmic scale. The color represents the intensity of the number of the events in arbitrary unit. (Right top) the same as the histogram on the left top but in the linear scale. (Left bottom) the same as the left top but described with a scatter plot, representing the fully-contained electrons (black dot) and the electrons escaping to the outside of the TPC (magenta dot). (Right bottom) the same as the left bottom but in the linear scale. The expected line of the energy-range relation and the energy loss rate cut used for the measured data are also shown with the three red solid lines.

6.5 Detection efficiency of ETCC

Combination of the matter interaction model and the detector model reveals the contribution of each component to the detection efficiency of the ETCC. Figure 6.22 shows the energy dependence of the fraction of the physics process probability and the event selection efficiency of the SMILE-II ETCC.

First of all, when Compton scattering in the TPC, most of the events occur photoabsorption in the PSA, as shown with (a) and (b) in the Figure 6.22, indicating that the covering fraction of PSA is generally reasonable and the both bottom and side PSAs contribute effectively as shown in (c) and (d). One can see that at high energy range not a few recoil electrons escape from the TPC active volume and therefore there is a significant fraction drop for the condition of 'fully-contained recoil electron' at high energy range, as shown in (e) compared to (b).

As the detector event selection efficiency, the energy thresholds of the TPC and the PSA, and the energy loss rate cut efficiency do not drop the efficiency significantly for high energy more than about 300 keV, but worsen it for low energy less than 200 keV, as shown in (f), (g), and (h) compared to (e). The detection efficiency for RI is derived by adopting the total energy cut to the efficiency (h), as drawn with (j). Basically, the drop at the total energy cut results from the undesired interaction of the gamma-ray with the passive matter such as the vessel of the TPC and the PSA readout modules. The line (i) shows the events for which the Compton-scattered gamma-rays do not interact with the passive matter before they are absorbed in the PSA. One can see the fraction levels of (i) and (j) are almost same level, and thus the total energy cut actually reflects the matter interaction of the scattered gamma rays.

The measured detection efficiency obtained by irradiating RI sources are shown in points (k), which are the same data as those introduced in Section 5.6. The measured effective area is systematically higher than that of simulation by $\sim 10\%$ for energy above 300 keV, but lower by 26% at 166 keV. The reason of these errors originating in the experiment was already discussed in Section 5.6. Here we comment about a possibility of the error in the simulation. Considering the major factor contributing to the efficiency for each energy range, the uncertainty of the mass model of TPC vessel will directly affect the detection efficiency for higher energy range. In fact, the simplified vessel model would be heavier than the real one. On the other hand, the measured efficiencies may be contaminated by the chance coincidence events, as mentioned in Section 5.6. To reject such random coincidence events, the Compton kinematics test, which was also used in SMILE-I, will work effectively. To adopt this test with optimized ways, further studies with both the measurement and the simulation are required for keeping a considerable SNR.

Looking down at the whole fraction lines, one can conclude that the predominant factors contributing to the detection efficiency are electron escaping and gamma-ray scattering through the TPC. We note that the both factors result from the physics process rather than detector response. For low energy below 200 keV, the contribution of the detector threshold of the PSA and the energy loss rate cut efficiency become higher. Therefore, to improve the effective area of the ETCC, several points are suggested. First, one should save the electron escaping events to measure the energy of the escaping electron. One of the solutions to realize this is to put the electron absorber such as plastic scintillator near the boundary of the active volume of the TPC. The effect of this improvement is investigated in [117]. Next, One should reduce the mass of the TPC vessel as much as possible, or put the absorber crystal in the TPC vessel. Long radiation length of the crystal also contributes to the reduction of the interaction with the readout circuits on the back side of the PSA. If one focuses on the lower energy range below 200 keV, a lower energy threshold of the PSA and refinement of the TPC position resolution are also important factors. Undoubtedly, the increase of the Compton scattering probability is a crucial factor for the whole energy range.

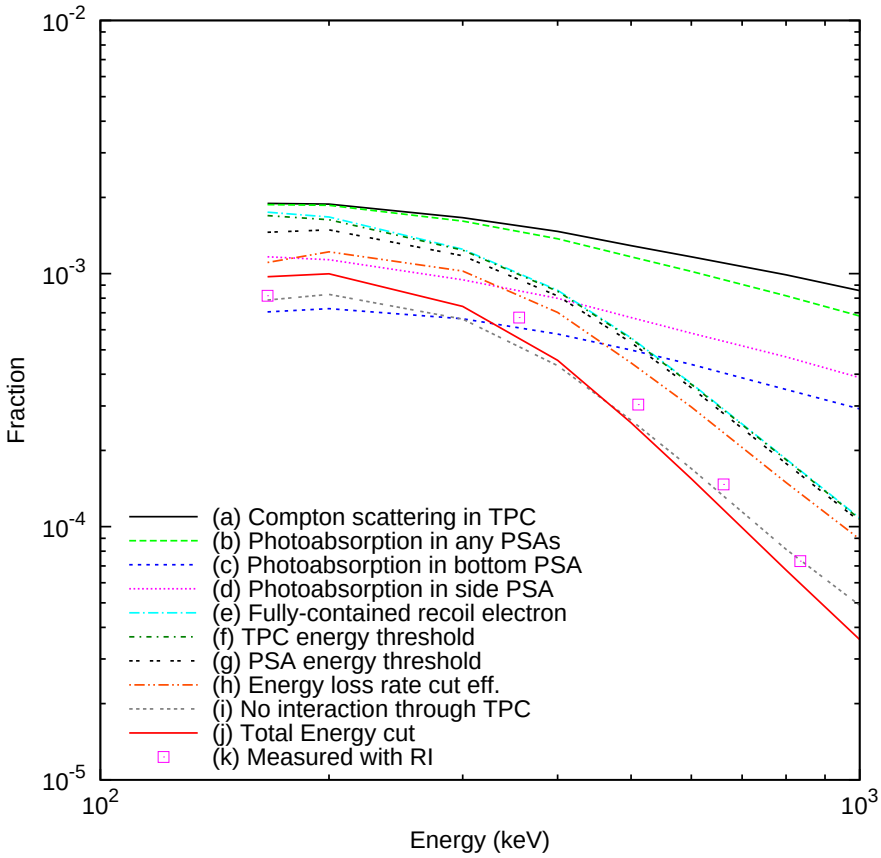

Fig. 6.22.— Fractions of physics process probability and event selection efficiency of the SMILE-II ETCC: (a) Compton scattering probability in the TPC, (b) Fraction where the events satisfies the condition (a) and photoabsorption occurs in any PSAs, (c) Fraction where the events satisfies the condition (a) and photoabsorption occurs in bottom PSAs, (d) Fraction where the events satisfies the condition (a) and photoabsorption occurs in side PSAs, (e) Fraction where the events satisfies the condition (a) and the recoil electron stopped in the TPC, (f) Fraction where the events satisfies the condition (e) and the energy loss in the TPC exceeds the energy threshold of the TPC, (g) Fraction where the events satisfies the condition (f) and the energy loss in the PSA exceeds the energy threshold of the PSA, (h) Fraction where the events satisfies the condition (g) and the energy loss rate cut, (i) Fraction where the events satisfies the condition (h) and no scatterings occur out of the active volume of the detector after Compton scattering in the TPC and before photoabsorption in the PSA, (j) Fraction where the events satisfies the condition (h) and the total energy loss cut, and (k) Measured detection efficiency obtained by irradiating RI sources.

Chapter 7

Future observations

In Chapter 6, the detection efficiencies obtained by the simulation show good coincidence with the experimental data. Therefore, one can estimate the significance for the detection of any celestial objects using the effective area and the background rejection ability derived by the detector simulation. In this chapter, we discuss the prospect for the future observations using the ETCC aboard a balloon/satellite.

7.1 Expected observation with SMILE-II

In this section, a numerical calculation of the significance of the observation of the bright point sources with the SMILE-II/ETCC is discussed, because the success criteria of the SMILE-II flight is that the ETCC detects any point sources at balloon altitudes with a significance level of $> 5\sigma$. The condition of the SMILE-II flight ETCC discussed in Chapter 5.6 is used.

In terms of the angular resolution, the SPD resolution was determined by the uncertainty resulting from the reconstruction method rather than the multiple scattering effect of the recoil electron. A recent study on analysis of the three-dimensional track obtained by the TPC, has realized better angular resolution of the SPD, by applying the correction of the time walk of each hit pixel using the TOT [90]. Applying this method, the SPD reaches 100 degrees (FWHM), with which an ARM of 5 degrees yields a radius of the PSF of 20 degrees. If the SPD is achieved to be 50 degrees by the further improvement of track data analysis, the corresponding PSF is improved to be 10 degrees. In this section, we suppose the two cases of the PSF, 10 degrees and 20 degrees.

The significance of the excess source counts are generally obtained as follows,

$$\sigma = N_{\rm src}/\sqrt{N_{\rm src} + N_{\rm bgd}}, \tag{7.1}$$

where $N_{\rm src}$ and $N_{\rm bgd}$ are the number of the signal and background events that are counted within a source region.

The numbers of the signal events $N_{\rm src}$ is calculated by

$$N_{\rm src} = \int_{E_1}^{E_2} dE\, \alpha(\Delta\Omega)\, F_{\rm src}(E)\, A_{\rm eff}(E)\, \eta(E)\, T, \tag{7.2}$$

where $\alpha(\Delta\Omega)$ is the fraction ratio of the signals that come within the solid angle of $\Delta\Omega$, and E_1, E_2, $F_{\rm src}(E)$, $A_{\rm eff}(E)$, $\eta(E)$, and T are the lower limit of the energy, the upper limit of the energy, the source flux, the effective area, the transparency of the atmosphere, and the observation time, respectively. For the balloon experiment, the attenuation effect $(1-\eta)$ is not negligible and calculated considering the zenith angle. T is determined by the time during the zenith angle of the point source within 45 degrees.

As the background events, in this section, we consider not only the cosmic diffuse gamma rays and atmospheric gamma rays, which are taken into account for in Section 5.1, but also the Galactic diffuse gamma rays. Moreover, we also estimate the event rates by the instrumental gamma rays and neutrons produced by the interaction between the primary/secondary cosmic rays and the equipment. The total number of the background events are described as

$$N_{\rm bgd} = \int_{E_1}^{E_2} dE\, \Delta\Omega(I_{\rm atm}(E) + I_{\rm int}(E) + \eta(E)(I_{\rm extragal}(E) + I_{\rm gal}(E)))\, A_{\rm eff}(E)\, T, \tag{7.3}$$

where $I_{\rm atm}(E)$, $I_{\rm int}(E)$, $I_{\rm extragal}(E)$, and $I_{\rm gal}(E)$ are the intensities of the atmospheric, instrumental, extragalactic, and Galactic gamma rays, respectively. Here, the gamma rays which come downward from the top of the instrument are taken into account for the intrinsic gamma-ray intensity $I_{\rm int}(E)$. On the other hand, the intrinsic gamma rays coming from the bottom of the instrument and random coincidence events are assumed to be rejected by the Compton kinematics test and the constraint on the reconstructed incident direction of the events, as discussed by Tanimori *et al.* [90].

In the SMILE-II balloon experiment, a day-flight is planned on the middle latitude. As a practical location of a balloon launching, Fort Sumner in the U.S. and Alice Springs in Australia are candidates. Let us assume that the location of the launch site is chose to be Fort Sumner, and the altitude reaches 40 km during the flight. Then, as promising candidates of the bright sources in the sub-MeV band, Crab nebula, Cyg X-1, and GRO J0442+32 are chosen, for the fluxes and altitudes of these sources are shown in Fig. 7.1 [94, 118, 119].

First, the diffuse gamma-ray continuum radiation at MeV energies from the Galactic center and plane is thought to mainly originate in two process involving cosmic-ray electrons:

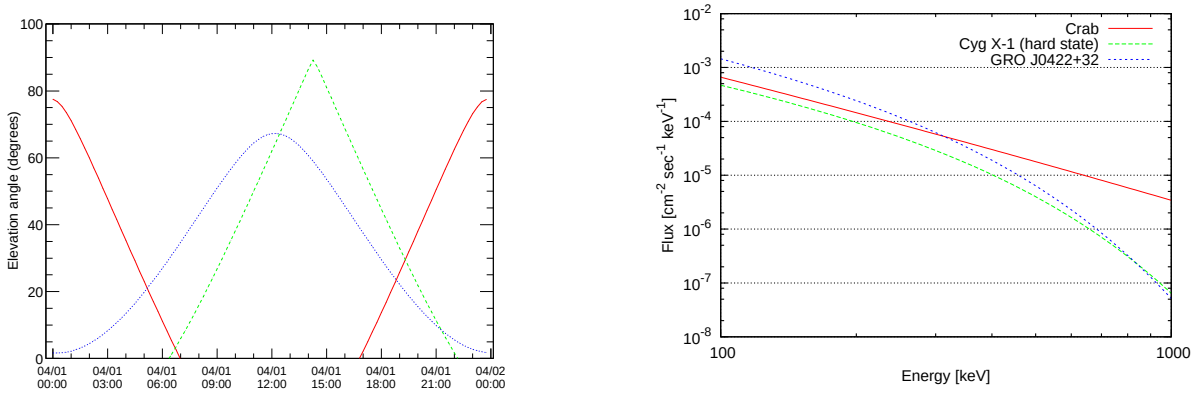

Fig. 7.1.— (Left) Elevations angle of Crab nebula (red solid line), Cyg X-1 (green dashed line), and GRO J0442+32 (blue dotted line) at Fort Sumner, on Apr. 1, 2018. (Right) Differential photon fluxes of the bright sources in the sub-MeV region [94, 118, 119].

the inverse Compton scattering of cosmic microwave background or starlight photons, and bremsstrahlung with interstellar gas (Kniffen and Fichtel 1982), where the latter predominates over the former in 1-10 MeV range (Harris *et al.*). Therefore, we assume Galactic diffuse gamma rays originate in cosmic-ray interactions with interstellar gas, and thus use the relationship, $I_{\rm gal} = \varepsilon N_{\rm H}$ where $I_{\rm gal}$ is the gamma-ray intensity (cm^{-2} sec^{-1} sr^{-1}), ε the gamma-ray emissivity per H atom, $N_{\rm H}$ the hydrogen column density. We assumed $\varepsilon \propto E^{\eta}$, where the normalization and index η are determined to be $0.01\,{\rm cm^{-2}sec^{-1}sr^{-1}MeV^{-1}}$ for 1 MeV with the averaged $N_{\rm H}$ in the inner Galaxy ($|l| < 30^{\circ}$ and $|b| < 5^{\circ}$), and -2, respectively, in reference to the observation data of OSSE [120, 121]. $N_{\rm H}$ was calculated with one of the *Swift* data analysis tools, NHtot, where the 21-cm maps of Kalberla *et al.* are used to determine the $N_{\rm HI}$ and the dust map of Schlegel *et al.* for $N_{\rm H_2}$ [122, 123, 124].

Second, at high altitudes, primary cosmic rays hit the equipment and locally produce secondary particles such as neutrons, gamma rays, electrons, positrons, and other charged particles. Secondary cosmic electrons are major sources of the tertiary gamma rays due to the Bremsstrahlung process of those electrons in the instruments. The tertiary gamma rays coming downward from the top of the instrument $I_{\gamma,{\rm down}}$ are intrinsic backgrounds for the real instrument, and therefore they must been taken into account for the estimation of the gamma-ray flux from the target. Neutrons would be prominent non-gamma-ray background for the classical Compton camera because the elastic scattering between the neutron and the nucleus in the scatterer behaves as if it were a Compton event. As shown from this, the ETCC can reject such neutron elastic scattering events using energy loss rate cut. To estimate the amount of the cosmic-ray induced particles, a Geant4 simulation was performed based on the mass model of the FM system. Figure 7.2 shows a visualized mass model of the FM system. The balloon gondola and the battery are not taken into account because they

will be placed in another vessel and distant from the vessel which contains the FM system and thus the effect on the secondary particle production is thought to be negligible. On the other hand, the components close to the detectors and detector themselves are carefully treated so that the mass of each component corresponds with the measured one. Since it is difficult to estimate the precise elemental composition of the electronics for each device, we compensate the mass at the location of each device with pure aluminum of a reduced density so as to be the same mass as the measured one. The total mass of the system on the model is 220 kg, which is consistent within 10% compared with the real instrument of 240 kg. Therefore, the maximum uncertainty for the number of the secondary particles is 10% level. To the physics process for the interaction between the cosmic rays and matters, we adopted the *QGSP_BERT_HP 2.4* hadron process package considering that it has better agreement of data for primary protons, neutrons, pions, and Kaons below 10 GeV than *QGSP*, which is the basic physics list using the quark gluon string model for the hadrons process calculation, and use the data driven high precision neutron package to transport neutrons below 20 MeV down to thermal energies. We customized the original *QGSP_BERT_HP 2.4* to replace *EmStandardPhysics* by *EmLivermorePhysics* so that the Doppler broadening is taken into account for gamma rays below 1 MeV.

To investigate the amount of the background for the ETCC, we need the particle fluxes of the proton, neutron, electron and positron, and thus we adopted the MAIRE model introduced by Lei *et al.* [125] (and the old name was QARM model). We assumed the positron flux identical to that of the electron, and this assumption is reasonable according to the MC simulation reported by Koldashov *et al.* [126]. For the MAIRE model, The parameters of the location, altitude, date, and a magnetic field disturbance index K_p, are assumed to be $(34.5°, -104.2°)$ (Ft. Sumner), 40 km, May 1, 2004, and $K_p = 2$. The date and K_p are nominal values and the particle fluxes are dependent on these parameters with a fluctuation of several percent. Figure 7.3 shows the model flux of primary particles for the date of May 1, 2004. Also, we assumed the incident direction of the particles that are generated in MC simulation to be only downward (zenith angle is 0 degrees) or upward (180 degrees), due to the lack of any observational data of angular dependence of the fluxes of protons, neutrons and electrons at balloon altitudes.

Figure 7.4 shows the flues of the gamma-rays that come to the active volume of TPC obtained by the MC simulation with zenith angle θ of $\theta < 90°$ (black), $90° > \theta$ (green), and total flux (red), respectively, and the fluxes of neutrons (red), electrons (blue), positrons (cyan), protons (purple), deuterons (pale orange), positive pion (light brown), and negative pion (pink). One can see the emission line of 511 keV, which results from the decay of the positronium produced near the TPC. The flux of the downward gamma rays intrinsically produced, $I_{\gamma,down}$, except for the line emission of 511 keV, is unavoidable background component, and can be fitted by the power law with an index which varies as a log parabola in

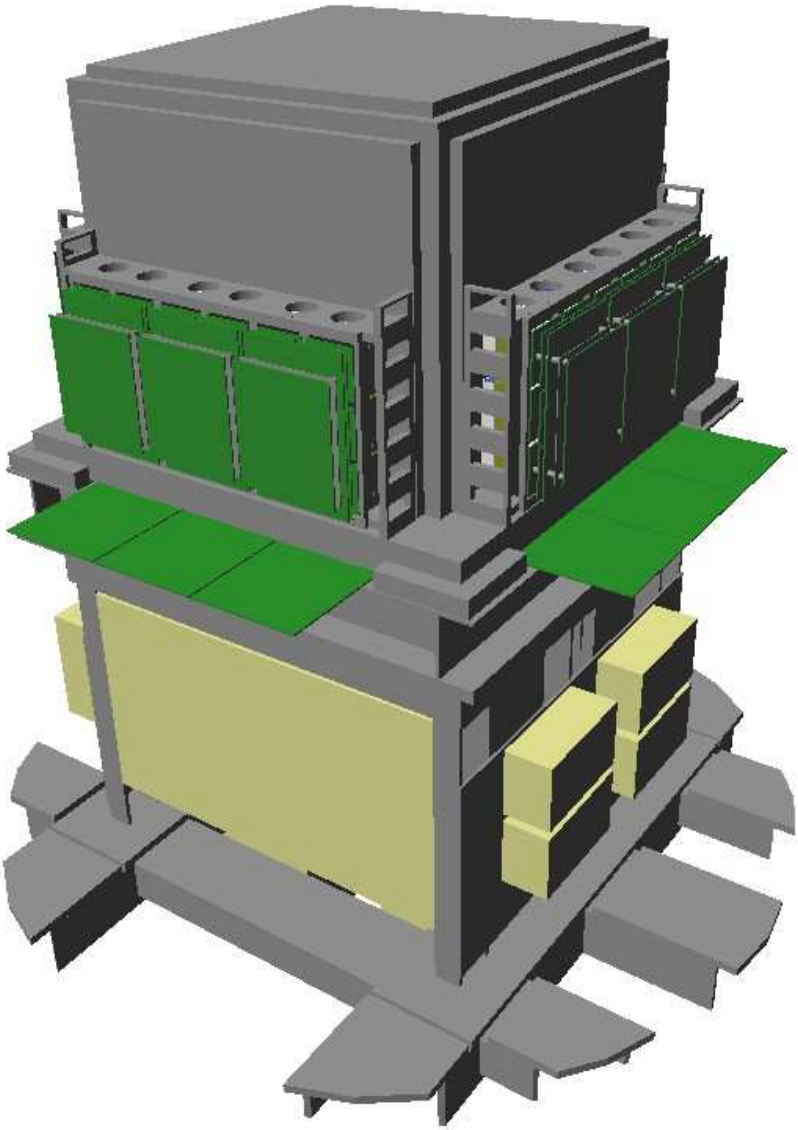

Fig. 7.2.— Mass model of the FM system.

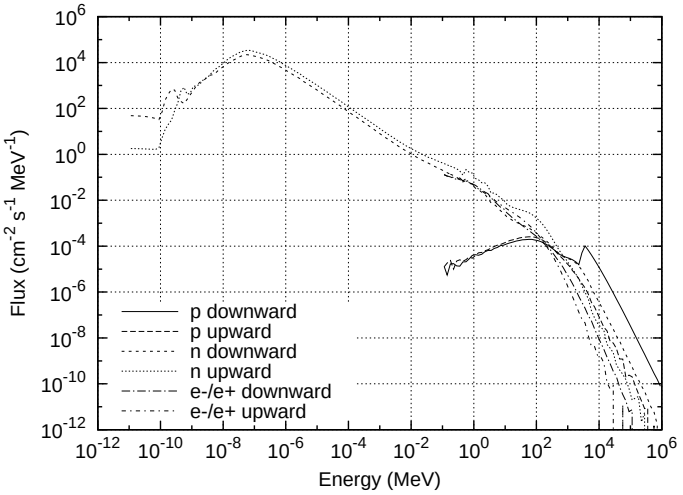

Fig. 7.3.— Fluxes of the primary incident particles derived by the QARM model under the condition with the date of May 1, 2004, and $K_p = 2$, and the latitude and longitude of 34.5 degrees and -104.2 degrees. 'downward' represents the flux of the incident zenith angle above 90 degrees, and 'upward' below 90 degrees.

energy:

$$I_{\gamma,\mathrm{down}} = (4.9 \pm 0.7) \times 10^{-5} \times \left(\frac{E}{1\,\mathrm{MeV}}\right)^{-(1.4+0.31\times\log10(\frac{E}{1\,\mathrm{MeV}}))} [\,\mathrm{cm}^{-2}\mathrm{s}^{-1}\mathrm{sr}^{-1}\mathrm{keV}^{-1}], \quad (7.4)$$

where the error of the normalization due to the model parameter dependence is taken account for. The intensity of the emission line of 511 keV produced in the equipment with an downward direction is estimated to be $I_{511} = (7 \pm 1) \times 10^{-2} [\,\mathrm{cm}^{-2}\mathrm{s}^{-1}\mathrm{sr}^{-1}]$. As mentioned, the events of charged particles can be rejected by the fiducial volume cut completely, and then the background events that remain after the energy loss cut and the fiducial volume cut are those of neutrons that mimic Compton scattering. The differential intensity of neutrons has a shape of two power laws jointing at 1 MeV, and can be fitted as

$$I_n = \begin{cases} (3.1 \pm 0.4) \times 10^{-5} \times E^{-0.50} [\,\mathrm{cm}^{-2}\mathrm{s}^{-1}\mathrm{sr}^{-1}\mathrm{keV}^{-1}] & (E < 1\mathrm{MeV}) \\ (3.1 \pm 0.4) \times 10^{-5} \times E^{-1.2} [\,\mathrm{cm}^{-2}\mathrm{s}^{-1}\mathrm{sr}^{-1}\mathrm{keV}^{-1}] & (E \geq 1\mathrm{MeV}) \end{cases}. \quad (7.5)$$

The integral of the differential neutron intensity with respect to the energy between 0.1 MeV and 10 MeV is ~ 0.10 cm^{-1}s^{-1}sr^{-1}. Using the current ETCC event selection criteria, the (mis)selection efficiency of the neutron events between 0.1 MeV and 1 GeV is less than 10^{-5}, which is calculated by a Monte Carlo simulation. This result indicates the elastic scattering events of neutrons are significantly suppressed with the ETCC by the energy loss cut and the fiducial volume cut.

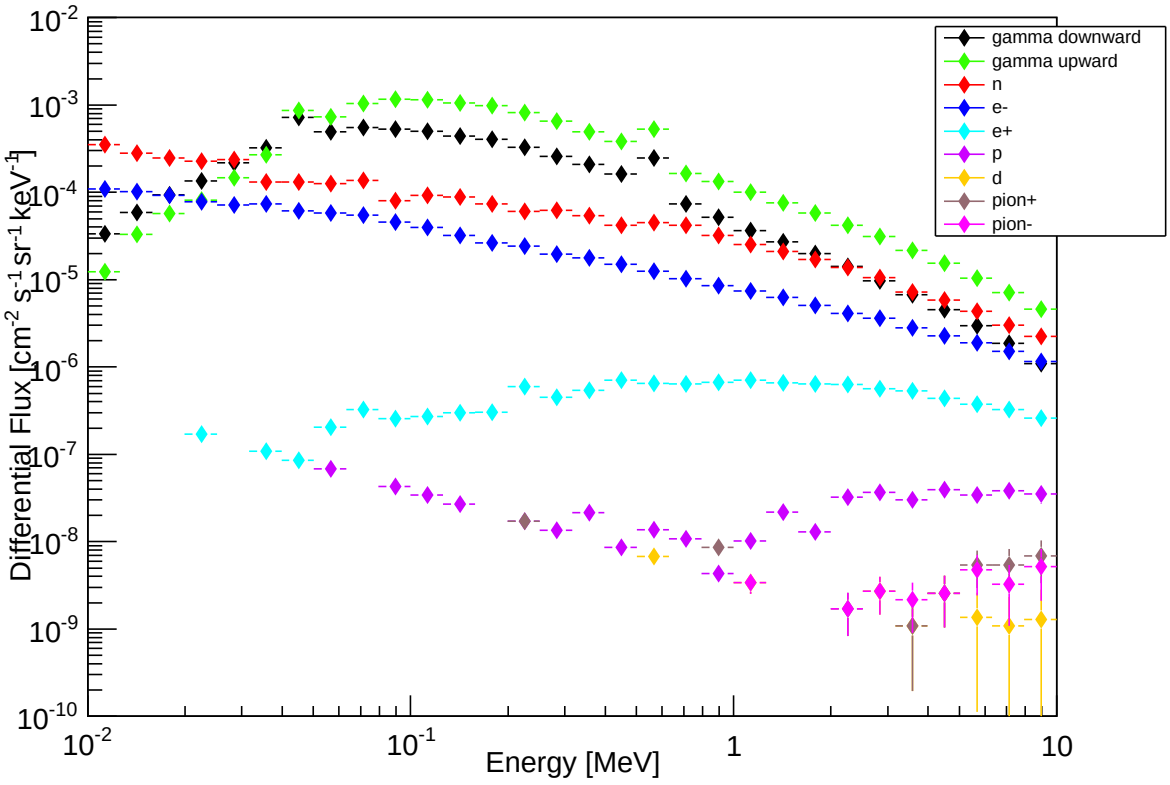

Fig. 7.4.— Fluxes of the gamma rays and particles that come to the active volume of the TPC, induced by the cosmic rays. The events of downward and upward gamma-rays (black and green, respectively), neutrons (red), electrons (blue), positrons (cyan), protons (purple), deuterons (pale orange), positive pion (light brown), and negative pion (pink) are plotted.

Table 7.1 shows the expected values of the number of the source and background events, the expected significance, and effective observation time during the one-day flight, which has an effective observation time of $2-3\times10^4$ seconds, assuming the PSF of 20 degrees. In that condition, however, it was found that there is marginal excess for each source. The same table but for the PSF of 10 degrees shows the considerable excesses for the all candidate sources (Table 7.2). Thus, the further improvement of the track reconstruction method or the effective area is required to accomplish the success criteria of the SMILE-II flight. For example, if the effective of the ETCC is increased by a factor of 1.4, the significance of Crab nebula can exceed 5σ level. One of the solution to achieve such condition is to increase the pressure of the filling gas of the TPC to 1.5 atm. The improvement of the SMILE-II ETCC is in progress (See [127]). We emphasize that the sensitivity calculation based on the principle of optics using the PSF was performed in the MeV gamma-ray energy band for the first time.

Table 7.1— Expected values of counting events from the source and background at SMILE-II one-day flight, assuming the PSF of 20 degrees.

	Crab nebula	Cyg X-1	GRO J0422+32
T [sec]	2.4×10^4	2.7×10^4	2.8×10^4
significance	4.3	2.7	2.9
$N_{\rm src}$ [counts]	185	126	130
$N_{\rm bgd}$ [counts]	1685	1985	1835
atmospheric	589	654	692
intrinsic gamma	564	626	661
intrinsic neutron	34	37	39
extragalactic	371	415	428
Galactic	127	253	14

Table 7.2— The same as Table 7.1 but for the PSF of 10 degrees.

	Crab nebula	Cyg X-1	GRO J0422+32
T [sec]	2.4×10^4	2.7×10^4	2.8×10^4
significance	7.4	5.0	5.3
$N_{\rm src}$ [counts]	185	126	130
$N_{\rm bgd}$ [counts]	424	500	462
atmospheric	148	165	174
intrinsic gamma	142	158	166
intrinsic neutron	8	9	10
extragalactic	94	104	108
Galactic	32	64	3

7.2 Gamma-ray burst search with Satellite-ETCC

In this section, sensitivities of the ETCC for GRBs with a satellite configuration are estimated by the numerical calculation. First, the sensitivity for the GRBs of which spectra are assumed to be the Band function is calculated. The detection of the GRB with a redshift more than 5 is expected as one of promising probe of the early universe. In addition, the sensitivity to the SGRBs associated with gravitational sources is discussed.

As a satellite ETCC, we assume the effective area of ~ 100 cm^2 for the sub-MeV band. This condition is derived from the fact that a typical payload size of a satellite is thought to be 1×1 m^2, and that the scattering probability at the former detector of a Compton camera should be less than or comparable to 5% to suppress multiple scattering of the gamma ray in the former detector. In such a case, The effective area considering the Compton scattering process only is 500 cm^2 at the highest, and the effective area as the Compton camera will be about 200 cm^2 due to other efficiencies such as photoabsorption in the latter detector and the event selection efficiency. We note that this condition must be applied to the all Compton cameras. To use gas for the Compton scattering target, the pure CF_4 gas with a pressure of 3 atm is a considerable candidate.

Under the condition on the effective area, the PSF in terms of optics must be attained to be less than 2 degrees in order to achieve the sensitivity of 1 mCrab for 10^6-second observation overcoming the diffuse cosmic gamma ray background. That sensitivity is essential to detect dim and high-redshift GRBs. For the coded aperture mask gamma-ray imagers, the PSF is identical to the FoV, and therefore it becomes a serious problem that there is trade-off between the sensitivity and the FoV. On the other hand, only the ETCC but none of classical Compton cameras can achieve such conditions. To improve the PSF to be 2 degrees, the SPD should be less than 5 degrees. Due to the multiple scattering effect of the recoil electrons, the ETCC must measure the recoil direction of the electron track by the hits near the vertex point within ~ 1 mm. This requirement for the electron tracking is a key point for future tasks of ETCCs.

In this section, we use the satellite-ETCC model introduced by Tanimori *et al.* [90]. The effective area for that satellite-ETCC calculated by the ETCC simulator are shown in Figure 7.5, and the major differences between the SMILE-II/ETCC and the satellite-ETCC are summarized in Table 7.3. For the satellite-ETCC, four units of the identical ETCCs, of which an active volume of TPC is $50 \times 50 \times 50$ cm^3 and the radiation length of the scintillator is 10, are supposed. Also the PSF is assumed to be 2 degrees.

Table 7.3— Configuration of the ETCCs

Configuration Name	Gas Mixtures	Gas Pressure	# of PSAs	R.L.
SMILE-II/ETCC	Ar(95%)/CF_4(3%)/iso-C_4H_{10}(2%)	1 atm	108	1 R.L.
satellite-ETCC (1 unit)	CF_4	3 atm	384	10 R.L.

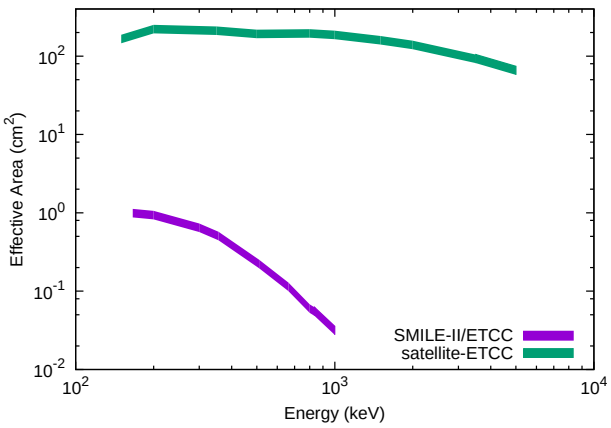

Fig. 7.5.— Effective areas for the current and future observations.

7.2.1 Sensitivity to high-z GRBs

To compare the GRB sensitivity among different detectors in an arbitrary energy band, Band formulated the minimum detection flux of a given detector [128]. That sensitivity of minimum detectable flux $F_{\rm min}$ with a significance level of σ_0 (that is normalized by 1σ) is represented as

$$F_{\rm min} = \frac{\int_{E_{\rm L}}^{E_{\rm H}} N(E)dE}{\int_{E_1}^{E_2} \epsilon(E)N(E)dE} \frac{\sigma_0\sqrt{Af_{\rm det}\Delta t\int_{E_1}^{E_2} B(E)dE}}{Af_{\rm det}f_{\rm mask}\Delta t}, \tag{7.6}$$

where $E_{\rm L}$ and $E_{\rm H}$ are the lower and upper limits of the energy that are used for the integral of the differential photon flux of the GRB, respectively. E_1 and E_2 are the lower and upper limit of the detector energy range. $N(E)$ and $B(E)$ are the GRB flux and background intensity, and $\epsilon(E)$, A, $f_{\rm det}$, $f_{\rm mask}$, and Δt are the detection efficiency, geometrical area of the detector, the fraction of the active area of the detector, the fraction of the aperture that must be considered in the case of the coded aperture imaging, and the observation time, respectively. In this formulation, the background intensity is described as

$$B(E) = \epsilon(E)\Delta\Omega f_{\rm mask}N_{\rm B}(E) + B_{\rm int}. \tag{7.7}$$

Here, the spectrum of the GRB is assumed to be the Band function Eq. 2.1, and $\alpha = -1$ and $\beta = -2.3$ for the comparison of the GRB detection rate by Ghirlanda *et al.* (2015) that is calculated under the condition of the same mean values. Also we suppose $f_{\rm mask} = f_{\rm det} = 1$, and the effective area is equivalent to $Af_{\rm det}\epsilon(E)$. As the background events, we assume the cosmic X-ray background (CXB) that covers from 10 keV to 1 MeV, obtained by the *Swift*/BAT [129], due to comparison with the sensitivity of the *Swift*/BAT. In the case of the ETCC, we assume the instrumental background rate as high as CXB. We note that the number of the photons from the GRBs that come within the solid angle $\Delta\Omega$ is the half of the whole photons if we take the solid angle as the region surrounded by the circle with a radius of the PSF, and therefore the minimum detection flux and fluence are twice as high as the values calculated with the Eq. 7.6.

For a shorter integral time, the sensitivity of the ETCC is limited by the number of photons from the GRB because the background counting rate within the solid angle in interest is less than 1 photon per second owing to the imaging capability of the ETCC. Thus, the advantage of the satellite-ETCC would be the image trigger with a long integral time. Here we calculate the flux limit for integral times of 10 seconds and 100 seconds, requiring the number of photons from the source to be 50 photons, and then the corresponding signal-to-noise ratio σ_0 are 41 and 13, respectively. For an integral time of 1000 seconds, the background counting rate goes high and thus we require the signal-to-noise ratio σ_0 to be higher than 8, and the corresponding number of the photons from the source is 97 photons. Using the center of gravity of the counting photons, the localization of GRBs can be realized

to be $2^\circ/\sqrt{50} \approx 0.3^\circ$, which is a suitable field of view for follow-up telescopes. Figure 7.6 shows the photon fluence sensitivity of GRBs with a duration of 10 sec, 100 sec, and 1000 sec in 50 - 300 keV band, derived applying $E_L = 50\,\mathrm{keV}$ and $E_H = 300\,\mathrm{keV}$. The fluence sensitivity achieved $\sim 1.5\,\mathrm{ph\,cm^{-2}}$ for the integral time of 10 - 100 seconds, and $\sim 2.9\,\mathrm{ph\,cm^{-2}}$ for 1000 seconds. Comparing the GRB rate dependence on the photon fluence as shown in Fig. 7.7, the corresponding detection rates of the GRBs are 70 - 100 events $\mathrm{year^{-1}\,sr^{-1}}$ for all redshifts, 5 - 7 events $\mathrm{year^{-1}\,sr^{-1}}$ for $z > 5$, and 0.3 - 0.5 events $\mathrm{year^{-1}\,sr^{-1}}$ for $z > 10$, respectively, as shown in Fig. 7.7. We note that this calculation focused on the LGRBs, while GRBs originating from Pop III star are not involved but expected to be detected by accomplishing such high sensitivity. This is because that the Pop III GRB properties of a long duration of $10^4 - 10^5$ seconds and a total energy of 10^{54} erg matches the imaging ability of the ETCC. The FoV of the ETCC can be realized to be ~ 4 sr if the ETCC configuration is not quite different from that at SMILE-II, and therefore the satellite-ETCC will be a potent tool to probe the star formation rate in the early universe.

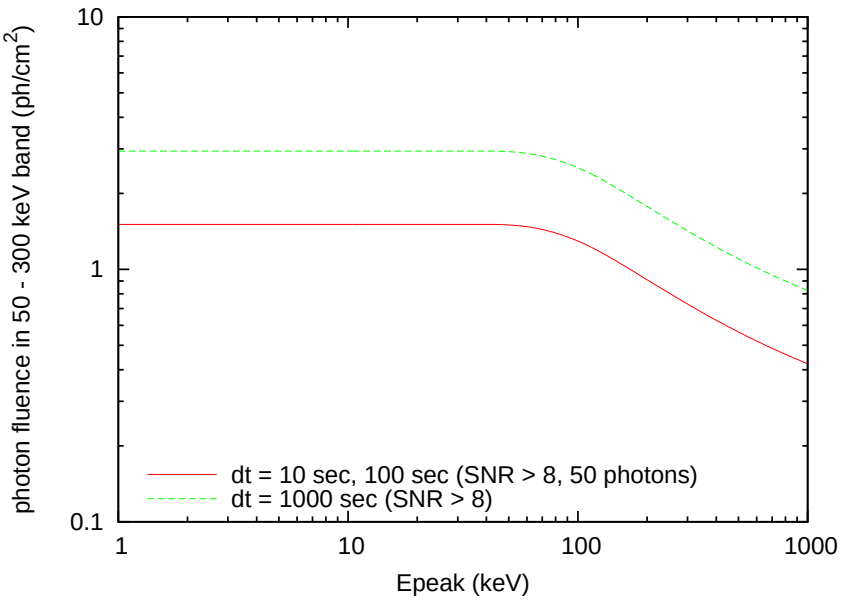

Fig. 7.6.— photon fluence sensitivity of GRBs in 50 - 300 keV band for the satellite-ETCC.

7.2.2 Sensitivity to short GRBs

It is important to localize SGRBs within 1 degrees for the follow-up observation by other X-ray/optical telescopes in terms of the identification of the host galaxy. Here we calculate the flux limit for SGRBs with an integral times of 1 second, requiring the number

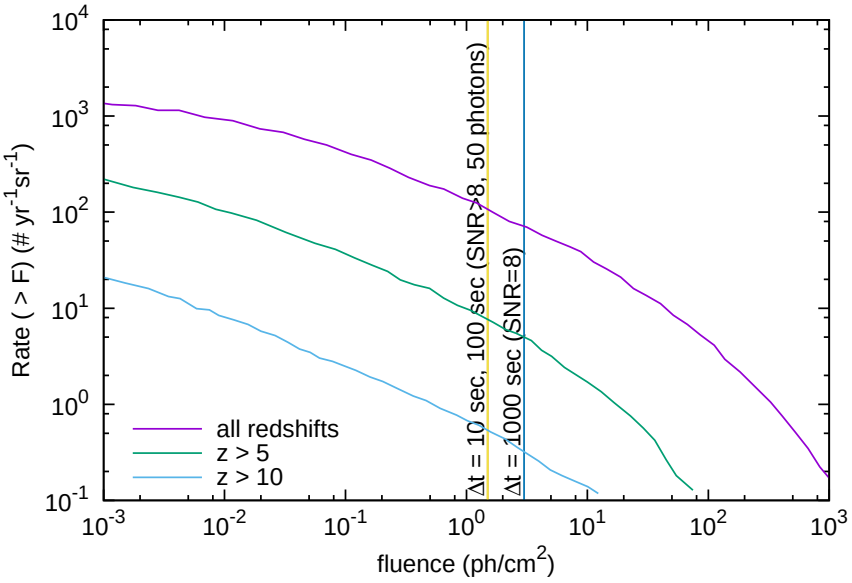

Fig. 7.7.— Photon fluence sensitivity of GRBs in 50 - 300 keV band for the satellite-ETCC and detection rate of GRBs. The detection rate is the data from [44].

of the photons from the source to be 10 photons or 25 photons, and then the corresponding signal-to-noise ratio σ_0 and the position determination accuracies are 27 and 66, and ~ 0.6 degrees and ~ 0.4 degrees, respectively. Figure 7.8 shows the sensitivity for 1-sec peak photon flux in 1 - 1000 keV. The satellite-ETCC has a comparable sensitivity near 490 keV as that of BATSE. The corresponding photon and energy flux limits are 0.5 ph cm^{-2}s^{-1}, and $\sim 1.3 \times 10^{-7}$ erg cm^{-2}s^{-1}, respectively. In this paper, we compare the detection flux limit of BATSE applying the background rate is determined by the cosmic diffuse X-ray background. On the other hand, the flux limit of the BATSE for SGRBs was estimated by Yonetoku et al. from the observation data, to be $\sim 4 \times 10^{-6}$ erg cm^{-2}s^{-1}, or could be better by a factor of 4, and therefore the satellite ETCC has 10 times better sensitivity than that of BATSE. Noting that the cumulative luminosity function is proportional to L^{-1} [55], we can expect that the event rate of SGRBs can be higher by a factor of ~ 10 if the flux threshold is improved by a factor of 10 and the luminosity function of SGRBs can be extrapolated to 10^{49} erg s^{-1}. Then the gravitational-wave detection rate becomes ~ 40 events yr^{-1} for NS-NS binaries (< 200 Mpc), while Abadie et al. (2010) suggested that the likely binary neutron-star detection rate for Advanced LIGO-Virgo network will be 40 events per year, with a range between 0.4 and 400 events per year in their review paper [130]. The corresponding event rate of SGRBs is ~ 0.2 event per year, if the half opening angle of the GRB jet is assumed to be 6 degrees, which is the assumption as the minimum opening angle [55]. Thus, the ETCC will a promising provide chance to the simultaneous observation of the gravitational and

electromagnetic waves from binary neutron star mergers.

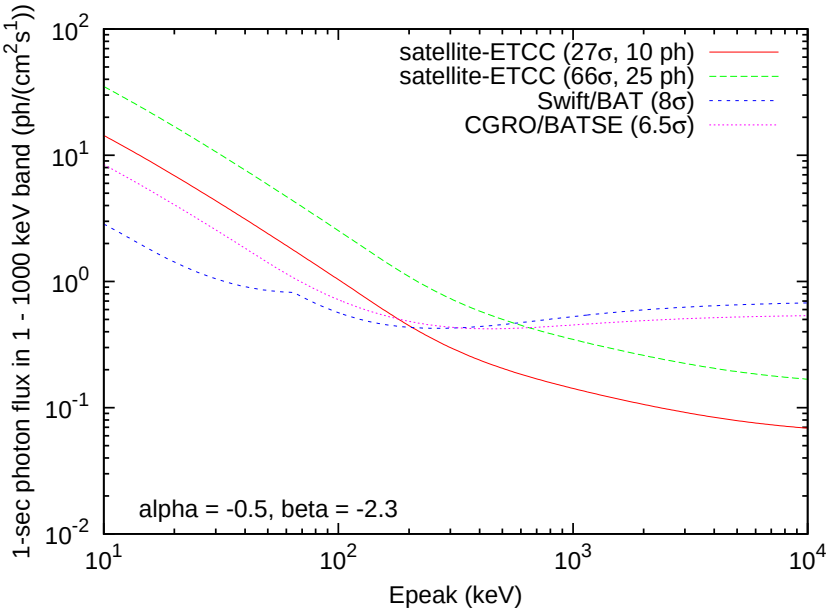

Fig. 7.8.— 1-sec photon flux sensitivity of GRBs in 1 - 1000 keV band for the satellite-ETCC.

Chapter 8

Conclusion

The goal of the SMILE project is to observe deep MeV gamma-ray universe with 100 times higher sensitivity than that of COMPTEL and perform all-sky survey for faint sources less than 1 mCrab. Based on the result of SMILE-I that showed the potent background rejection ability, the SMILE-II ETCC with an effective area 50 times larger than that of SMILE-I and an angular resolution ARM less than 10 degrees was designed and developed to demonstrate the imaging performance of the ETCC. These requirements are achieved by enlargement of the ETCC and the improvement of the detection efficiency of the electron track data by factors of 18 and 10, respectively.

The definition of the PSF based on the principle of the optics for MeV gamma-ray photons excludes the uncertainty on the detection sensitivity as well as other wavelength bands, contributing to the improvement of reliability on observational predictions. Especially, for Compton cameras not only the ARM but also the SPD must be improved to obtain a sharp PSF.

By estimating the sensitivity based on the PSF and developing the precise simulator of the ETCC, we can have a prospect to the SMILE-II observation; with the PSF of 10 degrees, the ETCC can observe Crab nebula at the statistical significance level of 7.4σ for one-day flight in the middle latitude.

This simulation also clarifies how we should the design for the future development, such as a satellite ETCC aiming to 1-mCrab sources. The satellite-class ETCC will enable us to detect high-redshift GRBs by the image trigger with a duration of 10 - 1000 seconds. Expected detection rates of the high-redshift GRBs are 5 - 7 events/yr/sr for $z > 5$, and 0.3 - 0.5 events/yr/sr for $z > 10$, respectively. For short duration GRBs, the ETCC has a sensitivity with a photon flux limit of 0.5 ph $\mathrm{cm}^{-2}\mathrm{s}^{-1}$, with a photon limit of 25 photons. Considering the wide field of view of ETCC and the corresponding detection rate of SGRBs

that occur with a distance less than 200 Mpc is about ~ 0.2 events per year in the all sky, the ETCC will provide a promising chance to observe the electromagnetic counterpart of a gravitational wave source. The localization capability of the ETCC with < 1 degree will contribute to the determination of the host galaxy of GRBs by follow-up observations using optical/NIR telescopes.

Finally, the development of the SMILE-II ETCC, which realized the first true imaging based on the optics for the MeV gamma-ray band, showed a good feasibility of the future satellite observation for 1-mCrab sources.

Acknowledgments

I would like to express my deep gratitude to Prof. Toru Tanimori, whose suggestions made enormous contribution to this thesis. I also would like to my gratitude to Dr. Atsushi Takada for a plenty of insightful comments. I specially thank μ-PIC collaborators: Associate Prof. Hidetoshi Kubo, Dr. Parker Joseph, Dr. Kazuki Ueno, Dr. Yoshitaka Mizumura, Dr. Tetsuya Mizumoto, Dr. Kiseki Nakamura, Yoshihiro Matsuoka, Shotaro Komura, and Taito Takemura. Finally, I would like to thank to my family for having brought me up with continuous encouragements.

Appendix A

Cumulative μ-PIC response

Figure A.1 shows the cumulative induced current of an single electron with $A = 1$ in Eq. 6.4. Here we define the signal duration as the time T_λ within which the induced charge has the half of the total one. T_λ is formally described as $T_\lambda := t_2 - t_1$, where t_1 and t_2 agree $\int_0^{t_1} I dt = \lambda\, e$ and $\int_0^{t_2} I dt = (\lambda + 0.5)\, e$, and λ is the lower boundary time of the integral. The distributions of the duration of the signals for $\lambda = 0.05\,\mu$s and $\lambda = 0.25\,\mu$s are as shown in Fig. A.2. The mean of $T_{0.05}$ and $T_{0.25}$ are 1.3×10^2 ns and 3.2×10^2 ns, that are longer than the time constant of the amplifier in the new readout board. Therefore, to gain the signal against the noise, it would be helpful to make the shaping time longer to about 100 ns. This will be treated by the study of convolution of the μ-PIC and electrics response in the next section.

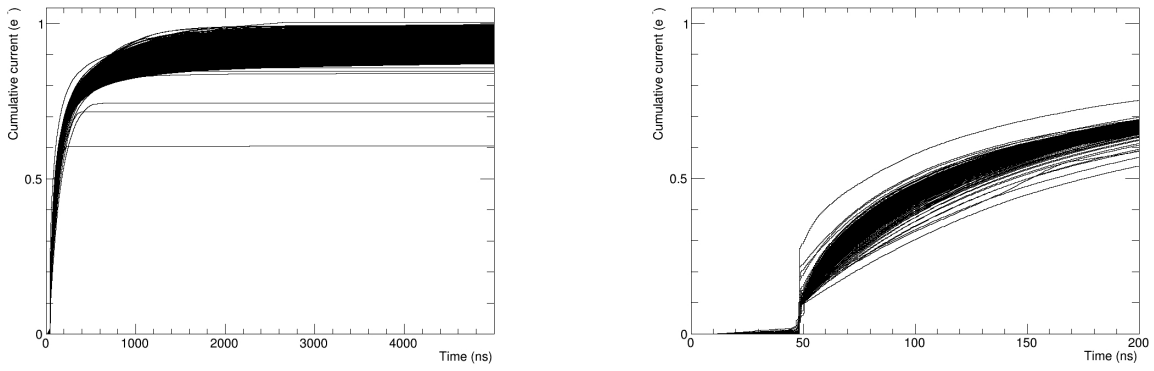

Fig. A.1.— 2000 samples of Cumulative μ-PIC current response.

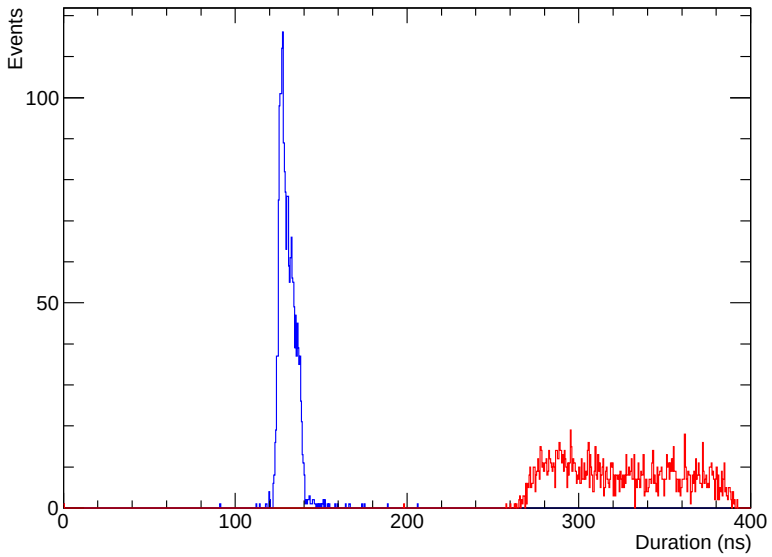

Fig. A.2.— Distribution of duration time of μ-PIC within which the induced charge contains the half of the elementary charge, in early time (blue solid) and in the middle time (red solid).

Appendix B

Convolution of μ-PIC and electronics response

The convolution of the responses of the μ-PIC current and the electronics is shown in Fig. B.1, for which the electron multiplication factor is 2×10^4, that is the nominal gas gain in the SMILE-II TPC operation. Note that the response is the output at 'XAOUT', and the signal that is connected to the comparator to generate the TOT is the magnified by a factor of 150 (three times at the attenuating summing-amplifier in the chip and 50 times at the amplifier before the comparator. See Fig. 5.6). One can see that most of the signals have peaks at near 0.8 mV and therefore required threshold levels are easy to be estimated by a simple calculation. The rate of energy loss of the minimum ionizing particles (MIPs) in light material is approximately $2\,\mathrm{MeV/(g/cm^2)}$ [64]. The density of pure argon gas of the standard temperature and pressure is $1.8\,\mathrm{mg/cm^3}$ and then, the energy loss of the MIPs in the argon gas within the 0.8 mm width is 2.9×10^2 eV and the number of the produced ion-electron pairs is ~ 11. Thus, the nominal pulse height for the MIPs is ~ 9 mV, and if one wants to read TOT above the half of the pulse heights, the corresponding required threshold level is $V_{\mathrm{th}} \sim \frac{1}{2} \times 9 \times 150 \sim 600\,\mathrm{mV}$. In the practical case, the electron cloud is spatially distributed, and the TOT response should be derived by the convolution of the response of the waveforms as shown in Fig. B.1 and the distribution of the electron cloud. However, the straightforward calculation of this convolution has a lot of CPU costs, and we would like to know how long the response of waveforms should be taken account for to calculate reasonable TOT response. Figure B.2 shows 2000 samples of the cumulative waveform response, and $1.5\,\mu$s should be considered to involve more than 90% of the total energy in the response for the almost all of the samples.

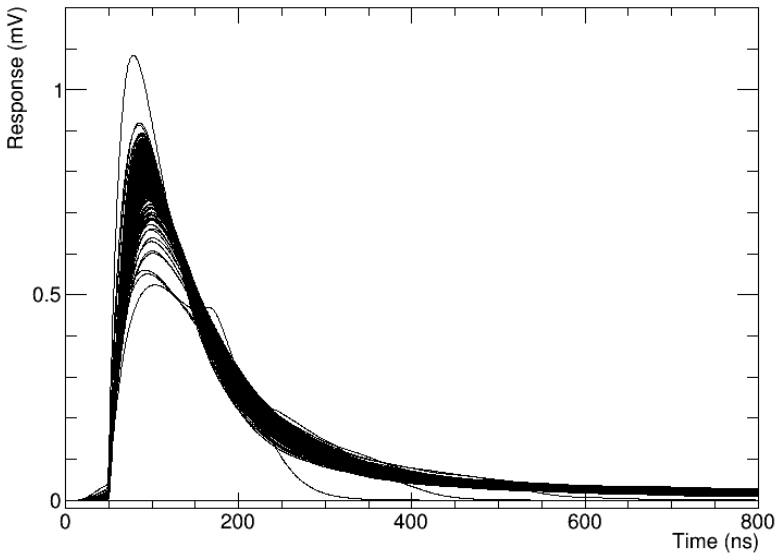

Fig. B.1.— Superposition of 2000 samples of the convolution of the response of the μ-PIC current and the electronics, for which the electron multiplication factor of the gas detector is 2×10^4.

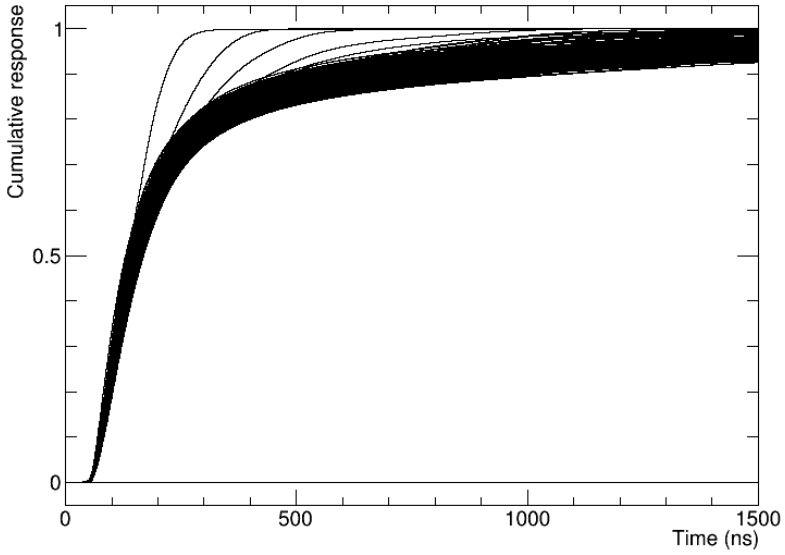

Fig. B.2.— Superposition of 2000 samples of the cumulative response, where the response is as shown in Fig. B.1.

Appendix C

Measurement of TOT response for MIP-like events

To extract MIP-like events from the background data, we used background data of the SMILE-II/ETCC obtained by the calibration run. The setup of the ETCC was as follows; the the normal vector of the front face of the ETCC is orthogonal to the zenith, *i.e.* the ETCC is lying on the ground so as to obtain efficiently the cosmic ray events that are orthogonal to the drift direction, not parallel. This is because the response of the events that travel along to the drift direction is complicated due to the broad distribution of the seed electrons, and the events that are orthogonal to the drift direction is more primitive for the TOT response investigation. In this way, the electrodes of the anode strip were aligned parallel to the zenith, and the those of the cathode are parallel to the horizontal direction. As a result, we can obtain the events that are orthogonal to the drift direction in the projected plane derived by the cathode data. Hereafter, we call this plane the 'cathode plane'. The first criteria of the event selection for the MIP-like events that travel orthogonal to the drift direction are on the hit pattern and energy loss in the PSA (hereafter, PSA cut):

(1) The single PMT has hit at the two sides of the PSA; one is that faces to the zenith and the other is to the nadir.

(2) There is no other hit at any side of the PSA.

(3) The both A-D converted hit signals are saturated.

There remain random coincident background events after that cut. To suppress them, we fitted the projected trajectory in the cathode plane by a straight line, and calculate the reduced χ^2, where the point and corresponding error are chosen as the mean and the standard

deviation of the TOT for each strip, and the results are shown in Fig. C.1. The blue points represent χ^2 distribution of the all events taken by the SMILE-II/ETCC, and the red are the distribution of the events with which the conditions about the PSA are satisfied. Though the PSA cut effectively rejects the events with large reduced χ^2, there still remain the events with a reduced χ^2 above 5. As the second event-cut criterion, we selected the events with a χ^2 less than 5, which is at about half point of the most probable χ^2 as good events (hereafter, χ^2 cut). Figure C.2 shows the distribution of the projected angle of the fitted line. The distribution for all events are shown with black points, the events of the PSA cut with cyan, and the events of the PSA cut and χ^2 cut with magenta. We fitted these angle distributions with a normal distribution, and the deviations are 8.8 ± 0.3 degrees for PSA cut and 9.8 ± 0.5 degrees for PSA cut and χ^2 cut, respectively. Figure C.3 shows the measured TOT distributions of all events (black), those of PSA cut (cyan), and those of PSA cut and χ^2 cut (magenta). The most probable values of the TOT distributions for the events of the PSA cut and the PSA and χ^2 cuts are approximately 10 clocks, and the TOT distributions have a shape like the Landau distribution, resulting from the energy loss process of the charged particles in the TPC. One can see the χ^2 cut reduces the events above 20 clocks in the distribution.

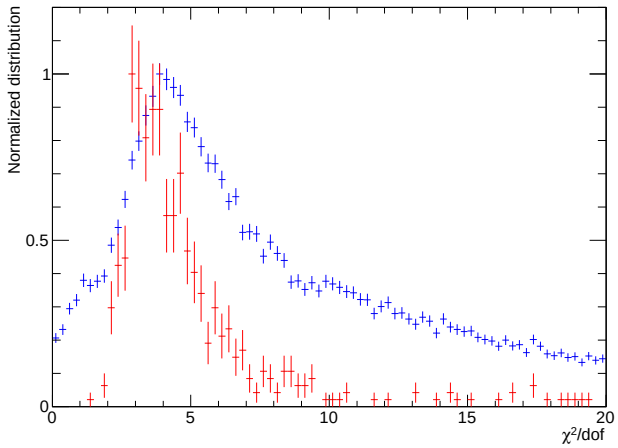

Fig. C.1.— The distributions of the reduced χ^2 for the fitting of the projected trajectory by a linear function. The blue points represent the all events, and the red ones are the events satisfy the PSA cut conditions. The distributions are normalized by the maximum bin content.

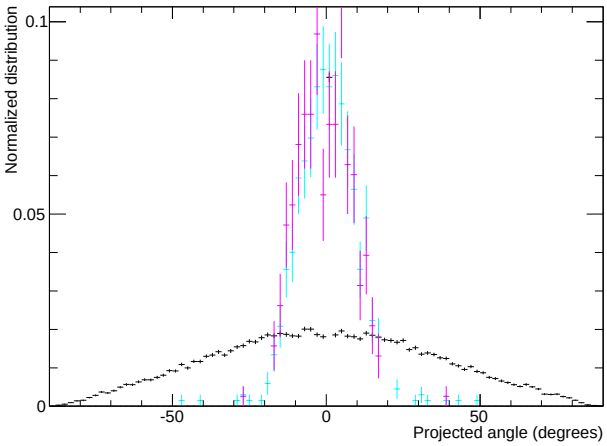

Fig. C.2.— The distributions of the projected angles of the trajectory by a linear function. The black points represent the all events, the cyan with the PSA cut, and the magenta with the both PSA cut and χ^2. The detail explanation of the PSA and χ^2 cuts are discussed in the text.

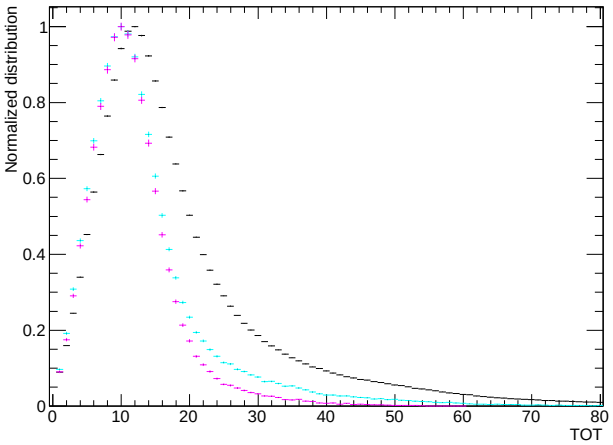

Fig. C.3.— The distributions of the TOT of the tracks. The black points represent the all events, the cyan with the PSA cut, and the magenta with the both PSA cut and χ^2. The detail explanation of the PSA and χ^2 cuts are discussed in the text.

References

[1] Volker Schönfelder. *The Universe in gamma rays*. Springer Science & Business Media, 2013.

[2] V Schönfelder, K Bennett, JJ Blom, H Bloemen, W Collmar, A Connors, R Diehl, W Hermsen, A Iyudin, RM Kippen, et al. The first comptel source catalogue. *Astronomy and Astrophysics Supplement Series*, 143(2):145–179, 2000.

[3] W. H. Baumgartner, J. Tueller, C. B. Markwardt, G. K. Skinner, S. Barthelmy, R. F. Mushotzky, P. A. Evans, and N. Gehrels. The 70 Month Swift-BAT All-sky Hard X-Ray Survey. *ApJS*, 207:19, August 2013.

[4] T. Sakamoto, S. D. Barthelmy, W. H. Baumgartner, J. R. Cummings, E. E. Fenimore, N. Gehrels, H. A. Krimm, C. B. Markwardt, D. M. Palmer, A. M. Parsons, G. Sato, M. Stamatikos, J. Tueller, T. N. Ukwatta, and B. Zhang. The Second Swift Burst Alert Telescope Gamma-Ray Burst Catalog. *ApJS*, 195:2, July 2011.

[5] The Fermi-LAT Collaboration. Fermi large area telescope third source catalog. *arXiv preprint arXiv:1501.02003*, 2015.

[6] P. L. Nolan, A. A. Abdo, M. Ackermann, M. Ajello, A. Allafort, E. Antolini, W. B. Atwood, M. Axelsson, L. Baldini, J. Ballet, and et al. Fermi Large Area Telescope Second Source Catalog. *ApJS*, 199:31, April 2012.

[7] V. Schönfelder. Lessons learnt from COMPTEL for future telescopes. *New Astronomy Reviews*, 48:193–198, February 2004.

[8] S. M. Matz, G. H. Share, and E. L. Chupp. SMM gamma-ray observations of SN 1987A. In N. Gehrels and G. H. Share, editors, *Nuclear Spectroscopy of Astrophysical Sources*, volume 170 of *American Institute of Physics Conference Series*, pages 51–59, September 1988.

[9] Roland Diehl, Thomas Siegert, Wolfgang Hillebrandt, Sergei A Grebenev, Jochen Greiner, Martin Krause, Markus Kromer, Keiichi Maeda, Friedrich Röpke, and Stefan

Taubenberger. Early 56ni decay gamma rays from sn2014j suggest an unusual explosion. *Science*, 345(6201):1162–1165, 2014.

[10] Eugene Churazov, Rashid Sunyaev, J Isern, J Knödlseder, Pierre Jean, François Lebrun, Nikolai Chugai, Sergei Grebenev, E Bravo, Sergei Sazonov, et al. Cobalt-56 [ggr]-ray emission lines from the type ia supernova 2014j. *Nature*, 512(7515):406–408, 2014.

[11] Roland Diehl, Nikos Prantzos, and Peter von Ballmoos. Astrophysical constraints from gamma-ray spectroscopy. *Nuclear Physics A*, 777:70–97, 2006.

[12] S Plüschke, R Diehl, V Schönfelder, H Bloemen, W Hermsen, K Bennett, C Winkler, M McConnell, J Ryan, U Oberlack, et al. The comptel 1.809 mev survey. *arXiv preprint astro-ph/0104047*, 2001.

[13] W Wang, MG Lang, R Diehl, H Halloin, P Jean, J Knödlseder, K Kretschmer, P Martin, JP Roques, AW Strong, et al. Spectral and intensity variations of galactic ^{26}al emission. *Astronomy & Astrophysics*, 496(3):713–724, 2009.

[14] Laurent Bouchet, Elisabeth Jourdain, and Jean-Pierre Roques. The galactic 26al emission map as revealed by integral spi. *The Astrophysical Journal*, 801(2):142, 2015.

[15] Nikos Prantzos and Roland Diehl. Radioactive 26 al in the galaxy: observations versus theory. *Physics Reports*, 267(1):1–69, 1996.

[16] R. Diehl. Cosmic Gamma-Ray Spectroscopy. *The Astronomical Review*, 8(3):19–65, July 2013.

[17] David M Smith. Gamma-ray line observations with rhessi. *arXiv preprint astro-ph/0404594*, 2004.

[18] W Wang, MJ Harris, R Diehl, H Halloin, B Cordier, AW Strong, K Kretschmer, J Knödlseder, P Jean, GG Lichti, et al. Spi observations of the diffuse ^{60}fe emission in the galaxy. *Astronomy & Astrophysics*, 469(3):1005–1012, 2007.

[19] R. W. Klebesadel, I. B. Strong, and R. A. Olson. Observations of Gamma-Ray Bursts of Cosmic Origin. *ApJ*, 182:L85, June 1973.

[20] G. J. Fishman, C. A. Meegan, R. B. Wilson, T. A. Parnell, W. S. Paciesas, G. N. Pendleton, H. S. Hudson, J. L. Matteson, L. E. Peterson, T. L. Cline, B. J. Teegarden, and B. E. Schaefer. The BATSE Experiment for the GRO - Solar Flare Hard X-Ray and Gamma-Ray Capabilities. In *Bulletin of the American Astronomical Society*, volume 21 of *Bulletin of the American Astronomical Society*, page 860, March 1989.

[21] Batse-original notices. `http://gcn.gsfc.nasa.gov/original.html`.

[22] E. Costa, F. Frontera, J. Heise, M. Feroci, J. in't Zand, F. Fiore, M. N. Cinti, D. Dal Fiume, L. Nicastro, M. Orlandini, E. Palazzi, M. Rapisarda#, G. Zavattini, R. Jager, A. Parmar, A. Owens, S. Molendi, G. Cusumano, M. C. Maccarone, S. Giarrusso, A. Coletta, L. A. Antonelli, P. Giommi, J. M. Muller, L. Piro, and R. C. Butler. Discovery of an X-ray afterglow associated with the γ-ray burst of 28 February 1997. *Nature*, 387:783–785, June 1997.

[23] Iau circular 6584: Grb 970228. `http://www.cbat.eps.harvard.edu/iauc/06500/06584.html`.

[24] M. R. Metzger, S. G. Djorgovski, S. R. Kulkarni, C. C. Steidel, K. L. Adelberger, D. A. Frail, E. Costa, and F. Frontera. Spectral constraints on the redshift of the optical counterpart to the γ-ray burst of 8 May 1997. *Nature*, 387:878–880, June 1997.

[25] Ruben Salvaterra, Sergio Campana, Susanna D Vergani, Stefano Covino, Paolo D ' Avanzo, Dino Fugazza, Giancarlo Ghirlanda, Gabriele Ghisellini, Andrea Melandri, Lara Nava, et al. A complete sample of bright swift long gamma-ray bursts. i. sample presentation, luminosity function and evolution. *The Astrophysical Journal*, 749(1):68, 2012.

[26] GJ Fishman. Observed properties of gamma-ray bursts. *Astronomy and Astrophysics Supplement Series*, 138(3):395–398, 1999.

[27] C. Kouveliotou, C. A. Meegan, G. J. Fishman, N. P. Bhat, M. S. Briggs, T. M. Koshut, W. S. Paciesas, and G. N. Pendleton. Identification of two classes of gamma-ray bursts. *ApJ*, 413:L101–L104, August 1993.

[28] T. J. Galama, P. M. Vreeswijk, J. van Paradijs, C. Kouveliotou, T. Augusteijn, H. Böhnhardt, J. P. Brewer, V. Doublier, J.-F. Gonzalez, B. Leibundgut, C. Lidman, O. R. Hainaut, F. Patat, J. Heise, J. in't Zand, K. Hurley, P. J. Groot, R. G. Strom, P. A. Mazzali, K. Iwamoto, K. Nomoto, H. Umeda, T. Nakamura, T. R. Young, T. Suzuki, T. Shigeyama, T. Koshut, M. Kippen, C. Robinson, P. de Wildt, R. A. M. J. Wijers, N. Tanvir, J. Greiner, E. Pian, E. Palazzi, F. Frontera, N. Masetti, L. Nicastro, M. Feroci, E. Costa, L. Piro, B. A. Peterson, C. Tinney, B. Boyle, R. Cannon, R. Stathakis, E. Sadler, M. C. Begam, and P. Ianna. An unusual supernova in the error box of the γ-ray burst of 25 April 1998. *Nature*, 395:670–672, October 1998.

[29] E. Berger, P. A. Price, S. B. Cenko, A. Gal-Yam, A. M. Soderberg, M. Kasliwal, D. C. Leonard, P. B. Cameron, D. A. Frail, S. R. Kulkarni, D. C. Murphy, W. Krzeminski, T. Piran, B. L. Lee, K. C. Roth, D.-S. Moon, D. B. Fox, F. A. Harrison, S. E. Persson,

B. P. Schmidt, B. E. Penprase, J. Rich, B. A. Peterson, and L. L. Cowie. The afterglow and elliptical host galaxy of the short γ-ray burst GRB 050724. *Nature*, 438:988–990, December 2005.

[30] J. Grindlay, S. Portegies Zwart, and S. McMillan. Short gamma-ray bursts from binary neutron star mergers in globular clusters. *Nature Physics*, 2:116–119, February 2006.

[31] Batse grb durations. `https://gammaray.nsstc.nasa.gov/batse/grb/duration/`.

[32] MS Briggs, DL Band, RM Kippen, RD Preece, C Kouveliotou, J Van Paradijs, GH Share, RJ Murphy, SM Matz, A Connors, et al. Observations of grb 990123 by the compton gamma ray observatory. *The Astrophysical Journal*, 524(1):82, 1999.

[33] D. Band, J. Matteson, L. Ford, B. Schaefer, D. Palmer, B. Teegarden, T. Cline, M. Briggs, W. Paciesas, G. Pendleton, G. Fishman, C. Kouveliotou, C. Meegan, R. Wilson, and P. Lestrade. BATSE observations of gamma-ray burst spectra. I - Spectral diversity. *ApJ*, 413:281–292, August 1993.

[34] Adam Goldstein, Robert D Preece, Robert S Mallozzi, Michael S Briggs, Gerald J Fishman, Chryssa Kouveliotou, William S Paciesas, and J Michael Burgess. The batse 5b gamma-ray burst spectral catalog. *The Astrophysical Journal Supplement Series*, 208(2):21, 2013.

[35] T. Piran. Astronomy: Glowing embers. *Nature*, 422:268–269, March 2003.

[36] D. Yonetoku, T. Murakami, S. Gunji, T. Mihara, K. Toma, T. Sakashita, Y. Morihara, T. Takahashi, N. Toukairin, H. Fujimoto, Y. Kodama, S. Kubo, and IKAROS Demonstration Team. Detection of Gamma-Ray Polarization in Prompt Emission of GRB 100826A. *ApJ*, 743:L30, December 2011.

[37] Wayne Coburn and Steven E Boggs. Polarization of the prompt γ-ray emission from the γ-ray burst of 6 december 2002. *Nature*, 423(6938):415–417, 2003.

[38] C Wigger, W Hajdas, K Arzner, M Güdel, and A Zehnder. Gamma-ray burst polarization: limits from rhessi measurements. *The Astrophysical Journal*, 613(2):1088, 2004.

[39] F. J. Virgili, C. G. Mundell, V. Pal'shin, C. Guidorzi, R. Margutti, A. Melandri, R. Harrison, S. Kobayashi, R. Chornock, A. Henden, A. C. Updike, S. B. Cenko, N. R. Tanvir, I. A. Steele, A. Cucchiara, A. Gomboc, A. Levan, Z. Cano, C. J. Mottram, N. R. Clay, D. Bersier, D. Kopač, J. Japelj, A. V. Filippenko, W. Li, D. Svinkin, S. Golenetskii, D. H. Hartmann, P. A. Milne, G. Williams, P. T. O'Brien, D. B. Fox, and E. Berger. GRB 091024A and the Nature of Ultra-long Gamma-Ray Bursts. *ApJ*, 778:54, November 2013.

[40] A. J. Levan, N. R. Tanvir, R. L. C. Starling, K. Wiersema, K. L. Page, D. A. Perley, S. Schulze, G. A. Wynn, R. Chornock, J. Hjorth, S. B. Cenko, A. S. Fruchter, P. T. O'Brien, G. C. Brown, R. L. Tunnicliffe, D. Malesani, P. Jakobsson, D. Watson, E. Berger, D. Bersier, B. E. Cobb, S. Covino, A. Cucchiara, A. de Ugarte Postigo, D. B. Fox, A. Gal-Yam, P. Goldoni, J. Gorosabel, L. Kaper, T. Krühler, R. Karjalainen, J. P. Osborne, E. Pian, R. Sánchez-Ramírez, B. Schmidt, I. Skillen, G. Tagliaferri, C. Thöne, O. Vaduvescu, R. A. M. J. Wijers, and B. A. Zauderer. A New Population of Ultra-long Duration Gamma-Ray Bursts. *ApJ*, 781:13, January 2014.

[41] F. Walter, F. Bertoldi, C. Carilli, P. Cox, K. Y. Lo, R. Neri, X. Fan, A. Omont, M. A. Strauss, and K. M. Menten. Molecular gas in the host galaxy of a quasar at redshift z = 6.42. *Nature*, 424:406–408, July 2003.

[42] F. Walter, C. Carilli, F. Bertoldi, K. Menten, P. Cox, K. Y. Lo, X. Fan, and M. A. Strauss. Resolved Molecular Gas in a Quasar Host Galaxy at Redshift z=6.42. *ApJ*, 615:L17–L20, November 2004.

[43] Ruben Salvaterra, M Della Valle, S Campana, G Chincarini, S Covino, P D ' Avanzo, A Fernández-Soto, C Guidorzi, F Mannucci, R Margutti, et al. Grb 090423 at a redshift of z ≈ 8.1. *Nature*, 461(7268):1258–1260, 2009.

[44] G Ghirlanda, R Salvaterra, G Ghisellini, S Mereghetti, G Tagliaferri, S Campana, JP Osborne, P O'Brien, N Tanvir, D Willingale, et al. Accessing the population of high-redshift gamma ray bursts. *Monthly Notices of the Royal Astronomical Society*, 448(3):2514–2524, 2015.

[45] P. Mészáros and M. J. Rees. Population III Gamma-ray Bursts. *ApJ*, 715:967–971, June 2010.

[46] K. Toma, T. Sakamoto, and P. Mészáros. Population III Gamma-ray Burst Afterglows: Constraints on Stellar Masses and External Medium Densities. *ApJ*, 731:127, April 2011.

[47] Y. Suwa and K. Ioka. Can Gamma-ray Burst Jets Break Out the First Stars? *ApJ*, 726:107, January 2011.

[48] D. Nakauchi, Y. Suwa, T. Sakamoto, K. Kashiyama, and T. Nakamura. Long-duration X-Ray Flash and X-Ray-rich Gamma-Ray Bursts from Low-mass Population III Stars. *ApJ*, 759:128, November 2012.

[49] Masaru Shibata and Keisuke Taniguchi. Merger of binary neutron stars to a black hole: Disk mass, short gamma-ray bursts, and quasinormal mode ringing. *Physical Review D*, 73(6):064027, 2006.

[50] Lara Nava, Giancarlo Ghirlanda, Gabriele Ghisellini, and Annalisa Celotti. Spectral properties of 438 grbs detected by fermi/gbm. *Astronomy & Astrophysics*, 530:A21, 2011.

[51] BP Abbott, R Abbott, TD Abbott, MR Abernathy, F Acernese, K Ackley, C Adams, T Adams, P Addesso, RX Adhikari, et al. Astrophysical implications of the binary black hole merger gw150914. *The Astrophysical Journal Letters*, 818(2):L22, 2016.

[52] V Connaughton, E Burns, A Goldstein, MS Briggs, B-B Zhang, CM Hui, P Jenke, J Racusin, CA Wilson-Hodge, PN Bhat, et al. Fermi gbm observations of ligo gravitational wave event gw150914. *arXiv preprint arXiv:1602.03920*, 2016.

[53] Volodymyr Savchenko, Carlo Ferrigno, Sandro Mereghetti, Lorenzo Natalucci, Angela Bazzano, Enrico Bozzo, Søren Brandt, TJ-L Courvoisier, R Diehl, L Hanlon, et al. Integral upper limits on gamma-ray emission associated with the gravitational wave event gw150914. *The Astrophysical Journal Letters*, 820(2):L36, 2016.

[54] Ryo Tsutsui, Daisuke Yonetoku, Takashi Nakamura, Keitaro Takahashi, and Yoshiyuki Morihara. Possible existence of the ep-lp and ep-eiso correlations for short gamma-ray bursts with a factor 5–100 dimmer than those for long gamma-ray bursts. *Monthly Notices of the Royal Astronomical Society*, page stt262, 2013.

[55] Daisuke Yonetoku, Takashi Nakamura, Tatsuya Sawano, Keitaro Takahashi, and Asuka Toyanago. Short gamma-ray burst formation rate from batse data using ep-lp correlation and the minimum gravitational-wave event rate of a coalescing compact binary. *The Astrophysical Journal*, 789(1):65, 2014.

[56] Riccardo Giacconi, Herbert Gursky, Frank R Paolini, and Bruno B Rossi. Evidence for x rays from sources outside the solar system. *Physical Review Letters*, 9(11):439, 1962.

[57] P Padovani, G Ghisellini, AC Fabian, and A Celotti. Radio-loud agn and the extragalactic gamma-ray background. *Monthly Notices of the Royal Astronomical Society*, 260(1):L21–L24, 1993.

[58] Yoshiyuki Inoue and Tomonori Totani. The blazar sequence and the cosmic gamma-ray background radiation in the fermi era. *The Astrophysical Journal*, 702(1):523, 2009.

[59] Yoshiyuki Inoue, Kohta Murase, Grzegorz M Madejski, and Yasunobu Uchiyama. Probing the cosmic x-ray and mev gamma-ray background radiation through the anisotropy. *The Astrophysical Journal*, 776(1):33, 2013.

[60] P Sreekumar, FW Stecker, and SC Kappadath. The extragalactic diffuse gamma-ray emission. *arXiv preprint astro-ph/9709258*, 1997.

[61] Ka Lok Cheng and Gustavo E Romero. *Cosmic gamma-ray sources*, volume 304. Springer Science & Business Media, 2004.

[62] P. von Ballmoos. Future goals for γ-ray spectroscopy. *Experimental Astronomy*, 6:85–96, December 1995.

[63] Martin J Berger, JH Hubbell, SM Seltzer, J Chang, JS Coursey, R Sukumar, DS Zucker, and K Olsen. Xcom: photon cross sections database. *NIST Standard reference database*, 8:87–3597, 1998.

[64] Glenn F Knoll. *Radiation detection and measurement*. John Wiley & Sons, 2010.

[65] V Schönfelder, H Aarts, K Bennett, H De Boer, J Clear, W Collmar, A Connors, A Deerenberg, R Diehl, A Von Dordrecht, et al. Instrument description and performance of the imaging gamma-ray telescope comptel aboard the compton gamma-ray observatory. *The Astrophysical Journal Supplement Series*, 86:657–692, 1993.

[66] R. A. Cameron, J. D. Kurfess, W. N. Johnson, R. L. Kinzer, R. A. Kroeger, M. D. Leising, R. J. Murphy, G. H. Share, M. S. Strickman, and J. E. Grove. Operation and performance of the OSSE instrument. In C. R. Shrader, N. Gehrels, and B. Dennis, editors, *NASA Conference Publication*, volume 3137 of *NASA Conference Publication*, pages 3–14, February 1992.

[67] RA Cameron, JD Kurfess, WN Johnson, RL Kinzer, RA Kroeger, MD Leising, RJ Murphy, GH Share, MS Strickman, and JE Grove. Operation and performance of the osse instrument. In *NASA Conference Publication*, volume 3137, 1992.

[68] G. J. Fishman, C. A. Meegan, T. A. Parnell, R. B. Wilson, W. Paciesas, J. L. Mateson, T. L. Cline, and B. J. Teegarden. Burst and Transient Source Experiment (BATSE) for the Gamma Ray Observatory (GRO). *International Cosmic Ray Conference*, 3, August 1985.

[69] The batse instrument. `https://heasarc.gsfc.nasa.gov/docs/cgro/batse/BATSE-desc.html`.

[70] G Weidenspointner, M Varendorff, U Oberlack, D Morris, S Plüschke, R Diehl, SC Kappadath, M McConnell, J Ryan, V Schönfelder, et al. The comptel instrumental line background. *arXiv preprint astro-ph/0012332*, 2000.

[71] J. M. Ryan. Astrophysics challenges of MeV-astronomy instrumentation. *New Astronomy Reviews*, 48:199–204, February 2004.

[72] E. Aprile, A. Curioni, K.-L. Giboni, M. Kobayashi, U. G. Oberlack, E. L. Chupp, P. P. Dunphy, T. Doke, J. Kikuchi, and S. Ventura. LXeGRIT Compton telescope prototype: current status and future prospects. In J. E. Truemper and H. D. Tananbaum, editors, *X-Ray and Gamma-Ray Telescopes and Instruments for Astronomy.*, volume 4851 of *Society of Photo-Optical Instrumentation Engineers (SPIE) Conference Series*, pages 1196–1208, March 2003.

[73] A. Curioni, E. Aprile, T. Doke, K. L. Giboni, M. Kobayashi, and U. G. Oberlack. A study of the LXeGRIT detection efficiency for MeV gamma-rays during the 2000 balloon flight campaign. *Nuclear Instruments and Methods in Physics Research A*, 576:350–361, June 2007.

[74] E. Aprile, A. Curioni, K. L. Giboni, M. Kobayashi, U. G. Oberlack, and S. Zhang. Compton imaging of MeV gamma-rays with the Liquid Xenon Gamma-Ray Imaging Telescope (LXeGRIT). *Nuclear Instruments and Methods in Physics Research A*, 593:414–425, August 2008.

[75] E. Aprile, U. G. Oberlack, A. Curioni, V. Egorov, K.-L. Giboni, S. Ventura, T. Doke, J. Kikuchi, K. Takizawa, E. L. Chupp, and P. P. Dunphy. Preliminary results from the 1999 balloon flight of the Liquid Xenon Gamma-Ray Imaging Telescope (LXeGRIT). In K. A. Flanagan and O. H. Siegmund, editors, *X-Ray and Gamma-Ray Instrumentation for Astronomy XI*, volume 4140 of *Society of Photo-Optical Instrumentation Engineers (SPIE) Conference Series*, pages 344–359, December 2000.

[76] A. Curioni, E. Aprile, K.-L. Giboni, M. Kobayashi, U. G. Oberlack, E. L. Chupp, P. P. Dunphy, T. Doke, J. Kikuchi, and S. Ventura. On the background rate in the LXeGRIT Instrument during the 2000 Balloon Flight. In J. E. Truemper and H. D. Tananbaum, editors, *X-Ray and Gamma-Ray Telescopes and Instruments for Astronomy.*, volume 4851 of *Society of Photo-Optical Instrumentation Engineers (SPIE) Conference Series*, pages 1281–1293, March 2003.

[77] E. Aprile, A. Curioni, V. Egorov, K.-L. Giboni, U. G. Oberlack, S. Ventura, T. Doke, J. Kikuchi, K. Takizawa, E. L. Chupp, and P. P. Dunphy. Spectroscopy and imaging performance of the Liquid Xenon Gamma-Ray Imaging Telescope (LXeGRIT). In K. A. Flanagan and O. H. Siegmund, editors, *X-Ray and Gamma-Ray Instrumentation for Astronomy XI*, volume 4140 of *Society of Photo-Optical Instrumentation Engineers (SPIE) Conference Series*, pages 333–343, December 2000.

[78] S. E. Boggs, P. Jean, R. P. Lin, D. M. Smith, P. von Ballmoos, N. W. Madden, P. N. Luke, M. Amman, M. T. Burks, E. L. Hull, W. Craig, and K. Ziock. The nuclear compton telescope: A balloon-borne soft γ-ray spectrometer, polarimeter, and imager. In S. Ritz, N. Gehrels, and C. R. Shrader, editors, *Gamma 2001: Gamma-Ray*

Astrophysics, volume 587 of *American Institute of Physics Conference Series*, pages 877–881, October 2001.

[79] M. S. Bandstra, E. C. Bellm, S. E. Boggs, D. Perez-Becker, A. Zoglauer, H.-K. Chang, J.-L. Chiu, J.-S. Liang, Y.-H. Chang, Z.-K. Liu, W.-C. Hung, M.-H. A. Huang, S. J. Chiang, R.-S. Run, C.-H. Lin, M. Amman, P. N. Luke, P. Jean, P. von Ballmoos, and C. B. Wunderer. Detection and Imaging of the Crab Nebula with the Nuclear Compton Telescope. *ApJ*, 738:8, September 2011.

[80] D. Perez-Becker, C. Wunderer, S. E. Boggs, and Nct Collaboration. Overview of the Nuclear Compton Telescope. In *Proceedings of the 7th INTEGRAL Workshop*, page 152, 2008.

[81] Hiroyasu Tajima, Roger Blandford, Teruaki Enoto, Yasushi Fukazawa, Kirk Gilmore, Tuneyoshi Kamae, Jun Kataoka, Madoka Kawaharada, Motohide Kokubun, Philippe Laurent, et al. Soft gamma-ray detector for the astro-h mission. In *SPIE Astronomical Telescopes+ Instrumentation*, pages 773216–773216. International Society for Optics and Photonics, 2010.

[82] Shin Watanabe, Hiroyasu Tajima, Yasushi Fukazawa, Roger Blandford, Teruaki Enoto, Andrea Goldwurm, Kouichi Hagino, Katsuhiro Hayashi, Yuto Ichinohe, Jun Kataoka, et al. The soft gamma-ray detector (sgd) onboard astro-h. In *SPIE Astronomical Telescopes+ Instrumentation*, pages 990513–990513. International Society for Optics and Photonics, 2016.

[83] Christoph Winkler. Integral-a status report. *arXiv preprint arXiv:0912.0077*, 2009.

[84] Scott D Barthelmy, Louis M Barbier, Jay R Cummings, Ed E Fenimore, Neil Gehrels, Derek Hullinger, Hans A Krimm, Craig B Markwardt, David M Palmer, Ann Parsons, et al. The burst alert telescope (bat) on the swift midex mission. *Space Science Reviews*, 120(3-4):143–164, 2005.

[85] Amy Lien, Takanori Sakamoto, Scott D Barthelmy, Wayne H Baumgartner, John K Cannizzo, Kevin Chen, Nicholas R Collins, Jay R Cummings, Neil Gehrels, Hans A Krimm, et al. The third swift burst alert telescope gamma-ray burst catalog. *arXiv preprint arXiv:1606.01956*, 2016.

[86] Swift grbs. `http://swift.gsfc.nasa.gov/archive/grb_table/`.

[87] Andreas Zoglauer and Gottfried Kanbach. Doppler broadening as a lower limit to the angular resolution of next-generation compton telescopes. In *Astronomical Telescopes and Instrumentation*, pages 1302–1309. International Society for Optics and Photonics, 2003.

[88] Gerald R Lynch and Orin I Dahl. Approximations to multiple coulomb scattering. *Nuclear Instruments and Methods in Physics Research Section B: Beam Interactions with Materials and Atoms*, 58(1):6–10, 1991.

[89] Atsushi Takada. Development of advanced compton imaging camera with gaseous electron tracker and first flight of sub-mev gamma-ray imaging loaded-on-balloon experiment. *PhD Thesis*, 2007.

[90] T Tanimori, H Kubo, A Takada, S Iwaki, S Komura, S Kurosawa, Y Matsuoka, K Miuchi, S Miyamoto, T Mizumoto, et al. An electron-tracking compton telescope for a survey of the deep universe by mev gamma-rays. *The Astrophysical Journal*, 810(1):28, 2015.

[91] Atsushi Takada, Hidetoshi Kubo, Hironobu Nishimura, Kazuki Ueno, Kaori Hattori, Shigeto Kabuki, Shunsuke Kurosawa, Kentaro Miuchi, Eiichi Mizuta, Tsutomu Nagayoshi, et al. Observation of diffuse cosmic and atmospheric gamma rays at balloon altitudes with an electron-tracking compton camera. *The Astrophysical Journal*, 733(1):13, 2011.

[92] James C Ling. A semiempirical model for atmospheric γ rays from 0.3 to 10 mev at λ= 40. *Journal of Geophysical Research*, 80(22):3241–3252, 1975.

[93] RL Kinzer, GV Jung, DE Gruber, JL Matteson, Peterson, and LE. Diffuse cosmic gamma radiation measured by heao 1. *The Astrophysical Journal*, 475(1):361, 1997.

[94] E Jourdain and JP Roques. The high-energy emission of the crab nebula from 20 kev to 6 mev with integral spibased on observations with integral, an esa project with instruments and science data center funded by esa member states (especially the pi countries: Denmark, france, germany, italy, spain, and switzerland), czech republic and poland with participation of russia and usa. *The Astrophysical Journal*, 704(1):17, 2009.

[95] Atsuhiko Ochi, Tsutomu Nagayoshi, Satoshi Koishi, Toru Tanimori, Tomofumi Nagae, and Mirei Nakamura. Development of micro pixel chamber. *Nuclear Instruments and Methods in Physics Research Section A: Accelerators, Spectrometers, Detectors and Associated Equipment*, 478(1):196–199, 2002.

[96] Fabio Sauli. Gem: A new concept for electron amplification in gas detectors. *Nuclear Instruments and Methods in Physics Research Section A: Accelerators, Spectrometers, Detectors and Associated Equipment*, 386(2):531–534, 1997.

[97] T Tamagawa, N Tsunoda, A Hayato, H Hamagaki, M Inuzuka, H Miyasaka, I Sakurai, F Tokanai, and K Makishima. Development of gas electron multiplier foils with a

laser etching technique. *Nuclear Instruments and Methods in Physics Research Section A: Accelerators, Spectrometers, Detectors and Associated Equipment*, 560(2):418–424, 2006.

[98] Fabio Sauli. The gas electron multiplier (gem): Operating principles and applications. *Nuclear Instruments and Methods in Physics Research Section A: Accelerators, Spectrometers, Detectors and Associated Equipment*, 805:2–24, 2016.

[99] Osamu Sasaki and Mitsuhiro Yoshida. Asd ic for the thin gap chambers in the lhc atlas experiment. In *Nuclear Science Symposium, 1998. Conference Record. 1998 IEEE*, volume 1, pages 440–444. IEEE, 1998.

[100] Tetsuya Mizumoto, Yoshihiro Matsuoka, Yoshitaka Mizumura, Toru Tanimori, Hidetoshi Kubo, Atsushi Takada, Satoru Iwaki, Tatsuya Sawano, Kiseki Nakamura, Shotaro Komura, et al. New readout and data-acquisition system in an electron-tracking compton camera for mev gamma-ray astronomy (smile-ii). *Nuclear Instruments and Methods in Physics Research Section A: Accelerators, Spectrometers, Detectors and Associated Equipment*, 800:40–50, 2015.

[101] Yoshihiro Matsuoka, T Tanimori, H Kubo, A Takada, JD Parker, T Mizumoto, Y Mizumura, S Iwaki, T Sawano, S Komura, et al. Performance of a new electron-tracking compton camera under intense radiations from a water target irradiated with a proton beam. *Journal of Instrumentation*, 10(01):C01053, 2015.

[102] Tomohisa Uchida. Hardware-based tcp processor for gigabit ethernet. *IEEE Transactions on Nuclear Science*, 55(3):1631–1637, 2008.

[103] S Komura, T Tanimori, H Kubo, A Takada, JD Parker, T Mizumoto, Y Mizumura, S Sonoda, D Tomono, T Sawano, et al. Performance improvement of an electron-tracking compton camera by a new track reconstruction method. In *2013 IEEE Nuclear Science Symposium and Medical Imaging Conference (2013 NSS/MIC)*, pages 1–5. IEEE, 2013.

[104] S. Biagi. Magboltz: Transport of electrons in gas mixtures. `http://consult.cern.ch/writeup/magboltz/`.

[105] H Nishimura, K Hattori, S Kabuki, H Kubo, K Miuchi, T Nagayoshi, Y Okada, R Orito, H Sekiya, A Takada, et al. Development of large area gamma-ray camera with gso (ce) scintillator arrays and pspmts. *Nuclear Instruments and Methods in Physics Research Section A: Accelerators, Spectrometers, Detectors and Associated Equipment*, 573(1):115–118, 2007.

[106] Stefan Siegel, Robert W Silverman, Yiping Shao, and Simon R Cherry. Simple charge division readouts for imaging scintillator arrays using a multi-channel pmt. *Nuclear Science, IEEE Transactions on*, 43(3):1634–1641, 1996.

[107] Rene Brun and Fons Rademakers. Root—an object oriented data analysis framework. *Nuclear Instruments and Methods in Physics Research Section A: Accelerators, Spectrometers, Detectors and Associated Equipment*, 389(1):81–86, 1997.

[108] Fabio Sauli. Principles of operation of multiwire proportional and drift chambers. Technical report, European Organization for Nuclear Research, 1977.

[109] Sea Agostinelli, John Allison, K al Amako, J Apostolakis, H Araujo, P Arce, M Asai, D Axen, S Banerjee, G Barrand, et al. Geant4—a simulation toolkit. *Nuclear instruments and methods in physics research section A: Accelerators, Spectrometers, Detectors and Associated Equipment*, 506(3):250–303, 2003.

[110] Y Mizumura, T Tanimori, H Kubo, A Takada, JD Parker, T Mizumoto, S Sonoda, D Tomono, T Sawano, K Nakamura, et al. Development of a 30 cm-cube electron-tracking compton camera for the smile-ii experiment. *Journal of Instrumentation*, 9(05):C05045, 2014.

[111] A Takada, T Tanimori, H Kubo, JD Parker, T Mizumoto, Y Mizumura, S Iwaki, T Sawano, K Nakamura, K Taniue, et al. Simulation of gas avalanche in a micro pixel chamber using garfield++. *Journal of Instrumentation*, 8(10):C10023, 2013.

[112] Christophe Geuzaine and Jean-François Remacle. Gmsh: A 3-d finite element mesh generator with built-in pre-and post-processing facilities. *International Journal for Numerical Methods in Engineering*, 79(11):1309–1331, 2009.

[113] Mikko Lyly, Juha Ruokolainen, and Esko Järvinen. Elmer–a finite element solver for multiphysics. *CSC-report on scientific computing*, 2000:156–159, 1999.

[114] Garfield++. `http://garfieldpp.web.cern.ch/garfieldpp/`.

[115] Ö Şahin, I Tapan, EN Özmutlu, and R Veenhof. Penning transfer in argon-based gas mixtures. *Journal of Instrumentation*, 5(05):P05002, 2010.

[116] J Byrne. Iii. - statistics of the electron-multiplication process in proportional counters. *Proceedings of the Royal Society of Edinburgh. Section A. Mathematical and Physical Sciences*, 66(01):33–41, 1962.

[117] A Takada, T Tanimori, H Kubo, K Miuchi, S Kabuki, JD Parker, Y Kishimoto, T Mizumoto, K Ueno, S Kurosawa, et al. Simulation study for the higher sensitivity

of an electron-tracking compton camera at over 1 mev. In *Nuclear Science Symposium and Medical Imaging Conference (NSS/MIC), 2011 IEEE*, pages 1215–1221. IEEE, 2011.

[118] BF Phlips, GV Jung, Mark D Leising, JE Grove, WN Johnson, RL Kinzer, RA Kroeger, JD Kurfess, MS Strickman, DA Grabelsky, et al. Gamma-ray observations of cygnus x-1 with the oriented scintillation spectrometer experiment. *The Astrophysical Journal*, 465:907, 1996.

[119] FL Vieyro, Y Sestayo, GE Romero, and JM Paredes. Nonthermal processes and neutrino emission from the black hole gro j0422+ 32 in a bursting state. *Astronomy & Astrophysics*, 546:A46, 2012.

[120] RL Kinzer, WR Purcell, and JD Kurfess. Gamma-ray emission from the inner galactic ridge. *The Astrophysical Journal*, 515(1):215, 1999.

[121] Andrew W Strong, Igor V Moskalenko, and Olaf Reimer. Diffuse continuum gamma rays from the galaxy. *The Astrophysical Journal*, 537(2):763, 2000.

[122] PMW Kalberla, WB Burton, Dap Hartmann, EM Arnal, E Bajaja, R Morras, and WGL Pöppel. The leiden/argentine/bonn (lab) survey of galactic hi-final data release of the combined lds and iar surveys with improved stray-radiation corrections. *Astronomy & Astrophysics*, 440(2):775–782, 2005.

[123] David J Schlegel, Douglas P Finkbeiner, and Marc Davis. Maps of dust infrared emission for use in estimation of reddening and cosmic microwave background radiation foregrounds. *The Astrophysical Journal*, 500(2):525, 1998.

[124] Richard Willingale, RLC Starling, Andrew P Beardmore, Nial R Tanvir, and Paul T O'Brien. Calibration of x-ray absorption in our galaxy. *Monthly Notices of the Royal Astronomical Society*, 431(1):394–404, 2013.

[125] Fan Lei, Alex Hands, Simon Clucas, Clive Dyer, and Pete Truscott. Improvements to and validations of the qinetiq atmospheric radiation model (qarm). In *Radiation and Its Effects on Components and Systems, 2005. RADECS 2005. 8th European Conference on*, pages D3–1. IEEE, 2005.

[126] S. V. Koldashov, V. V. Mikhailov, and S. A. Voronov. Electron and Positron Albedo Spectra with Energy more than 20 MeV. *International Cosmic Ray Conference*, 4:993, 1995.

[127] A Takada, T Tanimori, H Kubo, T Mizumoto, Y Mizumura, S Komura, T Kishimoto, T Takemura, K Yoshikawa, Y Nakamasu, et al. Mev gamma-ray observation with a

well-defined point spread function based on electron tracking. In *SPIE Astronomical Telescopes+ Instrumentation*, pages 99052O–99052O. International Society for Optics and Photonics, 2016.

[128] David L Band. Comparison of the gamma-ray burst sensitivity of different detectors. *The Astrophysical Journal*, 588(2):945, 2003.

[129] Marco Ajello, J Greiner, G Sato, DR Willis, G Kanbach, AW Strong, R Diehl, G Hasinger, N Gehrels, CB Markwardt, et al. Cosmic x-ray background and earth albedo spectra with swift bat. *The Astrophysical Journal*, 689(2):666, 2008.

[130] Jea Abadie, BP Abbott, Richard Abbott, Matthew Abernathy, Timothee Accadia, Fausto Acernese, Carl Adams, Rana Adhikari, Parameswaran Ajith, Bruce Allen, et al. Predictions for the rates of compact binary coalescences observable by ground-based gravitational-wave detectors. *Classical and Quantum Gravity*, 27(17):173001, 2010.